Title

THE DEVELOPMENT OP A MULTIWIRE PROPORTIONAL CHAMBER IMAGING SYSTEM FOR NEUTRON RADIOGRAPHY

Author

Valentine, Kenneth Howard.

Publication Date

1974-05-01

THE DEVELOPMENT OF A MULTIWIRE PROPORTIONAL CHAMBER IMAGING SYSTEM FOR NEUTRON RADIOGRAPHY

Kenneth Howard Valentine
(Ph. D. Thesis)

May 1974

Prepared for the U. S. Atomic Energy Commission
under Contract W-7405-ENG-48

DISCLAIMER

THE DEVELOPMENT OF A MULTIWIRE PROPORTIONAL CHAMBER IMAGING SYSTEM FOR NEUTRON RADIOGRAPHY

Contents

Abstract. vii

I. Review of Neutron Radiographic Techniques 1

A. History of Neutron Radiography. 1

B. Interactions of Neutrons with Matter. 4

C. Radiographic Neutron Sources and Beams. 10

D. Neutron Radiographic Image Detectors. 15

E. Purpose of Present Research 22

II. Description of Exposure Facility. 24

A. Triga Mark III Reactor. 24

B. Beam Collimation. 24

C. Shutter 27

D. Experiment Holder and Shielding 29

E. Commercial Image Detector 31

III. Description of MWPC Imaging System. 34

A. Multiwire Proportional Chamber. 34

1. Electron Drift and Multiplication 34

2. Formation of Induced Pulses 45

B. Detection and Amplification of MWPC Output Pulses 48

C. Coordinate Readout Methods. 54

D. Electronic Signal Processing. 58

E. Neutron Sensitization of MWPC 64

1. Boron Layer for Thermal and Epithermal Energies 64

2. Polyethylene Layer for Fast Neutrons. 69

IV. Hardware and Construction. 72

A. Prototype Chamber Design 72

B. 10 × 10 Inch Chamber Design. 74

C. Neutron Converters 78

D. Description of Electronic Equipment. 79

1. Delay Lines. 79

2. Amplifiers 86

3. Timing SCA 86

4. Pileup Rejector and Area Selector. 87

5. TAC's. 88

6. Performance Characteristics. 88

V. Experimental Measurements. 91

A. Discussion of Measurements 91

B. Prototype Chamber Measurements (Efficiency and Resolution) . . 95

C. 10 × 10 Inch Chamber Measurements. 98

1. Boron Coating Areal Density Measurement. 98

2. Neutron Detection Efficiency 100

3. Resolution 112

4. Lucite Attenuation Measurements. 123

D. Performance Analysis Methods for Resolution and Comparison with Experimental Results. 127

VI. Imaging with Neutron Sensitive MWPC. 137

A. Direct CRT Imaging 137

B. Image Storage in 4096 Channel Analyzer 139

1. On-Line Readout. 139

2. Off-Line (7600) Image Processing 142

VII. Conclusions 151

Appendix A. Induced Cathode Pulses and Delay Line Interpolation 155

Appendix B. Schematic Diagrams of Fiducial Mark Generator and Digital Photographic Display Unit 159

Appendix C. Details of MTF Calculations 162

Acknowledgments 169

References 170

THE DEVELOPMENT OF A MULTIWIRE PROPORTIONAL CHAMBER IMAGING SYSTEM FOR NEUTRON RADIOGRAPHY

Kenneth Howard Valentine

Department of Physics
Lawrence Berkeley Laboratory and
Department of Nuclear Engineering
University of California
Berkeley, California 94720

April 1974

ABSTRACT

A multiwire proportional chamber was developed for thermal, epithermal, and fast neutron radiographic imaging. It employs electromagnetic delay lines for coordinate readout and solid layer neutron-to-charged particle converters. Thermal neutron detection efficiencies of nearly 4% and spatial resolutions of 2 mm were achieved. Model calculations were in good agreement with experiment and indicate that substantial improvements in both the efficiency and resolution are possible.

The value of the neutron sensitive multiwire proportional chamber (MWPC) as a radiographic image detector lies in its ability to image single interactions and to supply coordinate information in a form that is easily digitized for computer storage and processing. Sample radiographs are presented which demonstrate the MWPC's capability for low dose imaging and several examples of computer processed radiographs are shown.

Initial work was done with a small (4 × 4.5 cm active area) x-ray chamber which was sensitized to neutrons by the addition of a 3-μm-thick layer of natural boron. The (n,α) reaction on ^{10}B supplied the charged particles necessary for neutron detection. This prototype chamber

performed approximately as expected so a larger chamber (25 × 25 cm active area) was designed and built. Enriched ^{10}B converting surfaces were fabricated for thermal and epithermal imaging, and fast neutron imaging was accomplished with a hydrogenous (polyethylene) recoil proton converter.

The system's spatial resolving power was determined by Fourier transformation of experimentally measured line spread functions which results in the modulation transfer function. Resolution measurements were made using low energy x-rays (5.9 keV) as well as neutrons. Comparison of the results obtained for the two types of radiation indicates the extent to which the resolving power is limited by longer range charged particles.

I. REVIEW OF NEUTRON RADIOGRAPHIC TECHNIQUES

By virtue of its electrical neutrality, the neutron eluded discovery until 1932 when it was identified by Chadwick through the application of momentum and energy balances to the $Be(\alpha,n)C$ reaction.[1] This same property of neutrality, which had complicated the neutron's discovery, was also primarily responsible for the interest in its radiographic application. Being neutral, the neutron can interact with matter in completely different ways from those observed for charged particles and electromagnetic radiation. It can pass almost unimpeded through the atomic electron shells and approach the nucleus with no Coulombic repulsion. Interaction mechanisms of radiographic interest between neutrons and matter are therefore nuclear in nature whereas those for charged particles and electromagnetic radiation are basically atomic phenomena.

A. History of Neutron Radiography

The first documented investigation specifically aimed at evaluating the use of neutrons as a radiographic probe dates back almost as far as the neutron's discovery. It was initiated in Germany in 1935 by Kallmann and Kuhn. Although their work was hindered by an extremely low intensity neutron source (a small discharge tube ion accelerator yielding about 4×10^7 neutrons/sec), they were able to collect a great deal of information about neutron source characteristics and image detection methods. As a result of this investigation, one publication appeared in 1948 which described some basic detection techniques that are still in use today.[2]

Concurrent with the later stages of Kallmann's work was another investigation of neutron radiography also conducted in Germany by Peter in 1946.[3] Due to a much higher neutron source strength (about 2×10^{11} neutrons/sec from a discharge tube ion accelerator), he was able to reduce Kallmann's exposure time from four hours to about two minutes and the neutron radiographs which he published were of reasonable quality.

A period of about ten years lapsed after Peter's work during which time little more was done in the area of neutron radiography. It has been suggested by Berger[4] that this dwell time was primarily due to the application of available sources to the more pressing needs of neutron physics experiments. This seems reasonable since the third major study of neutron radiography was done by Thewlis[5] and Thewlis and Derbyshire[6] in 1956, following the advent of the neutron chain reactor. They extracted their neutron beam from the BEPO reactor at Harwell, England and produced the best neutron radiographs available at that time. Their work illustrated some possible uses for neutron radiography in biological studies, inspection of heavy metals, and in radiographic contrasting problems that could not be easily solved by other means. One product of their investigation was a radiograph of a waxed string taken through two inches of lead which has become the classic example of the complementary contrast capability of neutron radiography.

Despite the impetus from the positive results obtained by Thewlis and Derbyshire, no more notable research was done for another four years--suitable reactors and neutron detection materials were still not abundant. In the period 1960-61, several independent studies were begun at Armour Research Foundation,[7] Argonne National Laboratory,[8] Naval Ordnance

Laboratory,[9] and Watertown Arsenal.[10] The emphasis of the work was directed toward the development and evaluation of improved sources, collimation systems, and imaging detectors. Also, work was done on delineating the limitations and areas of greatest applicability of neutron radiography.

The intense neutron beams provided by reactor neutron sources greatly aided in the optimization of neutron radiographic parameters so that by about 1968, the details of neutron beam collimation and detection were well understood. Expanding technology supplied a multitude of applications. From the aerospace industry came requirements for non-destructive-testing (NDT) of components such as nuclear rocket nozzle test sections, ordnance devices (explosive bolts), and jet engine turbine blades.[11] Neutron radiography was employed in the nuclear industry for NDT inspection of unirradiated and irradiated fuel elements, control rods, and in-core thermionic cells.[12] Also at this time, interest revived in portable non-reactor neutron sources which would broaden the application of neutron radiography and make it a more flexible NDT technique. It is interesting to note that as of 1972 there were approximately a hundred neutron radiographic facilities in operation around the world, compared to about fifty in 1968 and four in 1963.

The main elements of neutron radiography are neutron interactions in matter (both in the subject and the detector), neutron sources and beam collimation, and neutron image detectors. Each area will be considered in the remainder of this section.

B. Interactions of Neutrons with Matter

As mentioned previously, neutrons interact mainly with the nuclei of materials and there are several clearly distinguishable mechanisms by which the interaction can proceed. Among these mechanisms are compound nucleus formation, potential or shape scattering, and direct interaction.

Compound Nucleus Formation. This process involves the reaction $n + {}_{Z}M^{A} \rightarrow {}_{Z}M^{A+1}$. Since the compound nucleus, ${}_{Z}M^{A+1}$, must be at rest in the center of mass system of coordinates, the center of mass kinetic energies of both the incident neutron and the target nucleus must be transformed to internal energy of the compound nucleus. However, in most cases, this is only a small contribution to the total excitation energy. Assuming for the moment that the nucleus, ${}_{Z}M^{A+1}$, is stable against neutron emission, it follows that a positive amount of energy must be expended in order to remove one neutron. This energy is called the neutron binding energy, and when the reverse process of adding one neutron to the nucleus ${}_{Z}M^{A}$ occurs, it is available to the compound nucleus as excitation energy. The total excitation of the compound nucleus is the sum of the neutron binding energy and the center of mass kinetic energies. Since neutron binding energies tend to be in the MeV range, the kinetic energy of slow neutron reactions need not be considered in the total excitation.

The excited compound nucleus can decay to a ground state in a variety of ways. Since the excitation energy is as least as large as the neutron binding energy, the compound nucleus exists in an unbound state such that it is possible for a nucleon or a group of nucleons to be emitted. If a neutron is emitted with the total excitation energy, the process is called compound elastic scattering. If the neutron carries away only a

fraction of the excitation, the process is called compound inelastic scattering and the remainder of the excitation is then dissipated through either gamma emission or beta followed by gamma emission.

If a single neutron is not emitted, the process is called neutron absorption. One possibility in this case is emission of more than one neutron, a proton or some other group of nucleons such as an alpha particle followed by gamma or beta plus gamma decay as before. Another possibility is that the approach to a ground state will proceed directly by beta or gamma emission. Finally, neutron absorption in certain of the heavier nuclei can lead to fission. Once the compound nucleus has decayed to a bound state, nucleon emission and fission are no longer energetically possible.

Potential Scattering. In this process the neutron approaches the nucleus closely enough to be deflected by the short range nuclear forces. No compound nucleus is formed and no excitations occur.

Direct Interaction. This process occurs only with neutrons of relatively high energy. In a direct interaction, a nucleon is ejected from the nucleus as a result of direct collision with the incident neutron.

A particular nucleus can exhibit any or all of the three interaction mechanisms described above. The likelihood or probability of a particular interaction occurring is expressed as a cross section which is measured in units of 10^{-24} cm^2 called barns. The cross section for a neutron interaction can loosely be interpreted as the area which a neutron must strike in order to cause the interaction. This interpretation leads to the correct expression for neutron attenuation in extended

materials consisting of many layers of atoms. If a neutron beam of intensity I_o passes through a thickness x of material having an atomic density of N, where each atomic nucleus has a cross section of σ, then the emerging beam intensity I(x) satisfies

$$\frac{I(x)}{I_o} = e^{-N\sigma x} \rightarrow \sigma = \frac{\ln(I_o/I(x))}{Nx} \quad .$$

The second expression is indicative of the way in which experimental cross sections are actually obtained. The fact that some cross sections are many orders of magnitude larger than the physical size of the nucleus can only be explained through the application of quantum-mechanical considerations.

Neutron cross sections vary as the incident neutron energy varies and many nuclei exhibit spectacular increases at certain energies known as resonances. These resonances occur both in absorption cross sections and scattering cross sections. Therefore the total cross section, which is the sum of absorption plus scattering, also shows resonance behavior. While analytical models exist which describe much of the observed cross section behavior, they are extremely complex and sometimes impossible to apply. However, by dividing nuclei into three groups according to their atomic weight (light, $A < 25$; intermediate, $25 < A < 80$; heavy, $A > 80$), several generalizations can be made which apply in many cases.[13]

Light and Some Magic* Nuclei. At energies below about 1 eV, the total cross section, σ_t, often behaves as $\sigma_t = C_1 + \frac{C_2}{v}$ where C_1 and C_2

*Certain nuclei possess a "magic" number of protons and/or neutrons which leads to exceptionally stable configurations due to closure of nucleon shells.[14]

are constants and v is the velocity of the neutron. Here C_1 accounts for elastic scattering and C_2 for absorption. If C_1 is much greater than C_2, the total cross section will be fairly constant over this energy range whereas if C_2 is the larger, the material will be a socalled 1/v absorber and the cross section will decrease hyperbolically with increasing neutron energy. In the MeV region the total cross section is no longer constant or 1/v and several broad resonances can occur. Beyond 6 or 8 MeV the cross section becomes smooth and rolling.

Heavy Nuclei (not Magic). Below 1 eV the total cross section may be flat or 1/v. Between 1 eV and 100 eV a series of high narrow resonances occur. Beyond 100 eV the resonances lose amplitude and group closer together and past 5 keV the cross section is smooth.

Intermediate Nuclei. In this case the total cross section may or may not be 1/v below 1 eV. The resonance region lies between 100 eV and 100 keV and the character of the resonances is intermediate between that of light and heavy nuclei. Intermediate resonances are higher and narrower than for light nuclei but lower and broader than for heavy nuclei. Figure 1 shows the energy dependence of the cross section for a light and two heavy nuclides.

The spectrum of energies encountered in neutron physics has been divided into several convenient groups. Although the group limits are subject to a certain amount of variation in the literature, the values in Table I below are typical and will be used in this thesis.

Since a large fraction of neutron radiography is performed using thermal neutrons, the values of thermal neutron interaction cross sections are especially important. Figure 2 shows a plot of the mass

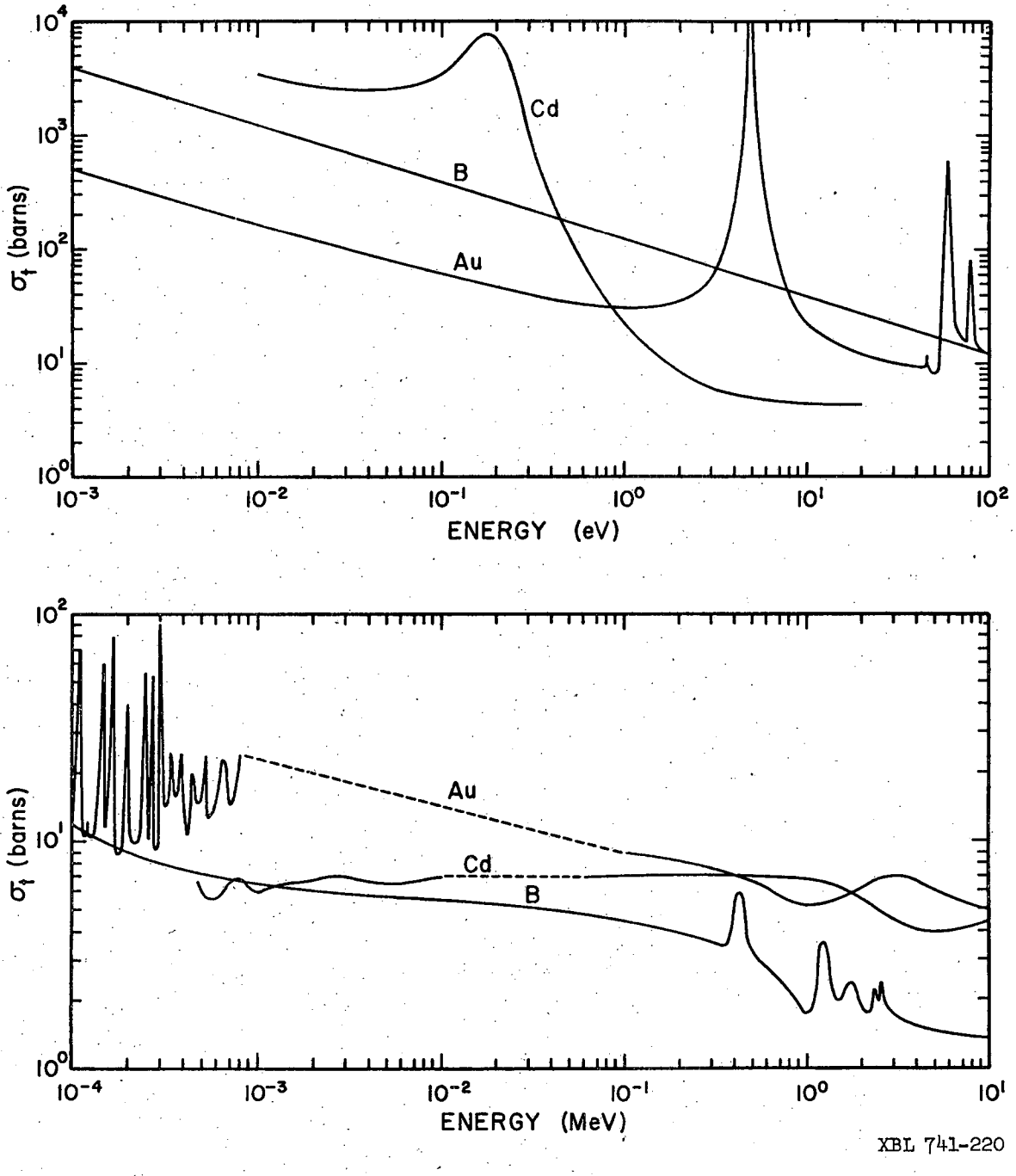

Fig. 1. Total interaction cross sections of boron, cadmium, and gold from 0.001 eV to 10 MeV. The omitted cadmium resonance region is similar in structure to the gold resonance region (data from Ref. 13).

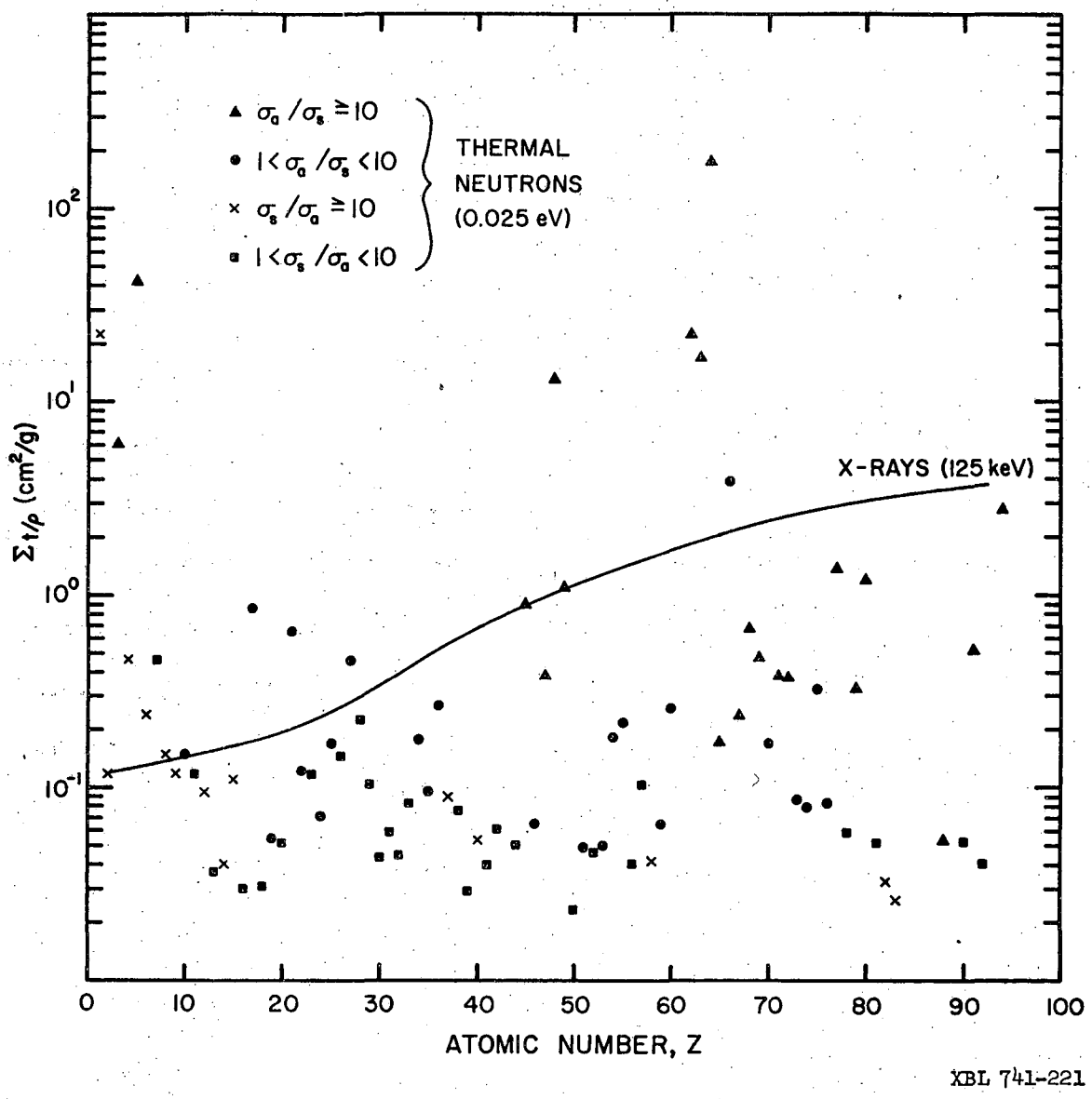

Fig. 2. Mass attenuation coefficients of the elements for 0.025 eV neutrons and 125 keV x-rays (neutron data from Ref. 13 and x-ray data from Ref. 15).

Table I. Neutron Energy Groups

cold	less than 0.01 eV
thermal	0.01 eV to 0.4 eV
epithermal or epicadmium	0.4 eV to 10 keV
slow	0 to 10 keV
fast	10 keV to 20 MeV
relativistic	greater than 20 MeV

attenuation coefficients of the elements for 0.025 eV neutrons and 125 keV x-rays as a function of the atomic number, Z. The mass attenuation coefficient can be directly related to the cross section through the expression $\sigma_t = \frac{\rho}{N} (\frac{\Sigma_t}{\rho})$. While the x-ray mass attenuation coefficient is a smoothly increasing function of atomic number, the neutron mass attenuation coefficient varies randomly. Under certain circumstances neutrons can solve radiographic imaging problems that would be impossible using x-rays. For instance, neutrons are especially well suited for imaging hydrogenous materials imbedded in low-Σ metals and for providing contrast between similar-Z materials like cadmium and indium or boron and beryllium.

C. Radiographic Neutron Sources and Beams

There are many known nuclear reactions which result in neutron emission but considerations such as yield, lifetime, non-neutron radiation levels, cost, and availability severely limit the number which can be practically applied. Application of the useable reactions results in three major neutron source categories, these being accelerator sources, isotopic sources, and reactor sources.

Accelerator sources are based on reactions such as $^{9}Be(d,n)^{10}B$, $t(d,n)^{4}He$, $d(d,n)^{3}He$, $^{7}Li(p,n)^{7}Be$, and $d(p,n)^{3}He$. A small linear accelerator is used to accelerate the projectile particle to a sufficiently high energy so the cross-section for the reaction involved is large enough to produce the desired yield. The $t(d,n)^{4}He$ reaction is widely used because acceleration voltages as low as 150 kilovolts can produce useable yields whereas acceleration voltages on the order of millions of volts are necessary to employ the other reactions. Practical accelerator sources of the d-t type can produce neutron yields in excess of 10^{11} neutrons/sec.[16]

Isotopic sources are similar to accelerator sources in that energetic radiation is used to induce neutron emission from a suitable target nucleus. The principal difference is that in an isotopic source the energetic radiation is derived from a radioactive isotope. The two principal reactions used in isotopic sources are (α,n) and (γ,n). Typical examples of the (α,n) variety are the Ra-Be source and the Pu-Be source. Since the yields from these sources are typically 10^{6} to 10^{7} neutrons/sec per curie of activity, kilocurie strength sources are necessary to match the output of the accelerator source. However, a ^{124}Sb-Be source of the (γ,n) variety is documented with a yield of 10^{10} neutrons/sec.[17] This source has the added advantage that due to the higher penetrating power of gamma rays, the antimony and beryllium need not be intimately mixed and the neutron output can be turned off simply by physically separating these two materials. The Sb activity decays with a half life of 60 days but can be replenished by neutron irradiation in a reactor. A notable exception to the foregoing is the ^{252}Cf spontaneous fission source. This material has a specific activity of about 3×10^{9} neutrons/sec-mg and a half-life of 2.2 years.[18]

Neutron chain reactors employing the neutron induced fission of such fissile materials as uranium, plutonium, or thorium are, and will probably continue to be, the most intense sources of neutrons. Their main disadvantage is immobility which requires that all work be performed at the reactor site.

The neutrons released in the nuclear reactions on which most neutron sources are based have energies typically in the hundred keV to MeV range. Although several investigations have been made using neutrons in this energy range,[19,20] the results were not as spectacular as those obtained with thermal neutrons. Many materials exhibit similar attenuation characteristics for high energy neutrons and the generally low interaction cross sections make detection difficult. Thus for most applications it is necessary to reduce their energy or moderate them. This moderation process is usually accomplished by surrounding the source with a layer of hydrogenous material. The initial source neutron energy is then lowered by successive elastic interactions with the hydrogen nuclei. Thermal reactors already have large amounts of moderating material incorporated in their design, so in this case, no further moderation is necessary.

Regardless of the type of neutron source used, by the time the neutrons are moderated to thermal energies their angular distribution is nearly isotropic. The extracted beam must therefore be passed through a collimator in order to limit the angular spread of neutrons in the beam. Magnetic or electrostatic focusing techniques are useless for this purpose due to the neutron's electrical neutrality, so collimation must be achieved by complete removal of the unwanted angular components. Tighter

beam collimation can be gained only at the expense of reduced beam intensity. Figure 3 shows the two most widely used collimator designs.

The multichannel collimator in many cases consists of a bundle of parallel stainless steel tubes which are sometimes coated with cadmium. Although this type of collimator was used almost exclusively in the early 1960's, the divergent collimator is perhaps the easier of the two to fabricate and is receiving more widespread attention today.

The two collimation systems are similar with respect to the degree of collimation, beam intensity, and field size. If the intensity and angular distribution of the neutron flux at the collimator entrance is the same for each type of collimator, then the beam intensity at the image plane will in each case be proportional to d^2/L^2 and the beam divergence as seen by a point in the image plane is in each case approximately equal to $\frac{d}{L}$ radians. In addition to these similarities, the divergent system offers several distinct advantages as pointed out by Barton in 1967.[21]

1. For similar source-modulator assemblies, the divergent collimator displaces less moderator material which could result in slightly higher beam intensities.
2. No collimator pattern is projected onto the image plane.
3. Field size can be increased simply by moving away from the collimator exit.
4. Geometric magnification can be achieved by separating the object and detector.

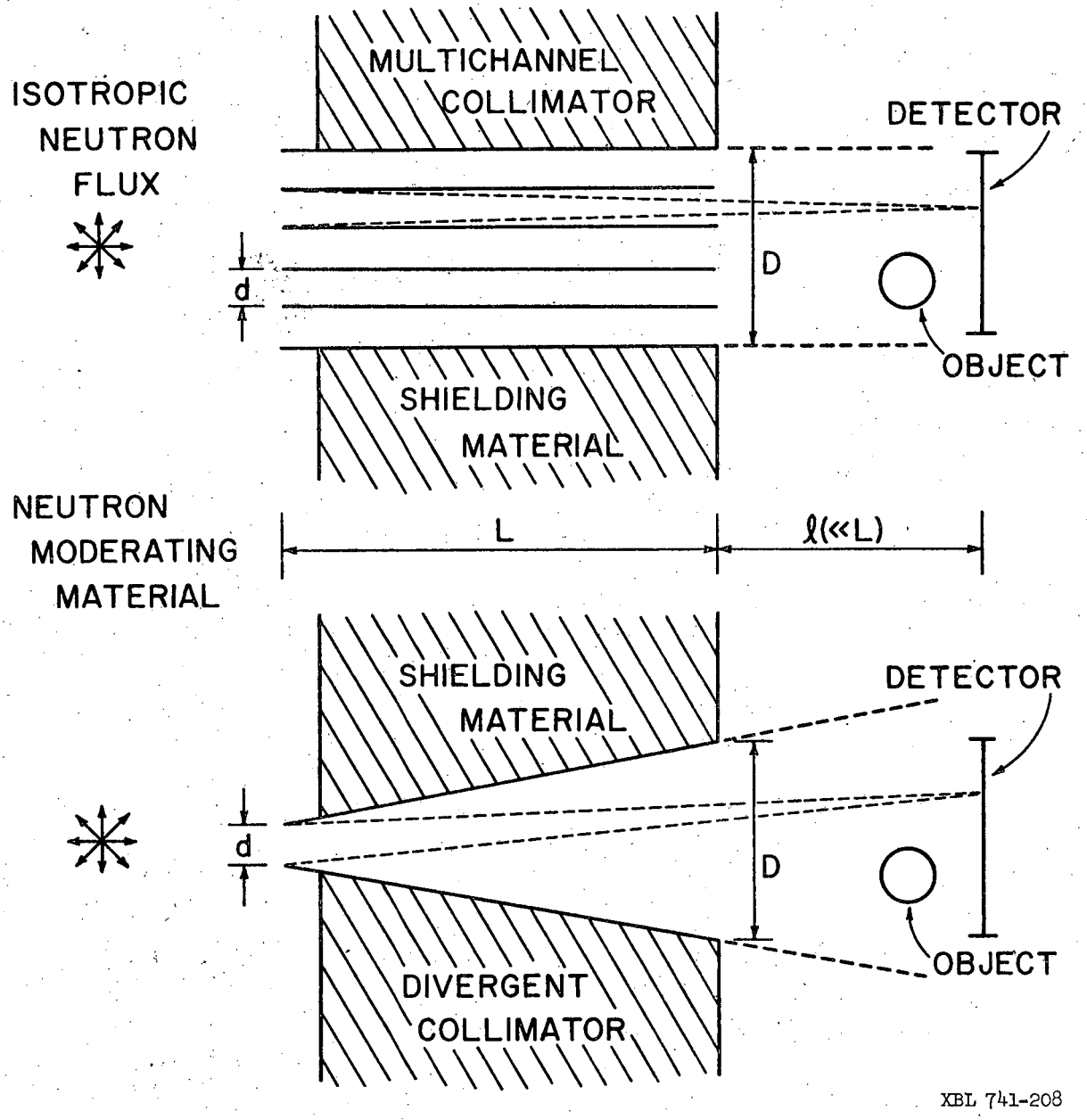

Fig. 3. Diagram of multichannel and divergent beam neutron collimators.

D. Neutron Radiographic Image Detectors

Techniques used to produce neutron radiographic images bear close resemblance to those used in x-radiography. The collimated beam of radiation is used to illuminate the radiographic object. The beam's intensity is then locally modulated as it passes through the object according to local interaction cross sections and areal density. A detector, placed behind the object so as to intercept the emergent beam, is used to obtain an image which reveals the internal structure of the object.

Although neutrons are capable of exposing photographic emulsions (by secondary radiation following neutron capture on one of the film constituents or by recoil protons ejected from the gelatin binder and plastic backing) the processes involved are not very efficient.[20] In order to reduce the neutron exposure required to produce a photographic image, converter screens are used which are made of materials having large cross sections for neutron interactions that result in the emission of more ionizing forms of radiation. Neutron converting screens are analogous to x-ray intensifying screens such as calcium tungstate which convert high energy x-ray photons to lower energy light photons.

Materials commonly used to make thermal neutron converter screens are gadolinium, dysprosium, indium, boron, and lithium. As can be seen from Fig. 2 each of these materials has a high thermal neutron absorption cross section. While all materials emit some form of prompt radiation immediately following neutron capture, some decay by emission to intermediate states with measurably long half lives. This process is called neutron activation and results in the formation of radioactive nuclei.

Figure 4 shows two variations of the photographic neutron image detection method. In the direct method the film is held in close contact with the converter during neutron exposure, and the film exposure is due to prompt radiation from the converter. For this method the converter screen can be made of any of the materials listed in Table II.

For the transfer method, only the converter screen is placed in the neutron beam and it must be made of one of the materials which undergoes neutron activation such as indium or dysprosium. During neutron exposure a radioactive image of the object is formed on the converter screen. After neutron exposure, the latent radioactive image on the converter is transformed to a latent photographic image on film by placing the converter and film in close contact and allowing the activity to decay for several half-lives. Since the activity of the converter is only a function of the neutron fluence (other activation cross-sections are relatively small), the transfer exposure is a powerful method for obtaining neutron radiographs of objects which are themselves radioactive, such as irradiated nuclear fuels. It also provides good immunity to non-neutron radiation components in the beam.

The ranges of the radiations emitted from the metallic converting materials typically lie between one and ten mils and this is the order of resolution obtainable from metallic and metallic oxide systems. In the case of cadmium the principal photographic effect is due to gamma rather than beta emission, and cadmium provides the poorest resolution of the metallic converters.[24]

Converting layers of boron or lithium fluoride (pure lithium is too reactive to form a stable converting layer) can, in principle, provide

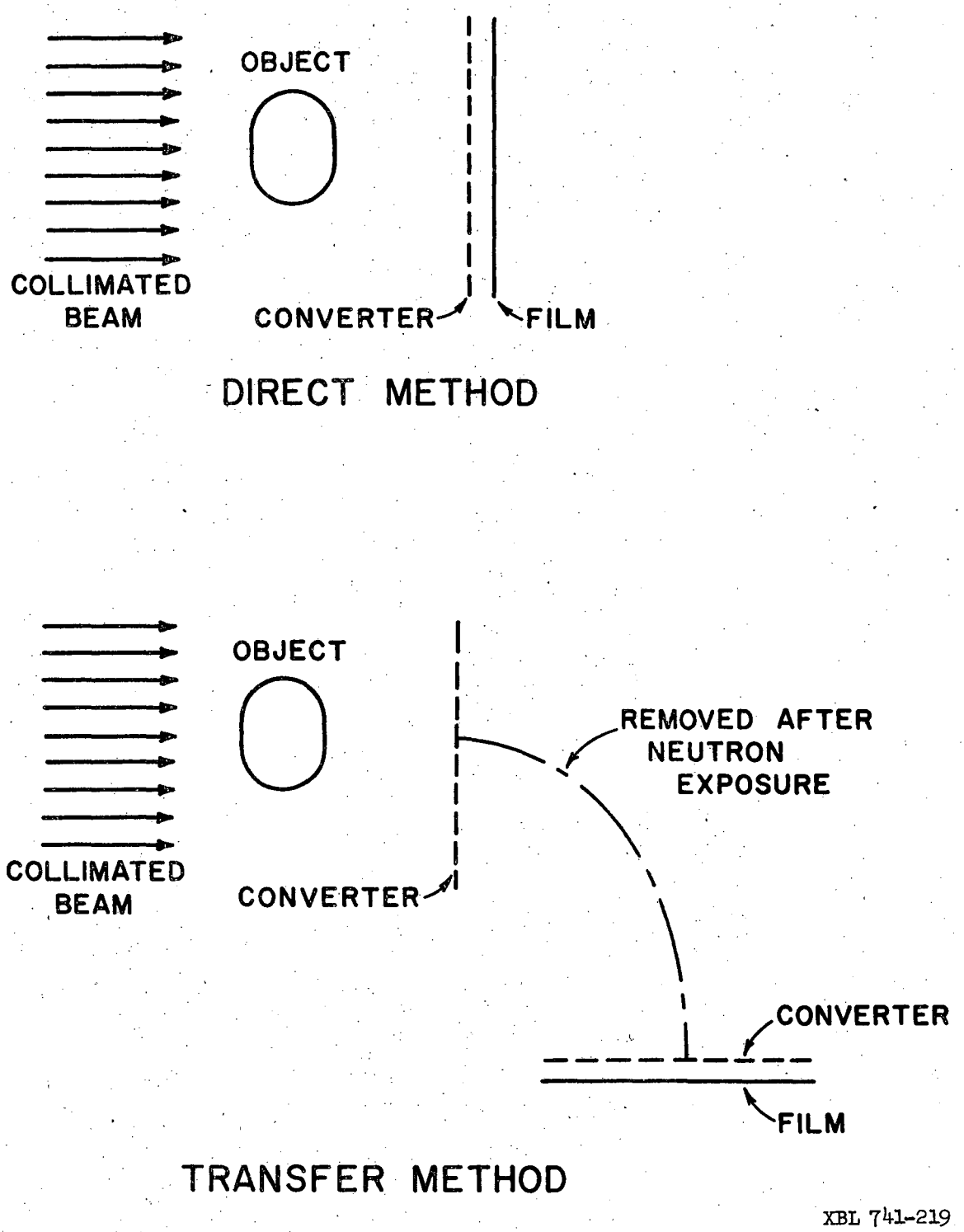

Fig. 4. Diagram of photographic neutron image detection methods, (a) direct method, (b) indirect or transfer method.

Table II. Characteristics of Various Neutron Converter Materials[a]

Isotope and Percent Abundance	Reaction	Reaction Cross Section for Thermal Neutrons (barns)	Half Life for Activation Products	Predominant Radiation and Particle Energy
$^{10}B(18.8)$	$^{10}B(n,\alpha)^{7}Li$	3,840	----	$\alpha + {}^{7}Li = 2.3$ MeV
$^{6}Li(7.5)$	$^{6}Li(n,\alpha)^{3}H$	945	----	$\alpha + {}^{3}H = 4.78$ MeV
$^{113}Cd(12.26)$	$^{113}Cd(n,\gamma)^{114}Cd$	20,000	----	gamma
$^{155}Gd(14.73)$	$^{155}Gd(n,\gamma)^{156}Gd$	56,000	----	gamma and beta[b]
$^{157}Gd(15.68)$	$^{157}Gd(n,\gamma)^{158}Gd$	242,000	----	
$^{115}In(96)$	$^{115}In(n)^{116}In$	52	13 sec	β(3.3 MeV)
	$^{115}In(n)^{116m}In$	155	54.2 min	β(0.90 MeV)
$^{197}Au(100)$	$^{197}Au(n)^{198}Au$	96	2.7 days	β(0.96 MeV)
$^{107}Ag(51)$	$^{107}Ag(n)^{108}Ag$	45	2.3 min	β(1.15 MeV)
	$^{109}Ag(n)^{110}Ag$	113	24.2 sec	β(2.2 MeV)
	$^{109}Ag(n)^{110m}Ag$	3.2	270 days	β(0.1 MeV)
$^{103}Rh(100)$	$^{103}Rh(n)^{104}Rh$	140	44 sec	(2.6 MeV)
	$^{103}Rh(n)^{104m}Rh$	12	4.3 min	----
$^{164}Dy(28.18)$	$^{164}Dy(n)^{165}Dy$	2,100	140 min	(1.25 MeV)
	$^{164}Dy(n)^{165m}Dy$	510	1.3 min	----

(continued)

Table II. (continued)

[a] Data are primarily from Ref. 13 and Ref. 22.

[b] 70 keV internal conversion electrons accompany the prompt gamma emission from gadolinium, see Ref. 23.

extremely good resolution since the ranges of the alpha particles emitted following neutron capture are on the order of microns. However, the resulting thickness of the converting layer which is effective in releasing alpha particles to the photographic emulsion is so thin that the efficiency of these materials does not compare favorably with the metallic converters. To increase the efficiency or speed of boron and lithium systems, these materials are commonly mixed with a scintillator such as zinc sulphide and suspended in a plastic or glass matrix. The reaction involved is then (n, α, light). Since these composite converter materials are designed to be at least semi-transparent to the emitted light, the thickness of such a converter can be increased enough to yield speeds as much as fifty times greater than for metallic systems.[25,26]

Lithium fluoride can also be applied to the transfer technique through the use of its thermoluminescent properties. While most of the electrons liberated by passage of the neutron-capture alpha particle recombine immediately after passage of the alpha, some are trapped at defect locations in the crystal lattice. Upon excitation of the lattice, either by heat or ultrasound, the trapped electrons are released and light is emitted as they recombine. In use, a thin sheet of either single or multicrystalline ^{6}LiF is placed in the beam to detect the image. After exposure, the converter is photographed during heating.[27]

In combination with the phosphor, ZnS(Ag), ^{6}LiF has also been used as the basis of a neutron television system which provides dynamic capability. Light emitted by the ^{6}LiF-ZnS(Ag) neutron-converter is collected and focused onto an electron emitting photo-surface by an optical lens. A multistage electron multiplier amplifies the signal and

a phosphor screen converts the amplified signal back to a visual image.[16]

Many of the thermal neutron converting materials are still useful in the epithermal range. Boron, dysprosium, and gadolinium are all 1/v absorbers, so their epithermal performance is essentially the same as their thermal performance except for reduced efficiency due to the decreased neutron absorption cross section. Other materials with absorption resonances in the 1 to 1000 eV range are also useful converters, particularly when used with a monochromatic neutron beam at the principal resonance energy. Through the use of epithermal neutrons, advantage can sometimes be taken of epithermal resonances in one of the test object materials to provide higher contrast than would be obtainable using thermal neutrons.[28] Table III lists several epithermal resonance detectors and their principal resonance energies.

Table III*

Isotope	Principal Resonance Energy (E)	σ(E)	FWHM	$t_{1/2}$
^{115}In	1.46 eV	290 b	0.10 eV	54 min
^{197}Au	4.9	30000	0.23	2.7 day
^{186}W	18.8	14000	0.8	24 day
^{139}La	73.5	175	2.0	40 hour
^{55}Mn	337	2000	40	2.56 hour

*Data from Ref. 4, p. 49.

The effectiveness of thermal and epithermal converting materials falls off to unacceptably low levels for fast neutrons due to the generally low fast neutron interaction cross sections. However, the neutron scattering cross section of hydrogen decreases less rapidly, and scintillators with high hydrogen content such as p-terphenyl, anthracene, or stilbene are commonly used as fast neutron converters in the direct method.[20] Fast neutron radiography is most useful for the imaging of thick specimens when extremely high resolution is not required.

Various other devices and techniques have been explored for neutron radiographic imaging. Among these are a neutron sensitive spark chamber,[29] mechanical scanning using a single small detector,[30] and fiber optic light guides.[31] Although some of these devices possess properties which make them extremely attractive for certain special applications, the bulk of present day neutron radiography is performed using neutron converters in conjunction with either film or image intensifiers.

E. Purpose of Present Research

The purpose of the research described in this thesis was to develop and evaluate a neutron radiographic imaging system based on a multiwire proportional chamber with delay line readouts which would be useful for thermal, epithermal and fast neutron imaging. Multiwire proportional chambers (MWPC) are currently used in high energy physics for particle trajectory measurements and event triggers. Their ability not only to detect ionizing radiation but also to localize the ionizing event makes them extremely useful for radiographic imaging, and they are

being adapted for a variety of biomedical applications including x-radiography and radioisotope imaging.[32] Delay line readout systems developed by Perez-Mendez have achieved better than 1 mm spatial resolution when applied to x-ray multiwire proportional chambers.[33]

A neutron-sensitive MWPC could be extremely useful for neutron radiographic applications not requiring extremely high resolution such as beam alignment, beam profile measurements or measurement of reactor control rod burnup. Since ionizing events are detected individually, there is no threshold on the number of interactions necessary to produce a detectable effect. Thus the MWPC can be used with low intensity sources and does not suffer, as converter-film systems do, from reciprocity failure.[34] The digital nature of the MWPC output makes absolute quantitative measurements relatively simple and the necessary neutron fluences are subject only to the desired counting statistics. The digital capability also provides for either temporary of permanent data storage which would greatly simplify on-line computer image analysis.

II. DESCRIPTION OF EXPOSURE FACILITY

The first efforts in this program to develop an MWPC neutron imaging system were directed toward the construction of a neutron exposure facility. The heart of the facility was a Triga Mark III thermal research reactor licensed to operate at a maximum continuous power of 1.0 Megawatt thermal. At this power the maximum neutron flux in the core is about 4.4×10^{13} $(cm^2\text{-}sec)^{-1}$ with a Cd ratio of 3.0

A. Triga Mark III Reactor

The Triga is a pool type reactor and the pool wall is penetrated by eight tubes for neutron beam extraction. Four of the tubes run tangentially to the core and the remaining four are radial tubes directed toward the center of the core. Although the γ/n flux ratio tends to be higher in beams extracted from a radial port, the total neutron flux is higher and the spectrum is somewhat harder than from a tangential port. Since it was desired to have as high a flux as possible and since the beam was to be used partially for epicadmium measurements, a radial port was chosen in spite of the higher γ-flux. The particular port used for this facility had the added advantage of opening into a three-foot cubicle cavity in the reactor wall where a shutter could be conveniently installed.

B. Beam Collimation

The neutron collimator (see Fig. 5) is a variation of the divergent beam type. Instead of allowing the neutrons to diverge directly from the source (the front face of the primary lead γ-shield in this case), a

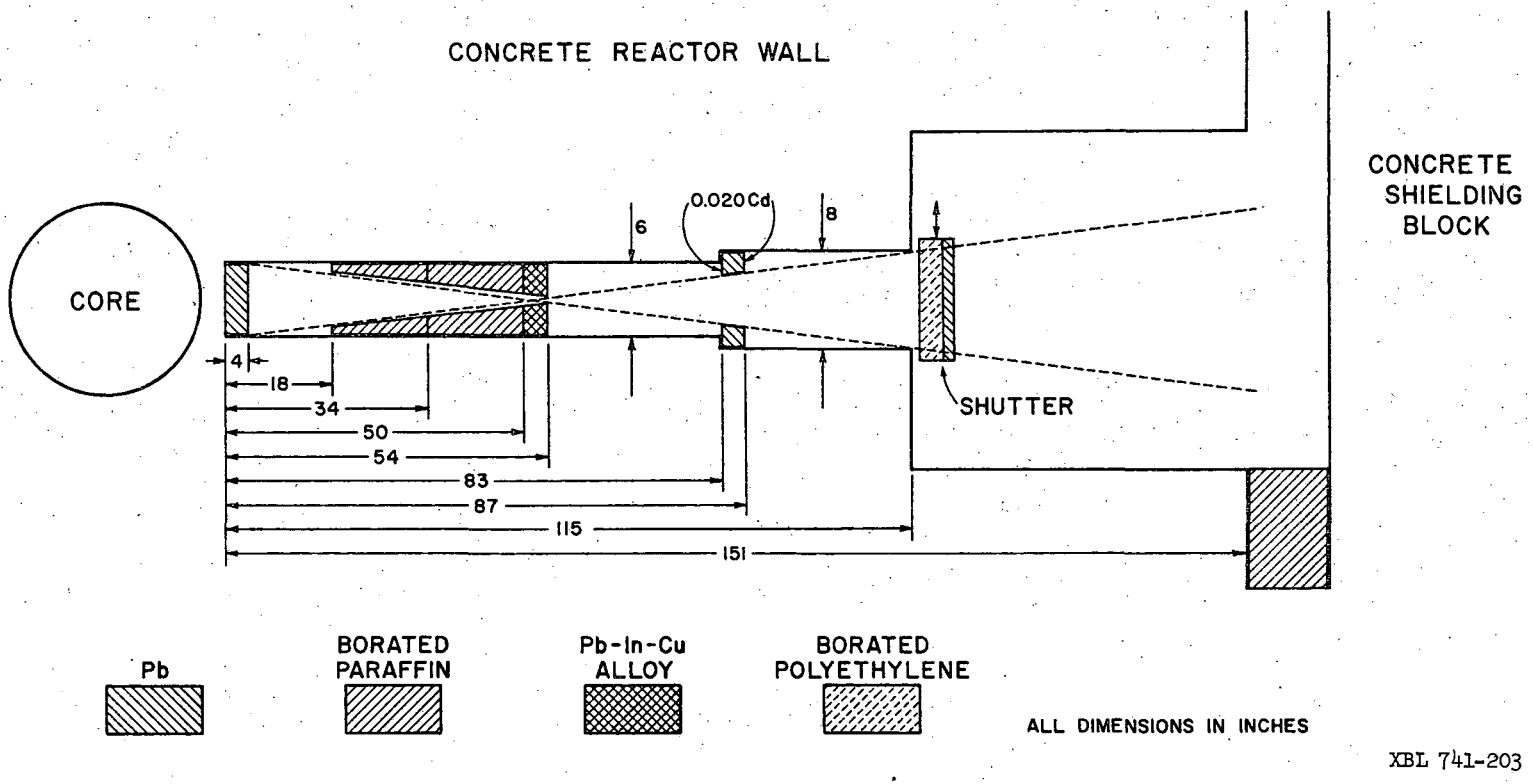

Fig. 5. Beam tube collimation design for radiographic exposure facility.

"pinhole" type collimator is used to move the effective source position further down the beam tube thus increasing the divergence angle of the beam. This allows the diameter of the beam to increase four inches between the front end of the beam tube and the exposure position resulting in a useable beam diameter of about 12 inches.

All shielding and collimation pieces were built into 1/8-inch-thick aluminum cases so they could easily be slid into position in the aluminum beam tube. The first four-inch-thick section of lead is the primary γ-shield. Following this γ-shield are two sections of borated paraffin containing a conical through-hole. These collimators provide pre-collimation of the thermal beam component and are mainly responsible for collimation of the epithermal component. After the paraffin comes a section of In-Cd-Pb alloy (2.2:0.52:130 by weight respectively) which provides the final collimation by reducing the beam diameter from 1.00 inch to 0.50 inches. Since indium is a convenient transfer material with a large absorption resonance at 1.5 eV, it was desired to have the indium resonance portion of the beam reasonably well collimated for epicadmium transfer imaging. The cadmium, or course, works on the thermal portion of the spectrum and the lead attenuates the capture-γ's. Four more inches of lead are located at the beam tube step to attenuate the γ's which stream down the gap between the collimator and shield cases and the beam tube wall. The lead is faced on both sides with annular pieces of 0.020-inch-thick cadmium sheet to remove any stray thermal neutrons which might be present. The effective source size of 0.50-inch-diameter in combination with an effective source-to-detector distance of 100 inches limits the angular divergence as seen by a point in the detector plane to $d/L \approx 0.005$ radians or about 0.3°.

Neutron fluxes at the exposure position were measured using β-γ coincidence-counting of gold foils. Three sets of foils (a set consists of one bare foil and one encapsulated in 0.020-inch-thick Cd) were located at different radial positions in the beam. The foil irradiation was 30 minutes long at a reactor power of 1.0 Megawatt which resulted in a maximum foil activity of about 0.1 μCi. The results of these measurements are plotted in Fig. 6. The curves are the general beam profiles indicated by later measurements with the MWPC and by optical densitometer scans of film images of the beam taken with a gadolinium converter. They have been normalized to the gold foil calibration points. The outermost portions of the curves are dotted because no separate epithermal film data was taken in this region. However, by attributing the Gd-film response in the outermost regions to the epithermal flux, the resulting shapes are compatible with the expected degree of collimation for the two spectral components. For an ideal pinhole collimator made of a material which is 100% absorbing to the radiations involved, the flux shape at the exposure position would simply be a projection of the flux distribution present at the real source plane. However, the flux shapes presented in Fig. 6 have folded into them the effects due to the finite cross sections of the collimation materials and the finite aperture size.

C. Shutter

In order to control exposure times and to allow experiments to be changed without scramming the reactor, a shutter was designed which could be positioned in front of the beam port exit. It is 10 × 10 inches square

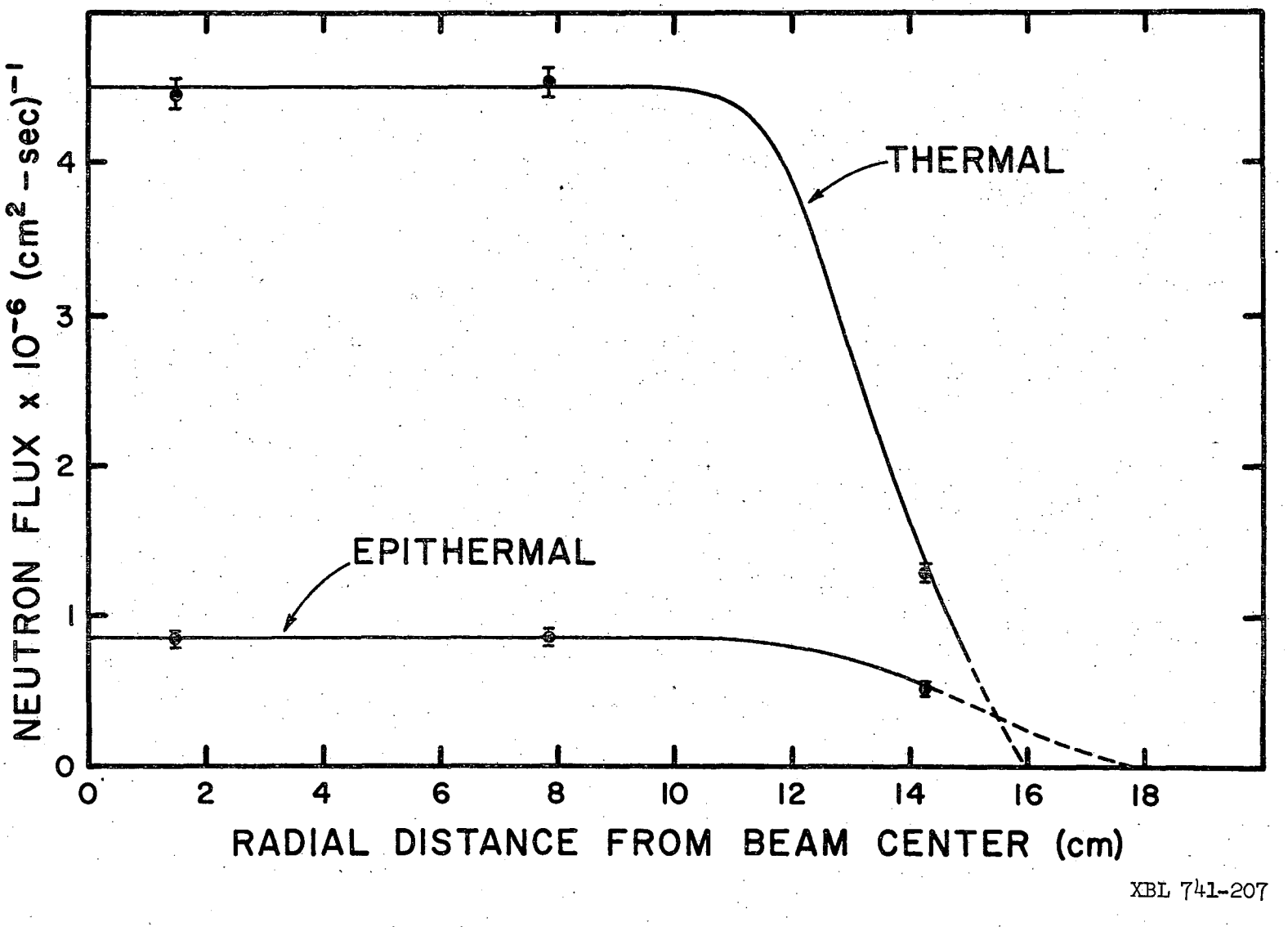

Fig. 6. Reactor beam flux profiles (thermal and epithermal).

and consists of four inches of borated polyethylene for neutron attenuation followed by two inches of lead for core-γ and capture-γ attenuation. The attenuators are contained by a steel frame mounted on wheels which run on inclined steel tracks across the front of the beam port. Fail-safe operation is thus obtained, for if the controlling mechanism should fail, the shutter automatically returns to the closed position.

In the closed position, the shutter was effective in reducing the thermal neutron flux reaching the detector by at least a factor of 2000. The count rate due to the epithermal flux was reduced by a factor of about 40 (measured with a boron-sensitized MWPC) and the count rate due to the decay-γ spectrum was reduced by about a factor of 250.

D. Experiment Holder and Shielding

Two 3 × 3 × 4 foot concrete shielding blocks were positioned in front of the beam port with the bottom block adjacent to the reactor wall and the top block set back eight inches to form a space in which the experiments could be placed. The space was closed on the left and top, as shown in Fig. 7, by an "L" shaped sheet-metal can filled with borated paraffin, the same material used in the collimators.

The experiment holder was fitted with four rollers which ran on steel tracks across the top of the exposure space. The left half of the holder is used for mounting the experiment or sample and the right half of the holder was enclosed with sheet-metal and filled with more borated paraffin. When the holder is rolled into the exposure space, the experiment is positioned in front of the beam and the shielding is completed. Microswitch interlocks were employed to scram the reactor if an attempt was made to roll the holder out of beam position while the shutter was open.

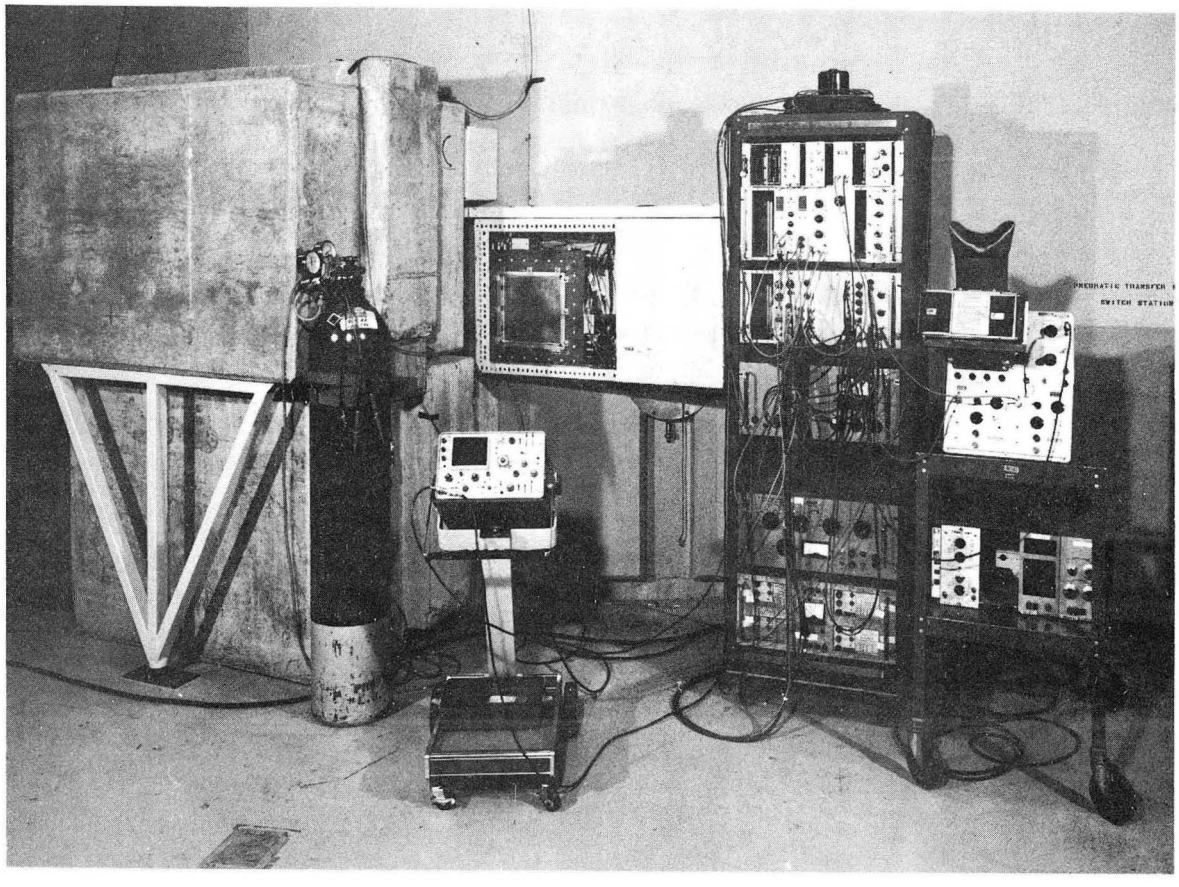

XBB-742-855

Fig. 7. Exposure facility. The 10 × 10 inch MWPC is shown mounted in the experiment holder.

E. Commercial Image Detector

An image detector completes the neutron radiographic facility. The first type of detector used was a 14 × 17 inch commercial vacuum cassette purchased from Research Chemical (Fig. 8a). The converting surface was a 25 μm-thick-coating of gadolinium oxide flame-sprayed onto an aluminum substrate. In use, the cassette is first loaded with a sheet of x-ray film and then attached to a vacuum pump and evacuated. Atmospheric pressure holds the thin aluminum cover, the film and the converting surface in close contact. The loaded cassette is then placed in the experiment holder, along with the object to be radiographed, for exposure.

Figure 8b shows a thermal neutron radiograph of an electric hand drill taken with the vacuum cassette. Kodak Type M x-ray film was used and the exposure required a total neutron fluence of about $10^9/cm^2$. Figure 8c is an x-radiograph of the same hand drill taken at a KVP of 100. The complimentary nature of thermal neutron and x-radiography shows up nicely here. While the x-radiograph emphasizes metallic parts, the neutron-radiograph emphasizes hydrogenous areas. For instance, the x-radiograph clearly shows the gears in the gearcase and the copper conductors in the wires. On the other hand, the neutron radiograph shows the grease in the gearcase and the rubber insulation covering the copper conductors. Note also the nylon screw in the chuck.

Aside from being an interesting study from the radiographic standpoint, Fig. 8b also demonstrates that the beam collimation is tight enough to easily resolve distances much smaller than a mm (note the screw threads). Because a mm or two is the order of resolution expected from

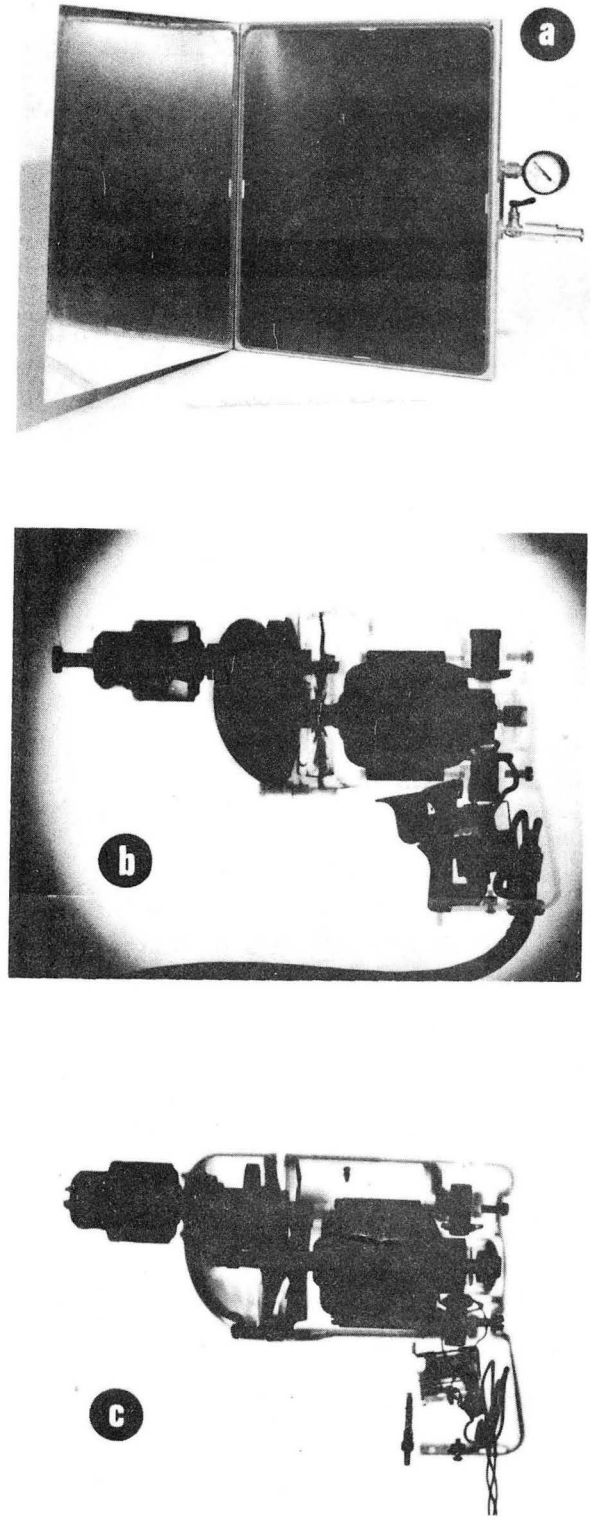

XBB-742-1068

Fig. 8. (a) Gadolinia vacuum cassette for neutron radiographic imaging, (b) thermal neutron radiograph of electric hand drill taken with vacuum cassette, (c) x-radiograph of hand drill.

the MWPC neutron imaging system to be described, image degrading effects due to imperfect beam collimation could be ignored.

III. DESCRIPTION OF MWPC IMAGING SYSTEM

A. Multiwire Proportional Chamber

Conceptually, the MWPC can be thought of as an array of single-wire proportional counters placed side-by-side with the circular cathodes broken in the plane of the anode wires and folded back to form plane cathodes (see Fig. 9). Although this process alters the electric field configuration somewhat, the process of proportional multiplication is still basically the same as in the single wire counters. Multiplication can occur on individual anode wires and by AC decoupling the wires, the perpendicular coordinate of an ionizing event can be determined by detecting on which wire or wires pulses occurred.

1. Electron Drift and Multiplication

Let us follow the sequence of events leading to the detection and localization of a 5.9 keV photon (^{55}Fe source) by the MWPC depicted in Fig. 9c, with an anode radius, r_o, of 6.3 μm; a wire spacing, s, of 1.5 mm; and a plane spacing, L, of 3 mm (geometric parameters for 10 × 10 inch MWPC). Assuming that one of the cathodes is thin enough to act as a window, the photon can get into the gas filled sensitive volume of the chamber where it undergoes photoelectric conversion on a gas molecule, for instance, on argon. Since the ranges of the 2.7 keV photoelectron and the 88% probable 2.7 keV Auger electron are much less than a mm, the kinetic energy will usually be deposited somewhere in a sphere of this radius and centered on the conversion point. An average energy of about 25 eV is required to create an ion-electron pair in most proportional counter gases so about 240 pairs will be created by the 5.9 keV photon.

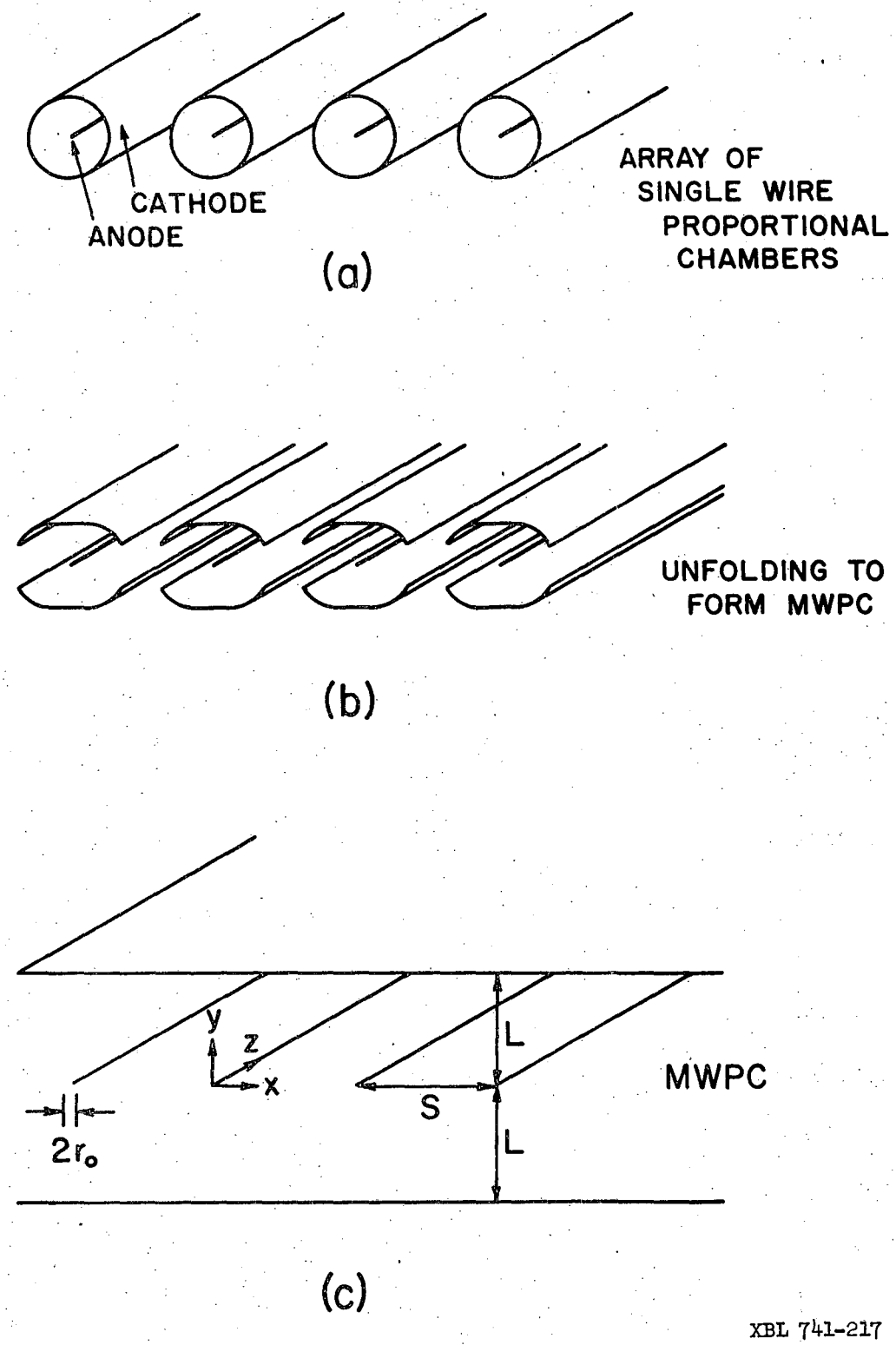

Fig. 9. Conceptual diagram of MWPC and graphic definition of MWPC geometric parameters.

Under the influence of the electric field, the pairs will separate with the electrons drifting toward the positively charged anodes and the ions toward the nearest cathode. The electric potential and field distributions in an MWPC have been calculated by Erskine[35] for the rather general cases of wires of finite thickness, displacements of single wires and local variations in wire diameter. However, for the approximation that the wires are infinitely thin (a good approximation for the case considered here), a solution of Laplace's equation, $\nabla^2 W = 0$, yields for the complex potential,

$$W(z) = 2q\left[\frac{\pi(iz-L)}{s} - \ln\frac{\theta_1(\pi z/s,p)}{\theta_1[\pi(z+2iL)/s,p]}\right] \qquad (1)$$

where $p = \exp(-4L/s)$, $\theta_1(u,p) = 2p^{\frac{1}{4}}(\sin(u) - p^2\sin(3u) + p^6\sin(5u) - \ldots)$ and z is the complex coordinate, x + iy. For the case, L > s, the following expression is a good approximation for the real potential, $V(x,y) = \mathrm{Re}[W(z)]$.[36]

$$V(x,y) \approx q\{2\pi L/s - \ln[4\sin^2(\pi x/s) + 4\sinh^2(\pi y/s)]\} \quad . \qquad (2)$$

The constant, q, is the charge per unit length on a wire and can be determined by requiring that the actual wire surface defined by $x^2 + y^2 = r_o^2$ be an equipotential surface at the applied voltage, V_o. This requirement yields

$$q \approx \frac{V_o}{2[\pi L/s - \ln(2\pi r_o/s)]} \quad . \qquad (3)$$

The electric field components are obtained by taking the negative gradient of V(x,y) which gives

$$E_x(x,y) = -\frac{\partial V}{\partial x} = \frac{\pi q \sin(2\pi x/s)}{s[\sin^2(\pi x/s) + \sinh^2(\pi y/s)]} \qquad (4a)$$

and

$$E_y(x,y) = -\frac{\partial V}{\partial y} = \frac{\pi q \sinh(2\pi y/s)}{s[\sin^2(\pi x/s) + \sinh^2(\pi y/s)]} \quad . \qquad (4b)$$

Figure 10 shows the general nature of the field lines and the equipotentials for the geometry under consideration. Two important features are the following:

1. Close to the wire where $x < s$ and $y < s$, the total electric field strength, $E = \sqrt{E_x^2 + E_y^2}$, is given by

$$E = \frac{2q}{\sqrt{x^2 + y^2}} = 2q/r \qquad (5)$$

irrespective of the azimuthal angle. This rapid, 1/r increase of the field close to the wire is the same condition encountered with single wire proportional counters.

2. From Eqs. (4a) and (4b) it can be shown that

$$E_y(0,y) = 2\pi q \coth(\pi y/s)/s \qquad (6a)$$

and

$$E_y(s/2,y) = 2\pi q \tanh(\pi y/s)/s \quad . \qquad (6b)$$

The fractional variation in the y-component of electric field at constant y is then

$$\frac{E_y(0,y) - E_y(s/2,y)}{\frac{1}{2}[E_y(0,y) + E_y(s/2,y)]} = \frac{\coth(\pi y/s) - \tanh(\pi y/s)}{\frac{1}{2}[\coth(\pi y/s) + \tanh(\pi y/s)]} \quad . \qquad (7)$$

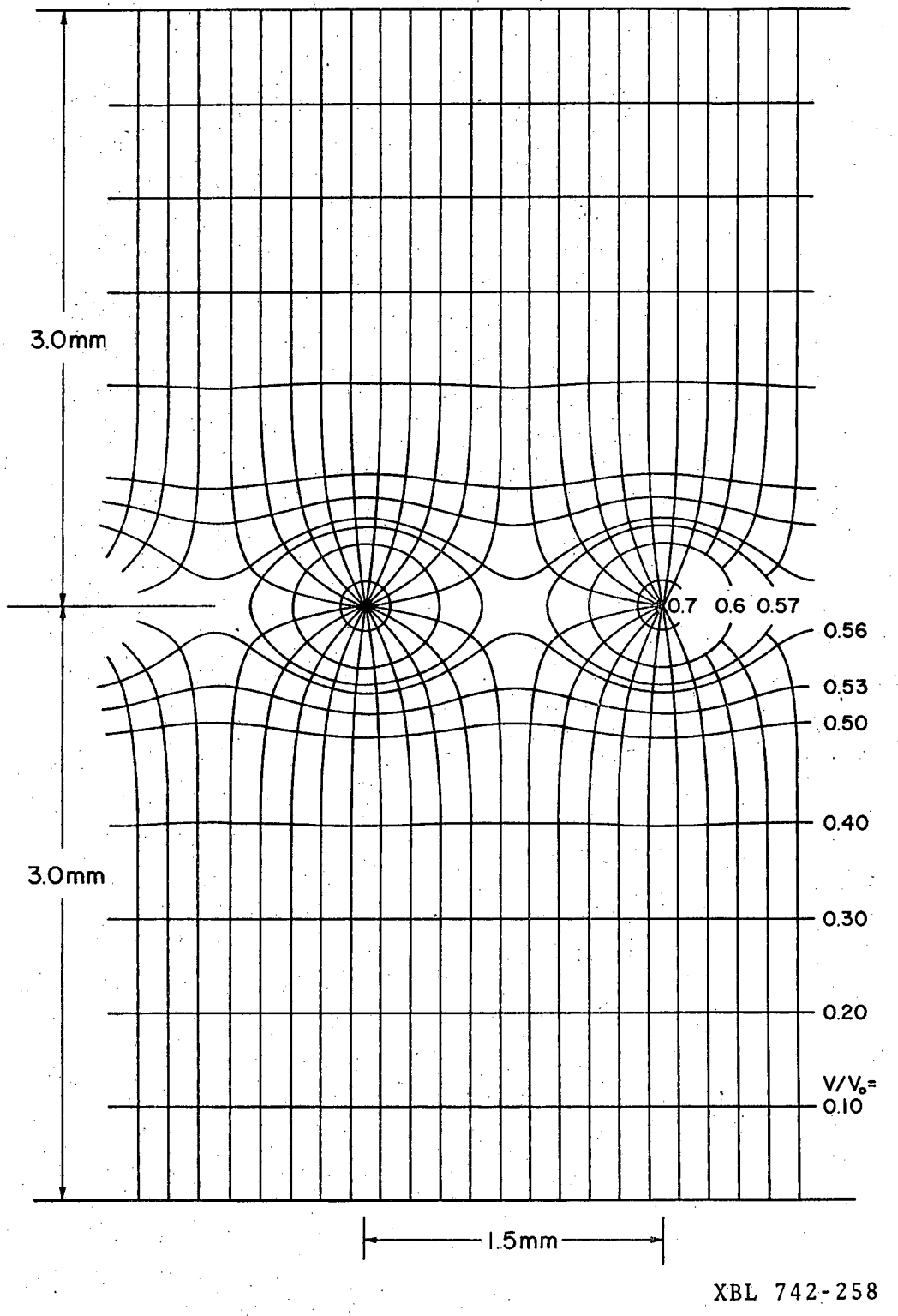

Fig. 10. Equipotentials and electric field lines in MWPC.

For $y \geqslant s$, the fractional variation is less than 1% and the ratio, E_y/E_x, is greater than 250.

Thus the field in an MWPC varies as $1/r$ near the wires and is nearly uniform for $y > s$.

Ion drift velocities in an electric field are proportional to the electric field strength making it possible to define an ion mobility, μ, such that $\vec{v}_{drift} = \mu\vec{E}/p$, where p is the pressure of the gas. Table IV gives a few representative values for ion mobilities in several different gases. The units of mobility are (mm-Hg)(cm/sec)(volt/cm)$^{-1}$.

Table IV*

Gas	μ^-	μ^+
Air	1350	1070
Argon	1290	1040
Hydrogen	6500	4300
Nitrogen	1380	980
CO_2	720	600

The dependence of electron drift velocity on electric field is not so simple, as demonstrated by Fig. 11a, which shows electron drift velocity as a function of E/p for pure argon, pure methane, and a mixture of 90% argon and 10% methane (a very common mixture for proportional counters). The more complicated functional dependence on electric field in this case is due to the larger variety of energy exchange mechanisms available to the electron.

*Mobility values from Ref. 38, p. 73.

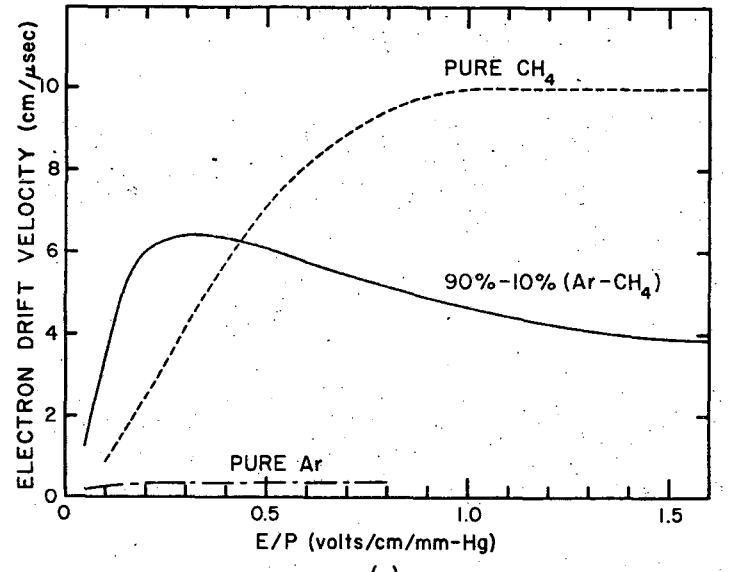

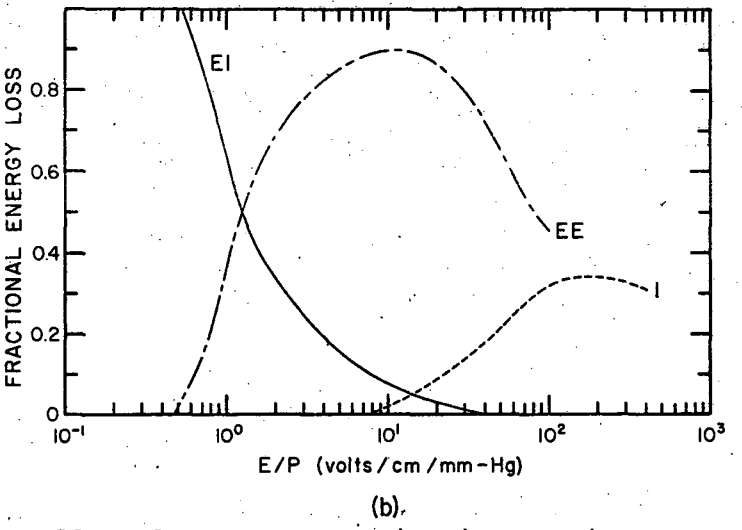

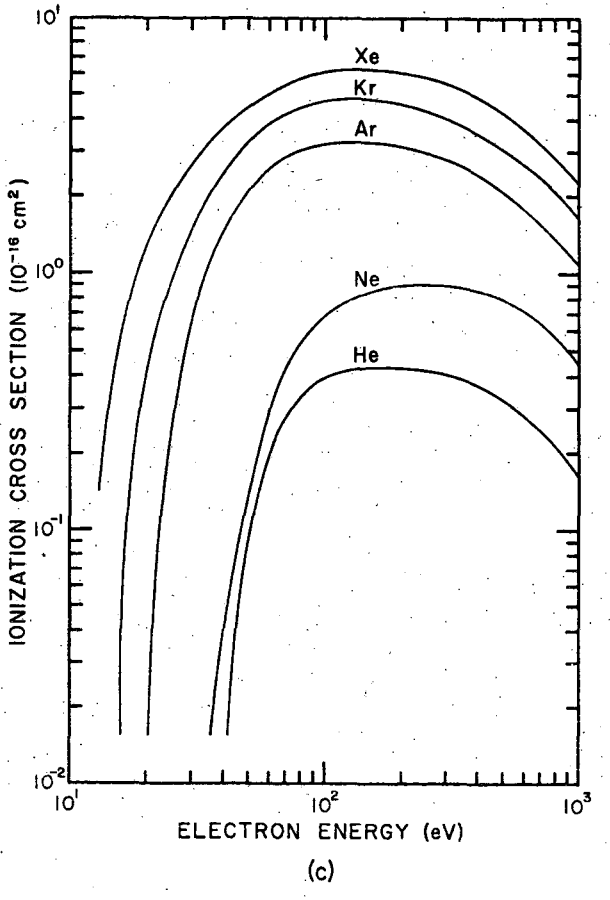

XBL-741-202

Fig. 11. Electron properties in counting gases. (a) Drift velocity in argon-methane mixtures (Ref. 39). (b) Fraction of electron energy going to different loss mechanisms in argon. El=loss to elastic impacts, EE=excitation of electronic levels leading to light emission and metastable states, I=ionization by direct impact (Ref. 40). (c) Ionization cross sections for noble gases (Ref. 41).

Figure 11b shows the relative importance of the various exchange mechanisms as a function of E/p in pure argon. The presence of methane in the argon provides an additional mechanism for energy exchange by excitation of low energy vibrational and rotational levels not present in pure monatomic argon.[37] This low-energy-loss mechanism lowers the electron temperature to a point where high energy loss interactions with argon become improbable and thus the drift velocity is increased. Another beneficial effect derived from this mechanism is the large cross section for absorption of photons released following electronic excitation. These photons are essential to the operation of a Geiger tube since they are responsible for propagating the discharge down the length of the anode. However, they would be very troublesome if left unchecked in a proportional system.

Returning once again to the MWPC of Fig. 9c, it is instructive to estimate the electric field strengths at several points in the chamber to get an idea of the electron and ion drift velocities. Using the values for V_o, r_o, s and L of 2.2 kV, 6.3 μm, 1.5 mm and 3 mm respectively, Eq. (3) yields 0.123 nanocoulomb/cm for the charge per unit wire length. Inserting this q-value into Eq. (5) yields

$$E(r) = 221/r \text{ volts/cm} \qquad (8a)$$

very near the wire, and Eq. (6a) or (6b) gives a value of 4640 volts/cm in the uniform field region. At STP, the corresponding E/p values are

$$E(r) = 0.281/r \text{ (volts/cm)(mm-Hg)}^{-1} \qquad (8b)$$

and 6.10 (volts/cm)(mm-Hg)$^{-1}$.

Assuming that the photoelectric conversion occurs in the uniform field region, the ions will drift toward a cathode at about 0.006 cm/μsec and the electrons will drift toward the anode plane at about 4 cm/μsec. So it takes at most about 60 nsec for the electrons to drift to a point where the field begins to vary as 1/r. As the field increases, the electrons are able to accumulate more and more energy between collisions. Figure 11c shows that the ionization cross section for argon rises rapidly for electron energies in the 20-30 eV range, and eventually, the mean-free-path for ionization becomes sufficiently short that this process can compete favorably with the other energy loss mechanisms. Once an electron is released by ionization, it is just as effective as the original secondaries in causing further ionization, and thus an electron avalanche is initiated which grows until it reaches the wire.

The problem of electron gain in a proportional multiplication process has been treated by Rose and Korff.[42] By making the simplifying assumptions that

(1) photoelectric emission at the cathode is negligible

(2) recombination and electron attachment to neutrals are negligible

(3) fluctuations in energy loss and in specific ionization are negligible

they obtained

$$A = \exp\left\{2\sqrt{\frac{aN_m r_o V_o}{\pi L/s - \ln(2\pi r_o/s)}}\left[(V_o/V_t)^{\frac{1}{2}} - 1\right]\right\}, \qquad (9)$$

where the parameters of this discussion have been inserted when appropriate. A is the electron gain, a is the rate of increase of the ionization cross section with energy (cm^2/volt) and N_m is the molecular density (cm^{-3}). V_t is the threshold voltage for electron multiplication; for anode voltages less than V_t, the chamber operates as an ionization chamber. Equation (9) is plotted in Fig. 12 using the value for a in argon of 1.8×10^{-17} cm^2/volt and V_t = 800 volts (estimated value for 10 × 10 inch chamber).

An intermediate result in Rose and Korff's derivation shows that

$$V_t/r_o = V_o/r_c \qquad (10)$$

where r_c is the critical radius at which ionization begins. It has already been shown that the field near the wire is proportional to q/r or V_o/r. Equation (10) is simply a statement of the fact that ionization is possible beyond some critical value of the electric field. With r_o = 6.3 μm, V_t = 800 volts, and V_o = 2.2 kV, Eq. (10) gives a value of 17.3 μm for r_c. Thus, the avalanche is confined to a very small radial distance from the wire. Charpak has observed that the avalanche surrounds the wire for reasonably large amplification factors[43] and the lateral extent due to a single secondary is probably about the same as the avalanche diameter.

Although Fig. 12 indicates that the electron gain can be increased indefinitely simply by raising the high voltage, this is not the case. When the charge of the ion sheath becomes a significant fraction of the charge on the wire, the local electric field is diminished and the gain

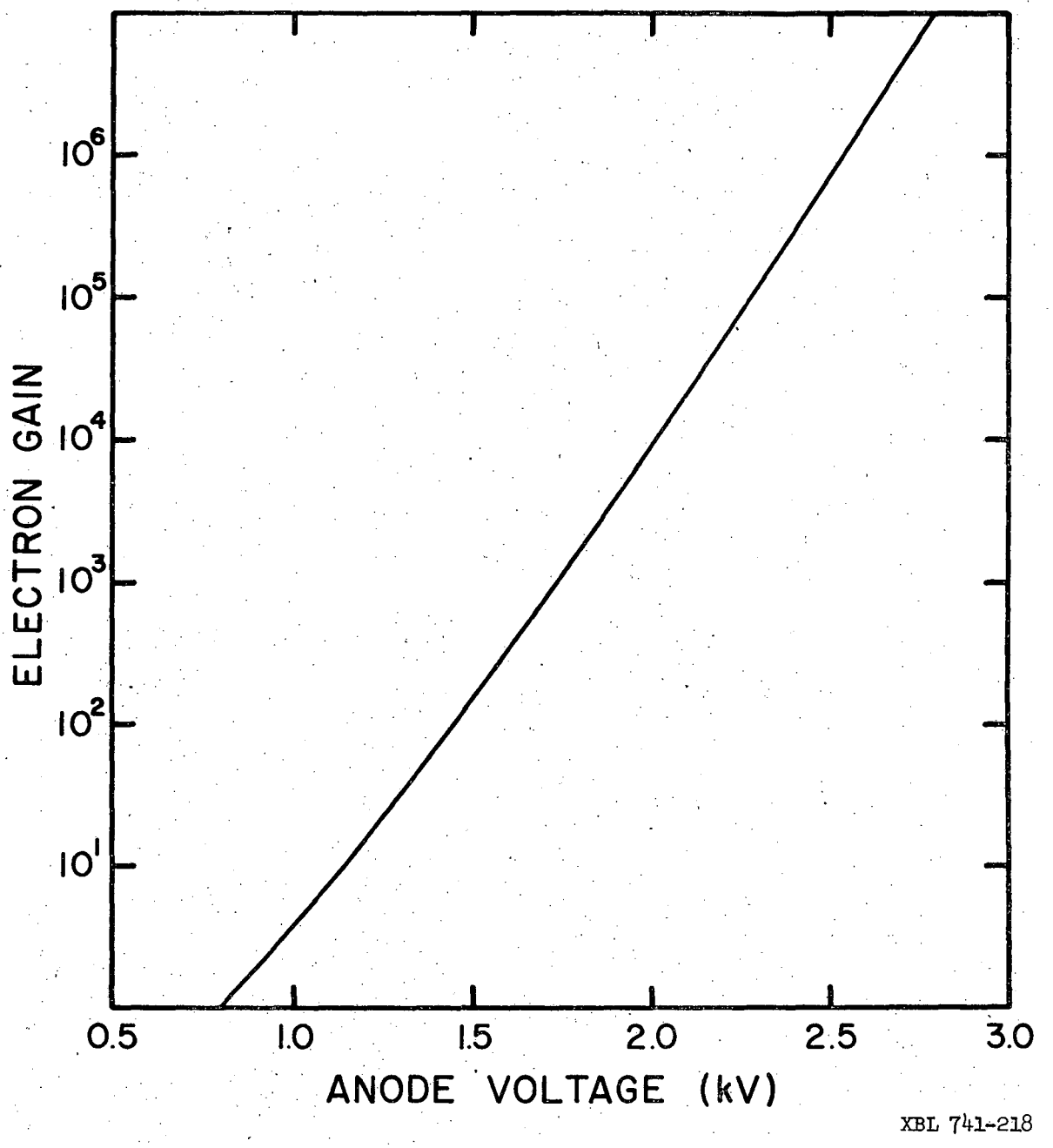

Fig. 12. MWPC electron gain as a function of anode voltage.

begins to saturate. A 10% effect should be noticeable corresponding to about 0.0123 nanocoulomb/cm or 7.70×10^6 ions/mm for the previously calculated q of 0.123 nanocoulomb/cm. Since the electrons from the 5.9 keV photon will certainly show signs of saturation at $A = 7.70 \times 10^6/2.4 \times 10^2 = 3.2 \times 10^4$. For smaller amounts of initial ionization or when the initial ionization is distributed over a larger distance, this value will be higher.[44]

2. Formation of Induced Pulses

A common belief is that the anode pulse arises from collection of the avalanche electrons. However, due to the close proximity of the avalanche to the wire and the fact that over half of the electrons are formed in the last mean-free-path, the work required to collect the electrons is very small compared to the work expended in drifting the ions all the way back to the cathodes. In fact, the major contribution to pulse formation in a proportional chamber is due to ion drift which induces negative charge on the avalanche anode, and positive charge on the cathodes and neighboring anodes.

If the simplifying assumption is made that all ions are formed at the wire surface so the anode charge is induced by expansion of the resulting cylindrical sheath, a simple expression can be derived for the anode current as a function of time. By definition, the ion drift velocity is

$$v_{drift} = \frac{dr}{dt} = \mu E/p = 2\mu q/rp \rightarrow \int_{r_o}^{r} r'dr' = \int_{0}^{t} 2\, qdt'/p \rightarrow$$

$$r(t) = r_o \sqrt{1 + 4\mu qt/pr_o^2} = r_o \sqrt{1 + t/t_o} \qquad (11)$$

where $t_o = pr_o^2/4\mu q$ and r(t) is the radius of the sheath for times small enough that the ions are still in the 1/r field region. Examination of the field lines and equipotentials in Fig. 10 shows the field to be approximately radial for $r \lesssim 0.2$ s. So Eq. (11) should be valid for $t \lesssim t_o(0.04\ s^2/r_o^2 - 1) \approx 1.6$ μsec. Since the pulse coupling networks that are commonly used have time constants on the order of several hundred nsec, this covers the time interval of interest.

There will be N = 240A ions in the sheath, and an amount of energy, $dW = NeE(r)dr$, must be expended to move the sheath from r to r + dr. This energy is derived from the high voltage which supplies a charge, dQ, to the anodes at a potential, V_o. Thus,

$$V_o dQ = NeE(r)dr \quad \text{and} \quad \frac{dQ}{dt} = i(t) = \frac{NeE(r)}{V_o}\frac{dr}{dt}$$

so

$$i(t) = \frac{NeE^2(r)\mu}{pV_o} = \frac{Ne\mu}{pV_o}\frac{4q^2}{r^2(t)} = \frac{Neq}{V_o}\frac{1}{t - t_o} \qquad (12)$$

for $t \lesssim t_o(0.04\ s^2/r_o^2 - 1)$. In accordance with the assumption that the avalanche surrounds the wire, half of the ions will drift to each cathode. While the sum of all positive induced currents must be equal in magnitude to the negative anode current (Eq. (12)), the ratio of positive induced cathode current to positive induced current on neighboring anodes is a function of s/L. Very roughly, this ratio is about 1 for typical s/L values[45] (0.2 to 0.5), and is directly related to s/L. Approximately then, 25% of the positive induced current goes to each nearest neighbor anode and 25% to each cathode. The anode and cathode currents are exactly

correlated in time because they are both due to the same charge displacement.

Neglecting diffusion, the electric field lines of Fig. 10 are the trajectories for ion and electron drift. Thus, detection of a current on the anode located at $x = 0$ signifies that the ionizing event occurred in the interval $-s/2 \leqslant x \leqslant s/2$. Hence the spatial resolution which can be obtained by detecting individual anode pulses is $s/2$ or half the wire spacing. Avalanches can occur anywhere along the length of an anode wire (z-direction) and since $\frac{\partial V(x,y)}{\partial z} = 0$ everywhere in the chamber, ion-electron drift occurs along lines of constant z. Thus an electron formed at $z = z_o$ will produce an avalanche at $z = z_o$ and the resulting ions will be collected at the cathode at $z = z_o$. If a cathode is divided into thin strips running in the z-direction, the z-coordinate of an ionizing event can be obtained by the detection of induced currents on individual strips.

In principle, currents will be induced on every one of the strips, but the largest current will occur on the strip (or strips) which lies directly beneath the avalanche (see Appendix A). By reading out all the cathode strips simultaneously, the z-coordinate can be determined by interpolation for the maximum pulse height, and so, to a first approximation, spatial resolution in the z-direction is independent of the width chosen for the cathode strips.

In practice, wires are usually used in place of flat cathode strips (for transparency to low energy radiation). While this will produce major alterations in the field configuration near the cathodes, the field in the region of ion drift germane to fast pulse formation will be essentially the same.

B. Detection and Amplification of MWPC Output Pulses

Although the anode and cathode currents can be integrated and detected with charge-sensitive amplifiers, the long ion-collection time (50-150 μsec in a typical chamber) requires that the integration-time of the amplifier be rather long in order to collect a significant fraction of the total charge. Because of the resulting wide pulses, repetition rates must be kept relatively low to avoid pulse addition effects. For fast pulse applications, advantage is taken of the fast rise-time of the anode and cathode currents by coupling these signals to voltage amplifiers through a differentiating network.

Equation (12) implies that the anode-cathode currents rise infinitely fast ($i(0^-) = 0$; $i(0^+) = Neq/V_o t_o$) because of the assumption that all ions begin drifting from the wire surface at $t = 0$. Actually, the current will rise during the time that the avalanche grows, which, for a single initiating electron, is on the order of nanoseconds. If the initial ionization is spread over a finite distance (as in the track of a charged particle or simply due to electron diffusion during drift) then the current will rise more or less linearly until all the electrons have drifted to the anode. Thus the rise-time can be as long as several hundred nsec depending on the thickness of the chamber and the nature of the radiation.

A typical network for coupling an anode wire to a voltage amplifier is shown in Fig. 13. C_g is the stray anode capacity to ground. When the anodes are AC decoupled from each other, C_g is the sum of the capacitive coupling to the cathodes plus the capacitive coupling to nearest-neighbor anodes. The cathode-coupling is simply $q\ell/V_o$ where ℓ

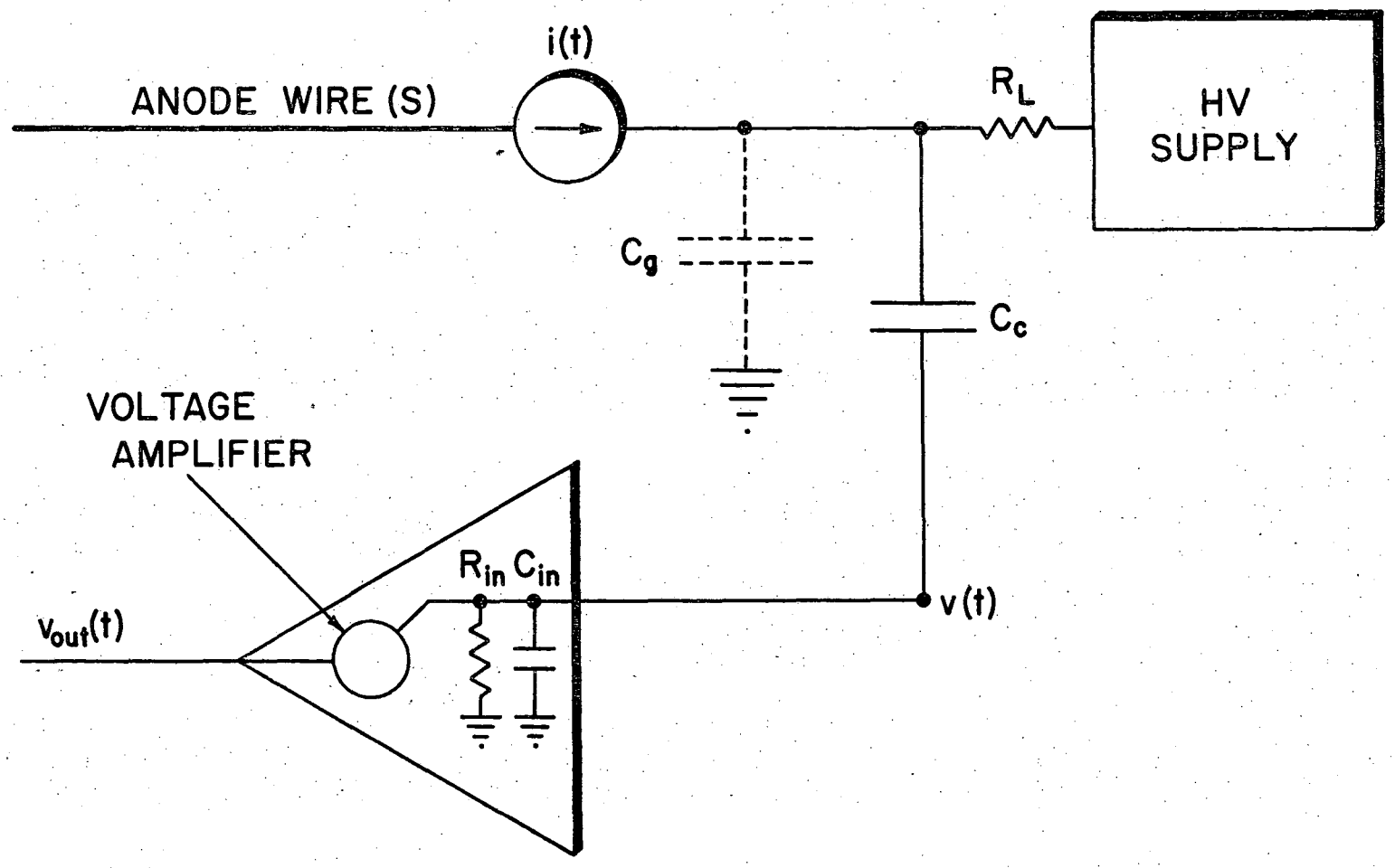

XBL 741-215

Fig. 13. Anode pulse coupling circuit.

is the length of the wire. The capacity between two parallel wires of radius r_o and separated by a distance, s, is $\frac{\ell}{4\cosh^{-1}(s/2r_o)}$ [46] and the anode to nearest-neighbor capacity will be of this order. Using the chamber parameters discussed in the previous section and a wire length of 25 cm, $q\ell/V_o$ = 1.4 pF and $\frac{\ell}{4\cosh^{-1}(s/2r_o)}$ = 1.3 pF. If an additional capacity on the order of 1 pF is assumed for end-effects where the wires are fastened to the dielectric frames, C_g will be about 4 pF per wire. If all the anodes are tied together, then $C_g = \frac{\ell}{s}(q\ell/V_o + C_{\text{end-effect}}) \approx 350$ pF for a 25 by 25 cm square chamber. The impedance of the high voltage limiting resistor, R_L, is large enough that it can be ignored for analytical purposes. C_c couples the signal to the amplifier which has an input resistance and capacitance of R_{in} and C_{in} respectively. The differential equation for the voltage at the amplifier input is

$$\frac{dv}{dt} + \frac{v}{\tau_2} = \frac{\tau_1}{\tau_2}\frac{i(t)}{C_g} \tag{13}$$

where $\tau_1 = \frac{R_{in}C_cC_g}{C_c + C_g}$ and $\tau_2 = \tau_1 + R_{in}C_{in}$. Substituting for i(t) from Eq. (12) and solving yields

$$v'(t) = \frac{Neq\tau_1}{V_oC_g\tau_2}\exp[-(t + t_o)/\tau_2]\int_{t_o/\tau_2}^{(t + t_o)/\tau_2}\frac{\exp(\xi)d\xi}{\xi} \quad . \tag{14}$$

If the ions are not all formed simultaneously but as a function of time, R(t), then R(t)dt ions will begin drifting from the anode between t and t + dt and the voltage is given by the convolution of R(t) and v'(t) or

$$v(t) = \int_0^t R(t')v'(t - t')dt' \quad . \tag{15}$$

A simple and not too unrealistic form for R(t) is

$$R(t) = \begin{cases} N/T \text{ for } 0 \leqslant t \leqslant T \\ 0 \text{ for } t > T \end{cases} \quad . \tag{16}$$

Substituting Eq. (14) and Eq. (16) into Eq. (15) gives

$$v(t) = V_m \int_0^t \exp[-(t - t' + t_o)/\tau_2]\frac{dt'}{T} \int_{t_o/\tau_2}^{(t - t' + t_o)/\tau_2} \frac{\exp(\xi)d\xi}{\xi} = V_m f(t) \tag{17}$$

where $V_m = \dfrac{Neq\tau_1}{V_o C_g \tau_2}$. The function, f(t), is displayed in Fig. 14a for various values of τ_2 with t_o = 0.72 nsec and T = 50 nsec. The pulses are seen to rise linearly for a time, T, and the tails can be made much shorter than a μsec by proper choice of circuit time constants or by a second differentiation following amplification. An important feature of the MWPC is that the presence of one pulse on an anode wire does not preclude the possibility of another avalanche forming at some other position on the same wire. Detection of the two pulses requires only that they be separated by the resolving time of the electronics. Thus the MWPC does not suffer from the long dead-time inherent in spark chambers and Geiger tubes.

For the experimental set of circuit component values C_g = 5 pF, C_c = 100 pF, R_{in} = 1.5 kΩ and C_{in} = 25 pF, and taking N as 10^7

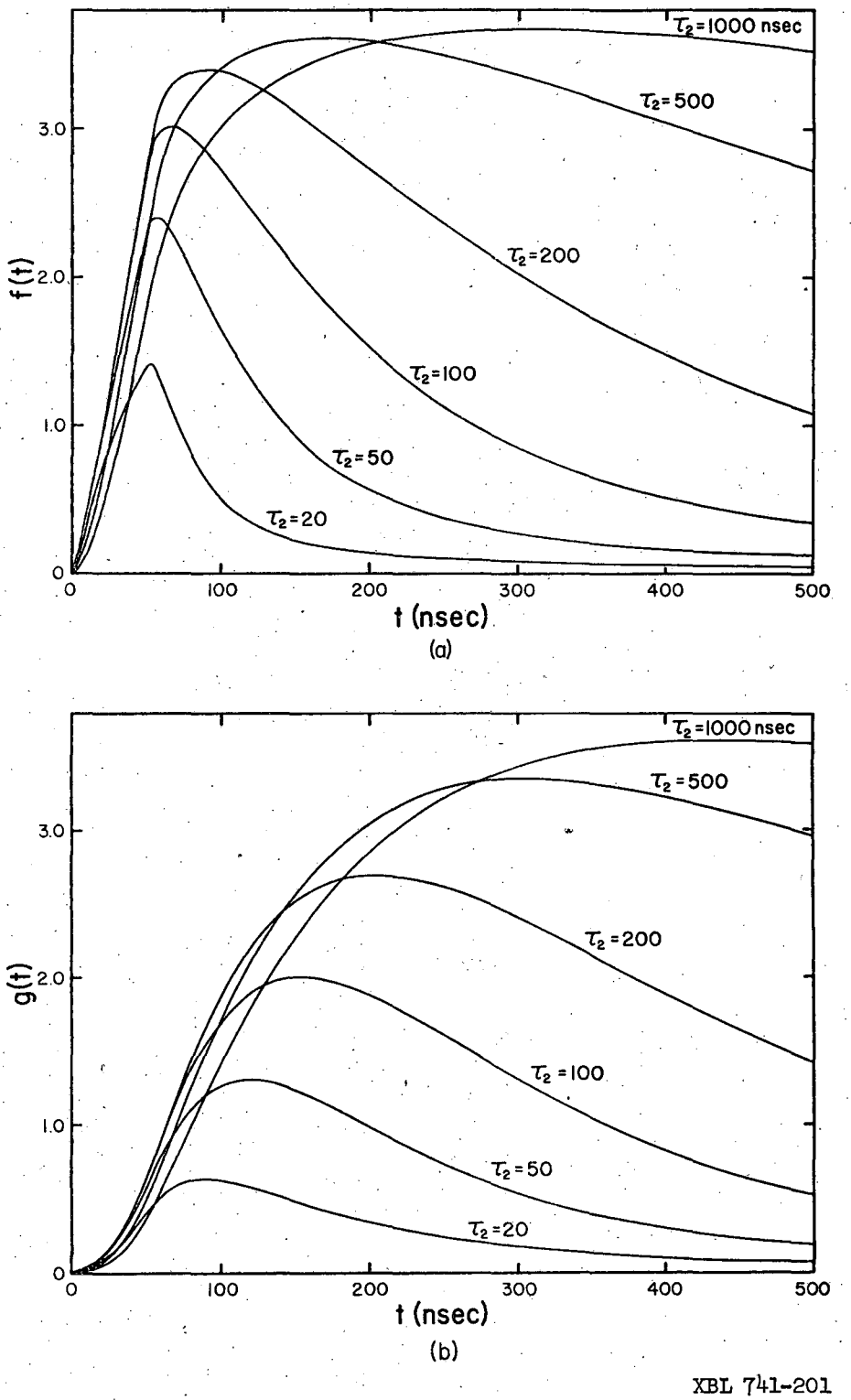

Fig. 14. MWPC pulse shapes at (a) input to amplifier and (b) output from amplifier with a risetime of 80 nsec.

(corresponding to a gain of 4×10^4 for a 5.9 keV ^{55}Fe x-ray), τ_2 = 46 nsec and V_m = 2.6 mV. Figure 14a shows that the maximum pulse height will be about 6.2 mV. When the anodes are bussed together so that C_g = 350 pF, then τ_2 = 150 nsec and V_m = 0.20 mV. In this case, Fig. 14a indicates a pulse height of about 0.62 mV. Thus, a rather severe penalty in peak pulse amplitude must be paid when the common anode configuration is used to supply a pulse which signifies the occurrence of an event anywhere in the chamber. Figure 14b shows the approximate pulse shapes that can be expected at the output of an amplifier whose transfer characteristic has been modeled as a simple exponential rise-time, τ_A, of 80 nsec, so

$$v_{out}(t) = (\text{DC voltage gain}) \times \frac{\exp(-t/\tau_A)}{\tau} \int_0^t v(t')\exp(-t'/\tau_A)dt'$$

$$= (\text{DC voltage gain}) \times V_m g(t) \quad . \qquad (18)$$

For the case of common anodes with τ_2 = 150 nsec and V_m = 0.20 mV, Fig. 14b indicates an output pulse amplitude of about 46 mV from a 100X amplifier. A factor which has not been included in this result is the effect of the fraction of positive charge which is induced on neighboring anodes. In the common mode, this charge algebraically subtracts from the negative induced charge resulting in lower pulse amplitudes. If it is assumed that about half of the positive charge is induced on the anode plane, then the values indicated by Fig. 14b should be halved. The resulting value of 23 mV is in good agreement with the experimentally obtained value of 20 mV. Predicted and observed pulse shapes were also in good agreement.

The actual values chosen for the coupling circuit components depend to a large extent on application. For imaging systems employing delay line readout, pulse timing is of the utmost importance so the design criterion is to obtain large pulses for high signal-to-noise ratio and to minimize rise and fall-times for accurate triggering of electronic components. As in many design problems, these two requirements are not complementary and the final design must be a compromise. The component values used in the sample calculation were the experimental values; while the 20 mV pulse obtained from the interaction of a ^{55}Fe x-ray was below the experimental detection threshold, the pulse amplitudes produced by the more ionizing $^{10}B(n,\alpha)$ α-particles saturated the amplifiers at similar MWPC electron gain.

Equation 13 applies equally well to capacitive cathode signal coupling. In this case, the HV supply and limiting resistor is replaced by a grounding resistor whose value is high enough (typically 100-200 kΩ) that it can be ignored. If the cathode wire spacing and wire radius are similar to the anode spacing and radius, then C_g should be of the same order. Of course, V_m will be reduced by some factor depending on the chamber geometry as discussed in the previous section and in Appendix A.

C. Coordinate Readout Methods

To localize an ionizing event in the MWPC, some method of pulse detection must be employed which can associate the pulse with a spatial position in the chamber. The most straightforward way to determine the coordinate perpendicular to the anodes is to use an amplifier on every anode and record pulses from each amplifier. Since negative pulses are

induced only on the avalanche anode and positive pulses are induced on all other anodes, it is relatively easy to determine on which anode the avalanche occurred (note that an inclined track whose projection on the anode plane spans more than one wire spacing will result in avalanches on more than one wire). By pancaking two chambers with their anodes mutually perpendicular, both coordinates can be obtained. While this method is satisfactory for the detection of minimum ionizing radiation, it is useless for the detection of low energy x-rays or any other radiation that would not deposit energy in both chambers. In general, it is necessary to obtain both coordinates from the same chamber.

To determine the event position along the length of the anode wire, anode current division has been used. For this method the anodes are made of a resistive material (20-μm-diameter tungsten wire has a resistance of 180 Ω/m so the amount of current flowing to each end of the wire is a function of the avalanche position. Denoting left and right by L and R, the distances of the avalanche from the ends of a wire of length ℓ are

$$X_L = \frac{\ell i_R}{i_L - i_R} \quad \text{and} \quad X_R = \frac{\ell i_L}{i_L - i_R} \quad .$$

A low impedance amplifier is used at each end of the wire and the accuracy of the localization is extremely sensitive to amplifier gain variations. Foeth, Hammerstrom and Rubbia report spatial resolutions on the order of 3 mm over a distance of 11 cm.[47]

Other methods have been developed which employ the positive induced cathode pulses. However, the cathode readout is more difficult for several reasons. The induced cathode charge distribution can extend

over distances of several cm (depending on chamber geometry) and all cathode pulses are positive. In addition, cathode pulse amplitudes tend to be much smaller than anode pulses due to the smaller induced charge. Fischer and Plch[45] used cathode strips of such a width (5 cm) that one strip received nearly the total induced charge when the avalanche was centered over the strip. By adjusting the threshold of their recording electronics, they were able to limit sensitivity to one strip per event with only moderate losses in efficiency. However, the spatial resolution obtainable with such wide strips is not sufficient for many applications. Charpak[48] has extended this idea by grouping cathode wires (1 mm spacing) into alternate strips of four. Using a fast divider to obtain the ratio of pulse heights on two adjacent strips, he has achieved position accuracies of 0.15 to 0.20 mm.

Several methods have been developed which simplify the coordinate readout considerably by transforming position differences to time differences. The transformation is accomplished through the use of passive electronics only, so a minimum of active signal processing is necessary to complete the readout. Borkowski and Kopp accomplish the position-to-time conversion by using a resistive material (Nichrome or quartz fiber) for the cathode wires. This distributed resistance, in combination with stray capacitance, forms a distributed RC line. With proper RC terminations at each end of the continuous cathode winding, position information is obtained from the pulse rise-time. Using this readout scheme in a 20 by 20 cm sensitive area chamber, Borkowski and Kopp[49] have achieved a 1 mm spatial resolution for x-rays in the 5 to 30 keV energy range. They report a position-to-time conversion ratio of about 5 nsec/mm.

Another method of accomplishing position-to-time conversion is through the use of distributed LC electromagnetic delay lines. Early work in this area by Perez-Mendez et al.[50] with small commercial delay lines showed the scheme to be workable, and spatial resolutions of 0.15 mm were obtained. For use with an MWPC, the wires are brought out of the chamber and coupled (capacitively, inductively, or directly) to consecutive points on the delay line. The arrival time of the pulse at one end of the line can be compared with the prompt anode pulse or with the arrival time at the other end of the line.

Perez-Mendez has developed a design especially well-suited for the MWPC[51] with a rectangular cross section which provides a relatively large flat surface for capacitive signal coupling. The wires of the MWPC are soldered to conducting strips etched on a PC board which, in turn, are coupled to the delay line by simple pressure contact. The position-to-time conversion ratio is adjustable through the parameters of distributed inductance and capacitance per unit length. Typical values which have been used to date lie in the 5-20 nsec/mm range. With the use of fast, low noise amplifiers and timing discriminators capable of 1 nsec time resolution, the fastest lines can be employed while maintaining spatial resolution in the fractional mm range.

The choice of readout system employed on the MWPC depends to a large extent on the application. Particle physics sometimes requires the capability for resolving multitack (simultaneous) events. In general, the amplifier-per-wire method with parallel readout is most suitable for this purpose. However, for most imaging applications, coincidences are

accidental and can be detected and rejected so that position-to-time readout systems which require four amplifiers at most offer a great reduction in cost and complexity. Neither the position-to-time readout method nor the amplifier-per-wire method fully exploits the extremely high rate capability of the MWPC. In the former case, the signal processing times are in the μsec range for chambers with practical dimensions (> 10 cm square) and in the latter case, data storage times are the limiting factor.

A distinct advantage of the delay line readout method is its inherent ability to interpolate between signal coupling points for the maximum pulse height. Signals are typically coupled to the line at 1 or 2 mm intervals (corresponding to 5 or 10 nsec of relative delay for a 5 nsec/mm position-to-time conversion ratio). Since the pulses are typically several hundred nsec wide, the addition in the delay line of coupled pulses from adjacent wires results in a single pulse whose centroid corresponds closely to the center of ionization of the detected event.

D. Electronic Signal Processing

A block diagram of an MWPC with delay line readout and its associated signal-processing electronics is shown in Fig. 15. Basic circuitry is drawn with solid lines and auxiliary systems are dotted. The time relationships between the pulses involved in the localization of an ionizing event are shown in Fig. 16. The sequence of events is as follows:

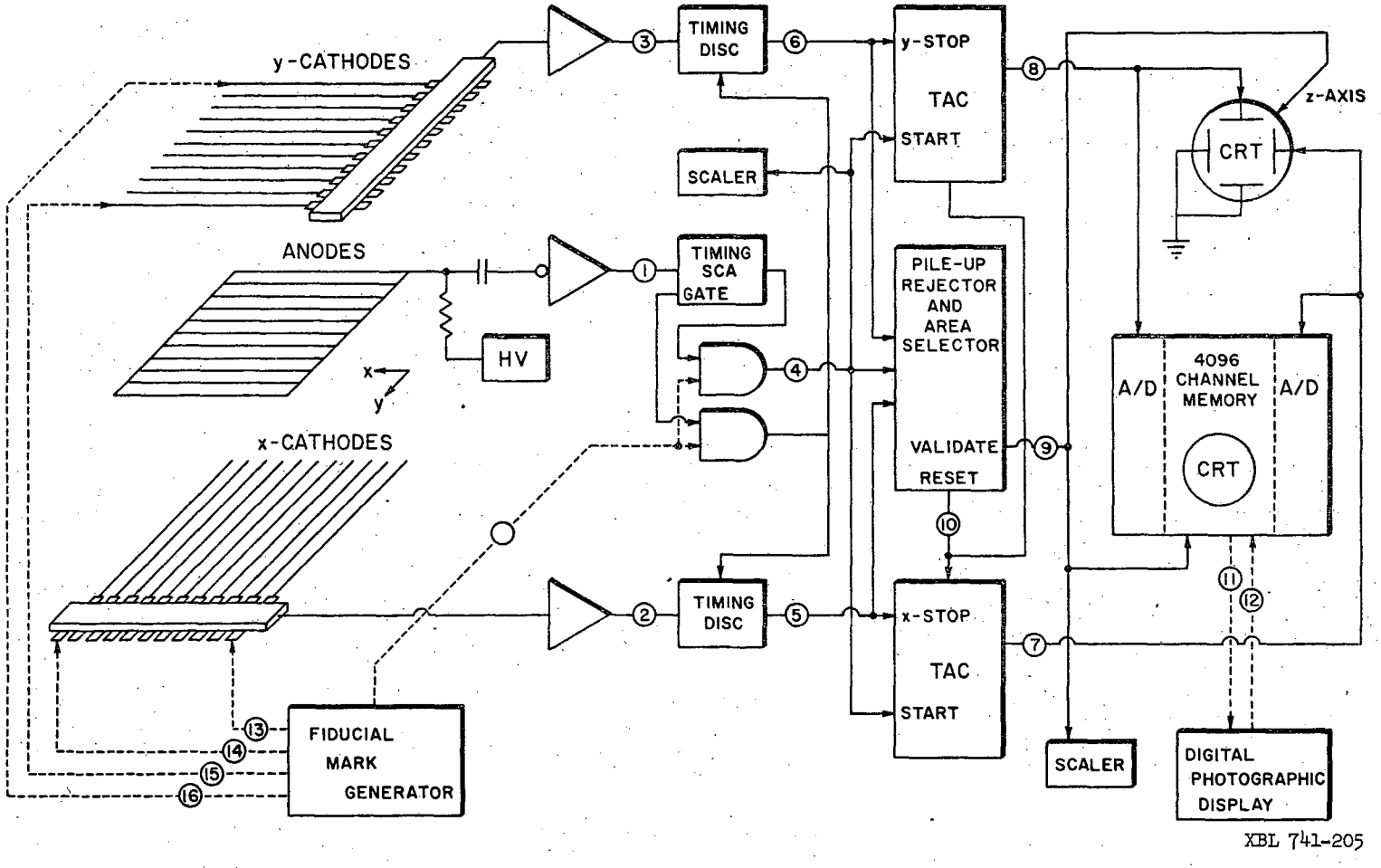

Fig. 15. Block diagram of MWPC pulse processing electronics. The dotted lines denote connections to auxiliary systems.

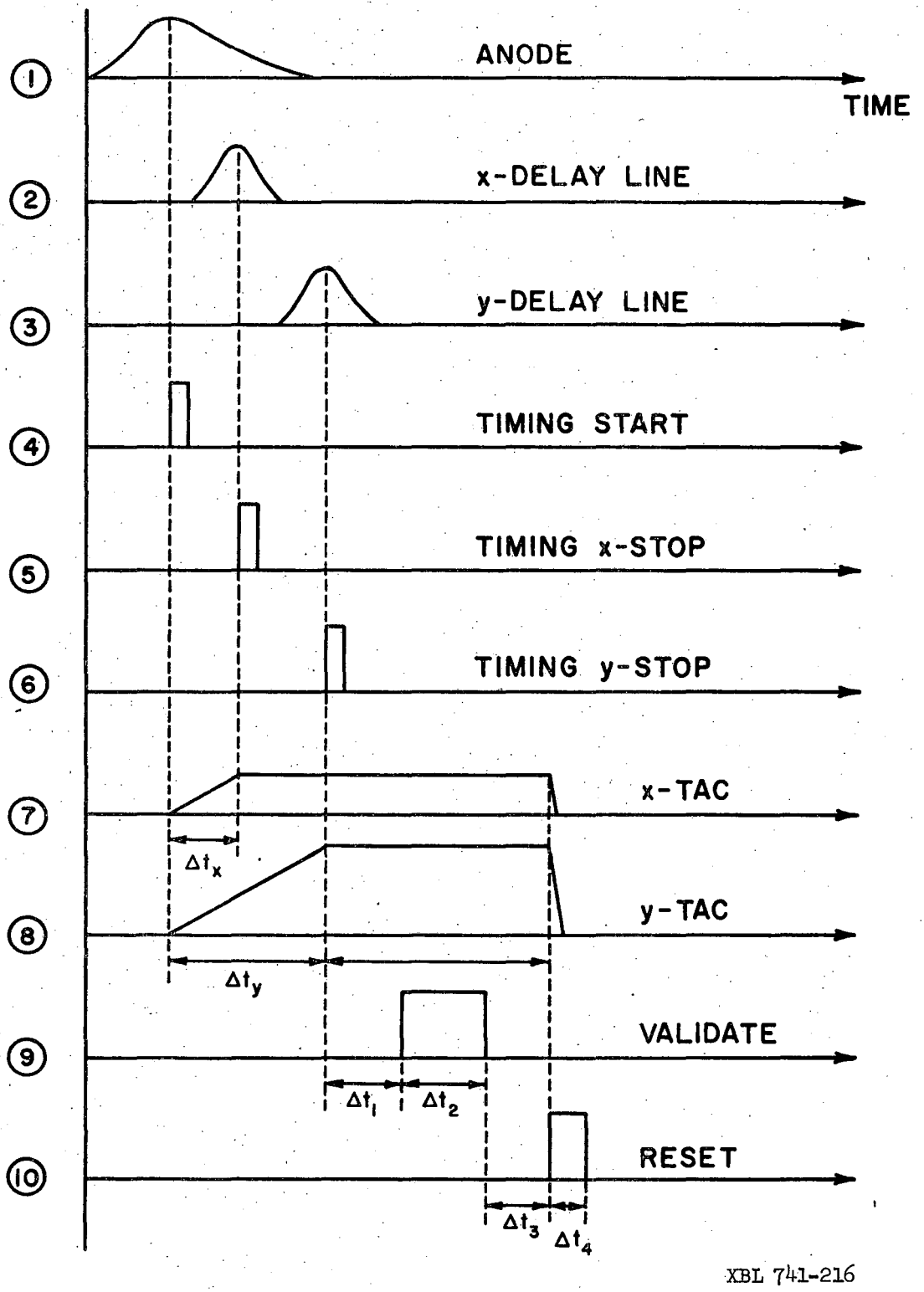

Fig. 16. Time relationships involved in MWPC pulse processing.

1. During ion drift, a negative pulse is induced on the anode plane and coupled into the amplifier. Simultaneous positive pulses are induced on wires of each cathode plane and coupled into the delay lines at points corresponding to the x-y coordinates of the avalanche.

2. The prompt anode pulse is single channel analyzed (SCA). If it lies in the acceptance window, it is zero-crossed and a fast timing pulse is generated. The outputs of the x and y timing discriminators are then gated on for a preset time (approximately equal to the total delay time of the delay lines). The timing pulse (START) initiates the ramp on both time-to-amplitude converters (TAC) and simultaneously disables their inputs so they cannot be restarted.

3. In this example, the pulse from the x delay line arrives first. It is zero-crossed and the timing pulse (x-STOP) terminates the ramp on the x-TAC. The voltage at the TAC output is now proportional to the x-coordinate of the avalanche.

4. The y delay line pulse arrives and is zero/crossed. The resulting timing pulse (y-STOP) terminates the ramp on the y-TAC.

5. The arrival of the later STOP pulse is detected by the PILE-UP REJECTOR and the preset time sequence, Δt_1 through Δt_4, is initiated. For CRT display, Δt_1 is the time required for the beam deflection to stabilize; for PHA storage it is set equal to zero. The validate pulse, generated during Δt_2, either intensifies the z-axis of the CRT to image the event or enables the PHA for storage. Δt_3 is the time allowed for the z-axis of the CRT to deintensify before the beam is returned to the origin. During Δt_4, a reset pulse is generated which discharges the TAC's and enables their inputs. If a second timing start

appears before the later stop, the validate circuit is disabled and the TAC's are reset after the delay lines have cleared.

An additional feature built into the PILE-UP REJECTOR was an area selector. It limits the system sensitivity to any rectangular area in the chamber by inhibiting the validate pulse for events which occur outside the rectangle. The rectangle is defined by comparing the x and y time delays (Δt_x and Δt_y) with variable delay, variable width gate pulses which are triggered by the timing start (Fig. 17a). If $\Delta t_{x1} \leqslant \Delta t_x \leqslant \Delta t_{x1} + \Delta t_{x2}$ and $\Delta t_{y1} \leqslant \Delta t_y \leqslant \Delta t_{y1} + \Delta t_{y2}$, the event is validated. This feature was particularly useful for measuring local detection efficiency and for making quantitative attenuation measurements of samples that did not completely cover the chamber.

A fiducial mark generator was designed which supplies a timing start directly to the TAC's and a set of shaped (to simulate MWPC pulses), synchronized pulses to the extreme outside wires of each cathode plane (Fig. 17b). Pulse processing results in a set of x-y TAC output pulses with a validate which correspond to the four corner points of the sensitive chamber area. These simulated corner events proved to be an invaluable aide for system alignment.

For on-line photographic display of the memory contents, a digital photographic display unit was designed and interfaced to the 4096 channel memory. It is basically a six-bit binary counter coupled to a six-bit D/A converter. The counter is triggered by a signal from the memory unit which occurs at the beginning of a memory scan cycle, and the D/A output is fed back to the contour level control (Fig. 17c). By recording the memory-unit CRT image on Polaroid film during 64 successive

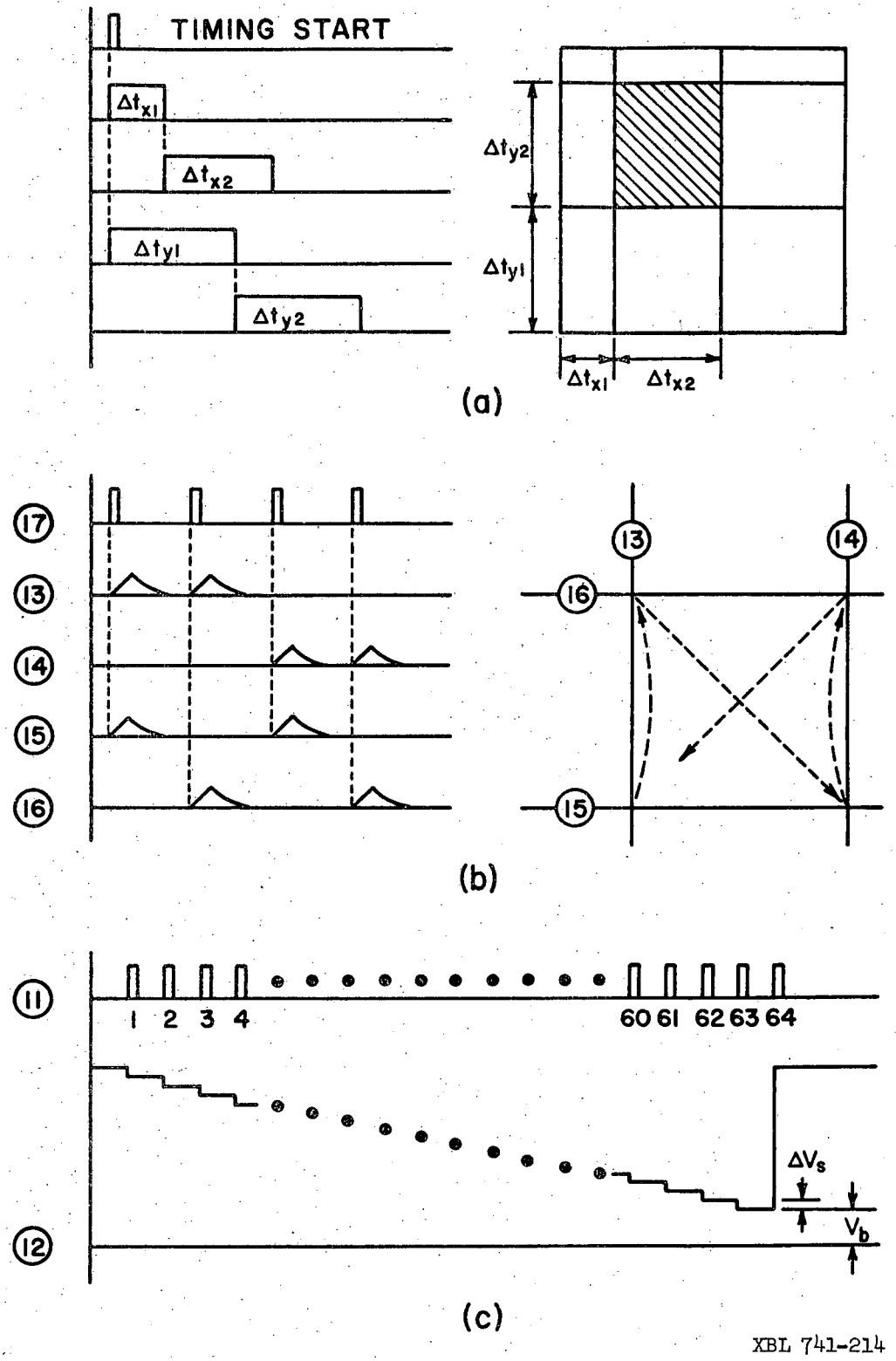

Fig. 17. Principles of operation of the (a) area selector, (b) the fiducial mark generator, and (c) the digital photographic display unit.

core scans, the numerical contents of the memory are converted to a 64 gray-shade photograph with the lighter gray shades corresponding to larger numbers of stored events. Variable gain (ΔV_s) and bias (V_b) were provided so small numerical differences could be expanded over the full 64 shade gray scale.

Aside from simple background subtraction (using the subtract mode on memory unit) the data were not accessible for arithmetic manipulation. For quantitative measurements and computer image processing, the memory contents were punched onto paper tape and converted to IBM cards so they could be analyzed off-line on a CDC 7600.

The advantage of collecting Polaroid film images from the CRT as the events are processed is the continuous spatial resolution which is obtained by avoiding the digitization. Of course, for sufficiently large memory, this is not a problem.

E. Neutron Sensitization of MWPC

1. Boron Layer for Thermal and Epithermal Energies

A thermal neutron is even less likely to interact in a thin layer of counter gas than in a photographic film. So in order to detect thermal neutrons in the MWPC with reasonable efficiency, it is necessary to employ a conversion reaction which occurs with high probability and whose reaction products are capable of causing significant ionization in the gas volume of the chamber. Candidate materials are the same ones used to enhance the photographic effect of thermal neutrons (Table II), but the final choice is subject to slightly different criteria.

Gadolinium has proven to be one of the best photographic converters due to the short range, 70 keV conversion electron which follows neutron capture. However, when a thick ($\approx$ 1 cm) detecting gas volume is substituted for the photographic detecting surface (fast emulsion coatings are typically in the 25 μm range) the residual range of the radiation in the detector must also be considered. For instance, while the range of a 70 keV electron is only about 50 μm in a film emulsion,[52] it is over 3 cm in argon at STP. Thus, ionization due to the Gd conversion electron would be distributed as far as 3 cm from the point of neutron interaction. For other materials listed in Table II which emit more energetic β-particles, the ionization extends even farther from the conversion point. Pressurization of the MWPC with a higher-Z gas such as xenon has been effectively employed for x-ray imaging in the 50-100 keV region and could also be applied to the case of neutron imaging. However, the use of neutron conversion reactions which result in the emission of low-energy α-particles offer several distinct advantages over the (n,β) converters.

The higher specific ionization provided by α-particles makes them most suitable for MWPC imaging applications. Not only are the ranges shorter but the total energy depositions are much higher. In a proportional system, the large energy deposition makes the α-particle easily distinguishable from less ionizing particles so that pulse height discrimination can be used to obtain immunity from non-neutron radiations. The (n,α) converting material can be introduced into the MWPC either as solid layers located in the outer cathode regions or homogeneously incorporated into the filling gas as in the standard BF_3 neutron counter.

For the work reported here, solid converting layers of 92% enriched ^{10}B were used. This allowed more latitude in the choice of filling gas and also provided a geometric focusing effect inherent in solid layer converters.

Figure 18a shows the physical location of the converting surface with respect to the active volume of the MWPC. The range of the 1.5 MeV α-particle resulting from neutron-capture by ^{10}B is about 4 μm in boron (R_B) and about 1 cm in argon (at STP), so the converting layer thickness is shown greatly exaggerated for illustrative purposes. Neutron conversion is shown occurring at two different depths in the converting layer with the corresponding loci of residual range track end-points in the gas. The α-particles are emitted isotropically from the conversion point and beyond a critical angle, $\theta = \cos^{-1}(d/R_B)$, they are stopped entirely in the converting layer. Thus, as the conversion depth increases, the α-particles are "focused" into smaller solid angles of emission about the converter normal.

When an α-particle does emerge into the gas volume, the electrons from its track are drifted along field lines toward the anode wires so that its effective range, from the spatial localization standpoint, is the length of the track's projection on the anode plane. In the event that the effective track length spans more than one anode wire spacing, avalanches will be initiated on several of the anode wires and the total length of the avalanches along the anodes will be equal to the length of the effective track component in the anode direction. The delay lines' ability to interpolate for pulse centroids results in the α-particle being localized at the center of ionization of the track, or approximately at

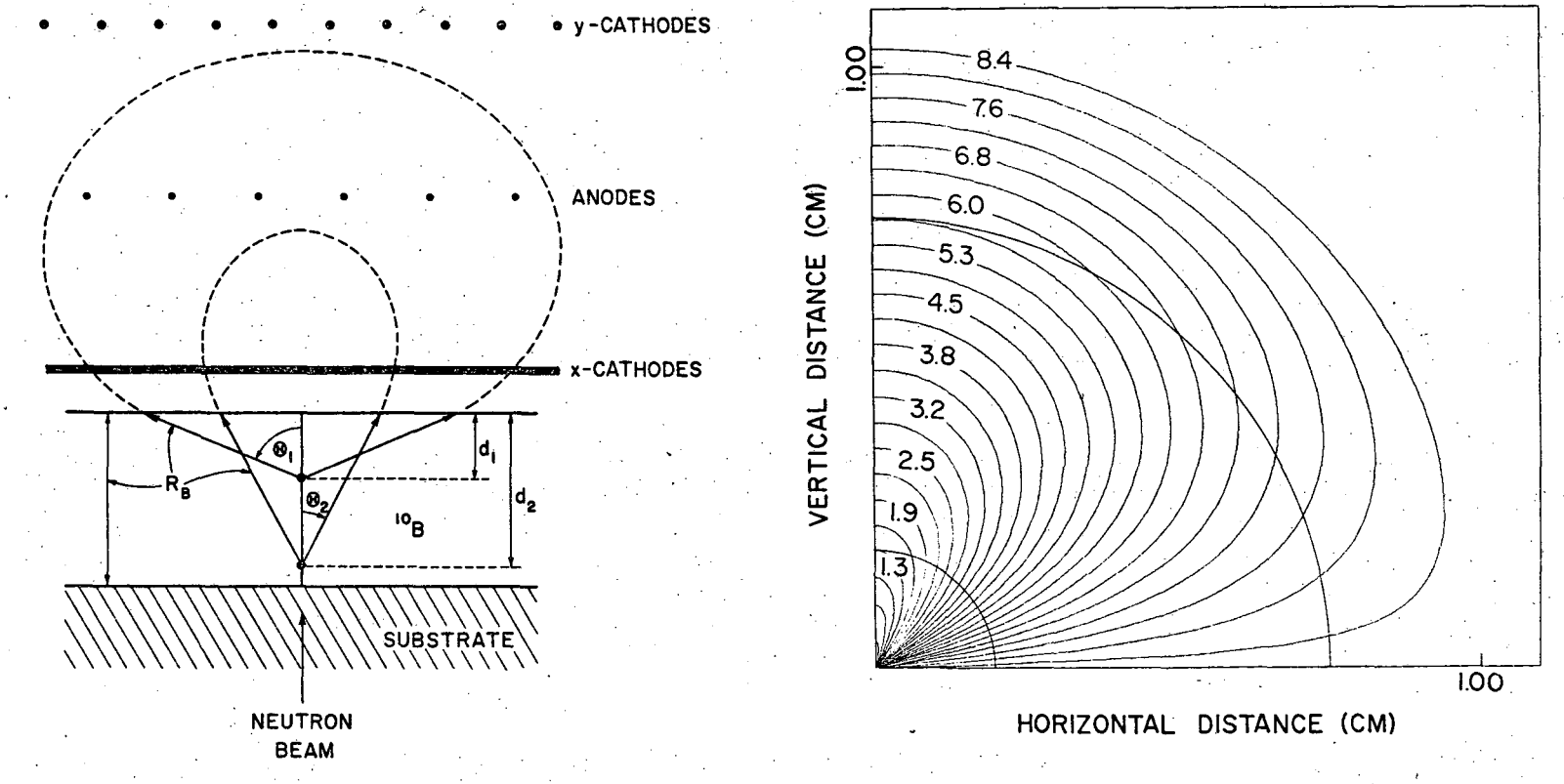

XBL 742-297

Fig. 18. (a) Geometry of the (n,α) conversion process. (b) Family of residual range curves for an optimum thickness ^{10}B converting layer.

the track midpoint. Of course, when only one anode sustains an avalanche, the α-particle must be localized at the anode position.

Figure 18b shows the entire family of residual range curves for a 4 μm thick boron converting layer. These curves were generated by dividing the converting layer into 25 equal thickness zones and then considering α-emission to be from the center of each zone. The geometry here is the same as in Fig. 18a; the neutron trajectory coincides with the ordinate and the abscissa lies in the plane of the converting layer. Due to the extremely short range of the α-particle in boron, α-emission appears to be from the origin. The numbers which appear on alternate curves are the percent of total alpha yield arising from the corresponding zone, and the radii of the two concentric circular segments are equal to the ranges of a 0.1 and a 1.0 MeV α-particle. Since shorter residual ranges result in smaller energy depositions, such circular segments correspond to energy thresholds that can be set on the SCA. The α-particles which then contribute to image formation are those lying on portions of range curves included between the segments. Thus, pulse height discrimination can be used to enhance the focusing effect by selecting the shorter range α-particles which deposit their energy close to the conversion point. Improving the spatial resolution in this manner, however, results in lower neutron detection efficiency.

Several other qualitative features of converting layer performance can be inferred from Fig. 18b. The effect of chamber thickness is to horizontally flatten loci where they intersect the far side of the chamber. For converting layers which are less than an α-range thick, the inner loci would be missing, and if the converting layer is coated

with a thin layer of non-converting material such as aluminum, outer loci would be missing. Also, since a 4 μm thickness of ^{10}B is only about 20% absorbing to thermal neutrons, the conversion process is essentially identical for neutrons which are incident through the chamber volume. Thus, addition of a second converting layer at a symmetric position on the other side of the chamber will double the α-particle yield per neutron.

The (n,α) reaction in ^{10}B can be used for neutron conversion into the epithermal range, but at reduced efficiency due to the lower epithermal cross sections. In the MeV region, boron is not a very useful converting material, but now the neutron energy is high enough to employ a slightly different approach.

2. Polyethylene Layer for Fast Neutrons

By replacing the boron converting layer with a layer of hydrogenous material (polyethylene), the incident neutron energy can be transferred to hydrogen nuclei through the n-p scattering cross section (10 to 1 barns between 1 and 10 MeV). Since n-p scattering is approximately isotropic in the CM system, recoil protons are ejected from the converter only in the forward direction, so only one converting layer can be effective in yielding protons to the active chamber volume. Locus plots of proton track endpoints are shown in Figs. 19a and 19b for incident neutron energies of 1.0 and 4.0 MeV. In these figures, the radii of the two reference circles are equal to the ranges of a 0.2 and a 0.7 MeV proton in argon. The previous discussion regarding localization of

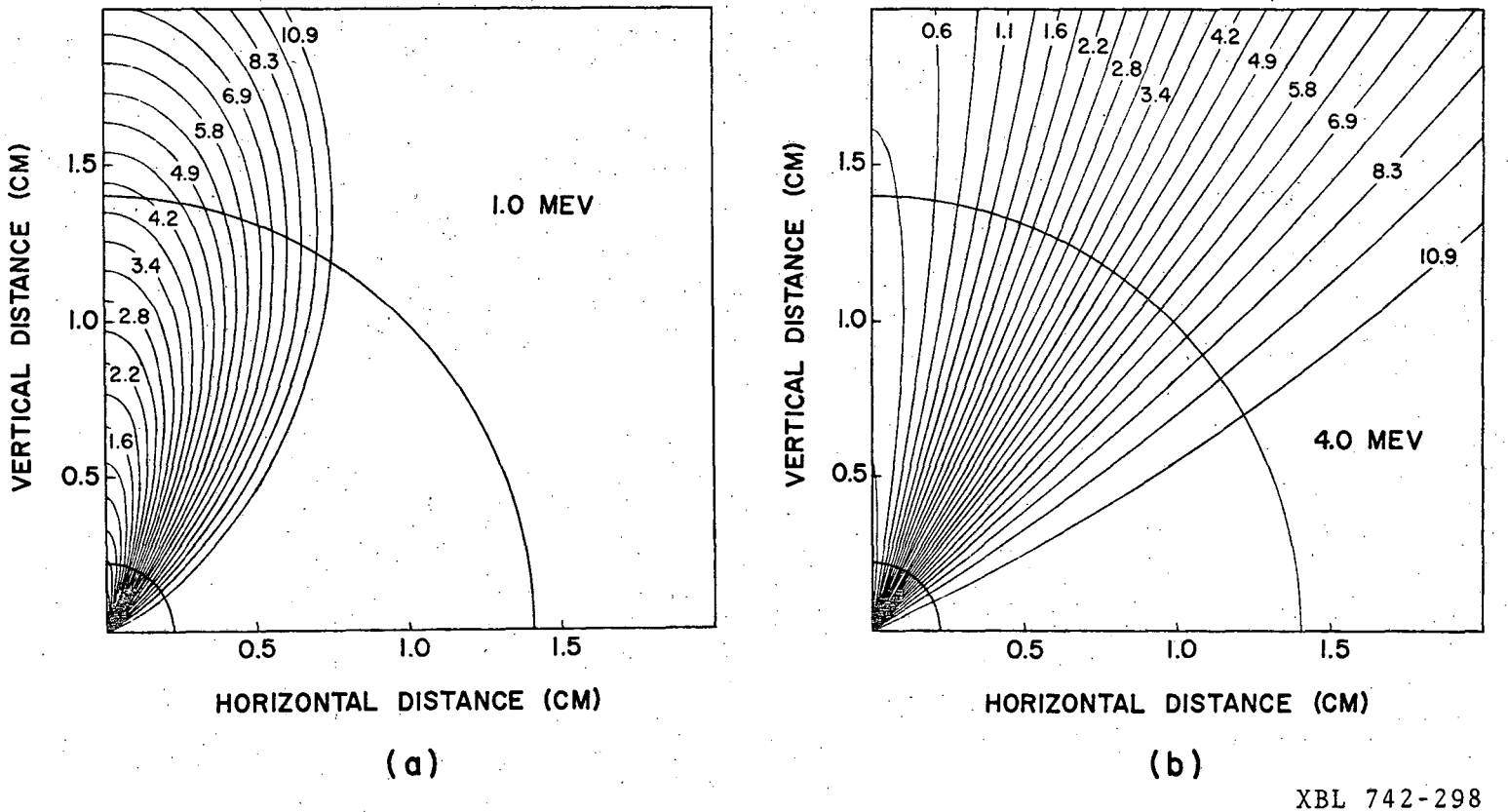

XBL 742-298

Fig. 19. Residual range locus plots for recoil protons ejected from a CH_2 converter for (a) 1 MeV neutrons and (b) 4 MeV neutrons.

α-particles from a boron converter also applies to localization of the recoil protons. The principal difference between the two conversion processes is that the initial recoil proton energy is a function both of incident neutron energy and of scattering angle, whereas the initial α-particle energy is a constant depending only on the Q-value of the exothermic (n,α) reaction.

The forward peaked nature of the recoil proton distribution is evident in Fig. 19a and comparison with Fig. 19b shows that the proton ranges increase rapidly with increasing neutron energy. Fortunately the finite thickness of a practical chamber effectively terminates the tracks so that most protons are not localized more than half a chamber thickness away from their point of origin.

IV. HARDWARE AND CONSTRUCTION

A. Prototype Chamber Design

The prototype chamber (Fig. 20) was originally built as an x-ray imaging chamber but its construction permitted easy adaptation for neutron imaging. It consisted basically of three electrical planes with an active area of 4.0 by 4.5 cm. The top plane was made up of 23 125-μm-diameter gold-coated molybdenum wires spaced two mm apart. The center plane also contained 23 wires spaced two mm apart. The center 17 wires were of 20-μm-diameter gold-coated tungsten and the outside three wires on either side of the chamber were graduated in diameter with the extreme outside wires having a diameter of 250 μm. The gradual increase in wire diameter toward the edges of the plane lowers the electric field at these wire surfaces. This counteracts the effect of the edge discontinuity which would result in higher fields on the outside wires. The bottom plane was a solid aluminum plate with a 0.70 mg/cm^2 coating of natural boron and a 150 Å overcoating of aluminum. The two support frames were made of Nema G-10 fiberglass epoxy and a third frame of the same material covered with thin mylar served as a window. The wires of each plane were fastened at both ends by soldering to printed circuit boards.

The delay line coupling strip boards were separate from the chamber. Wires were used to connect each wire of a plane to a coupling strip. Since the delay lines were 10 inches long and the active area of the chamber was less than two inches wide, it was possible to obtain coordinate fanout so that 1 mm at the chamber corresponded to about 4 mm at the delay line. This effectively increases the spatial resolution of the electronic readout system.

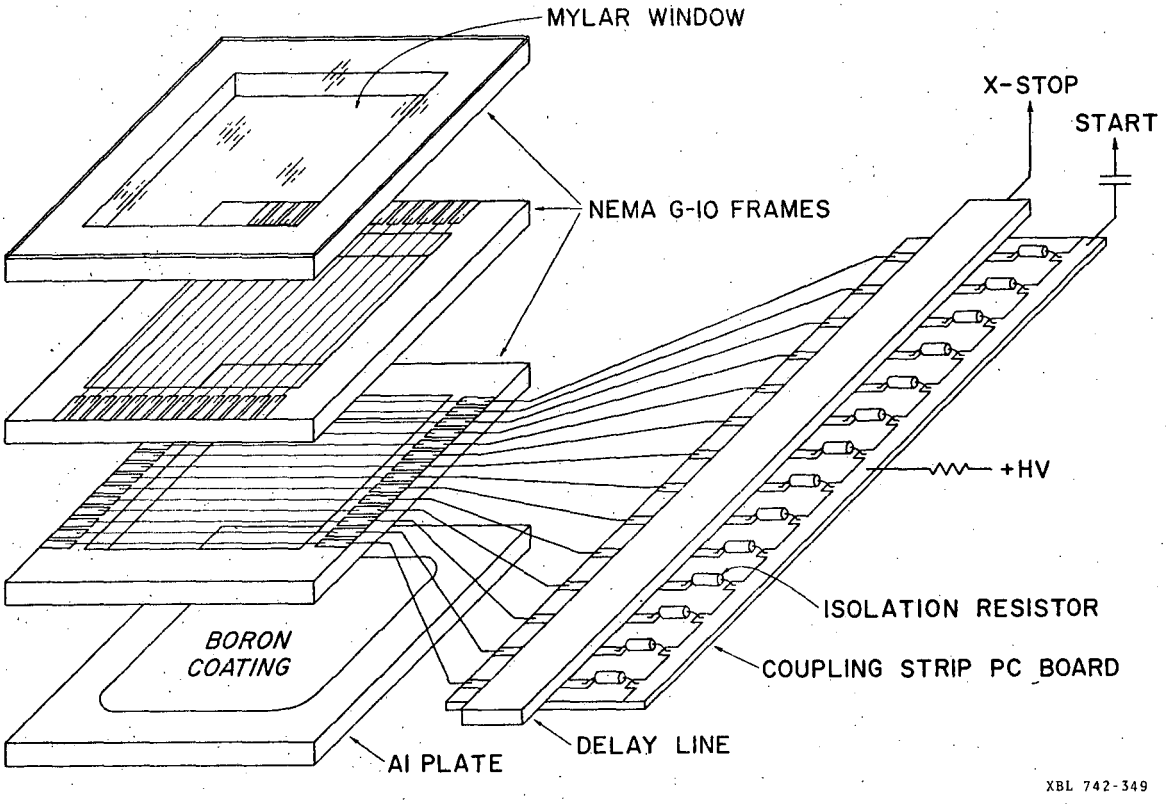

Fig. 20. Exploded diagram of the prototype chamber. Coupling of cathode signals to the y-coordinate delay line was accomplished in the same manner as shown for the anode signals.

B. 10 × 10 Inch Chamber Design

While data was being collected with the prototype chamber, construction was begun on a larger chamber. An active area of 10 × 10" was chosen for the new chamber to utilize the available beam area more efficiently and to provide a radiographic surface large enough to accommodate a wider variety of test objects. This chamber was designed for easy interchange and adjustment of the converting surfaces and differs from the prototype chamber not only in size but also in the addition of a third wire plane. The additional wire plane, rather than the converter plate, serves as the second cathode plane. By arranging the wires of the second cathode plane perpendicular to the wires of the first, x-y coordinate information can be read in a symmetrical manner from the cathodes which allows the anodes to be bussed together to supply the start signal. Also, when desired, symmetrical drift spaces can be established in both outer cathode volumes.

As in the case of the smaller prototype chamber, the dielectric frames which separate the wire planes are made of Nema G-10 glass epoxy. In all there are four Nema G-10 frames. The two central frames are each 3 mm thick and provide the actual interplanar spacing while the outer frames are each 10 mm thick and provide structural rigidity during assembly. The outside frames also serve as mounting surfaces for the coupling strip PC boards and the converter plates. The four-frame subassembly is sandwiched between two 1/4" thick steel plates and four corner through bolts clamp the unit together. All Nema G-10 and steel plate surfaces were surface ground to insure the uniformity of thickness that is necessary for maintaining uniform plane spacings, and an elastic

silicone adhesive was used to make the interplanar bonds. With the addition of front and back converter plates and side plates, almost complete electrical isolation is obtained for the wire planes and delay lines. This is important since the delay lines, in particular, tend to be susceptible to the pickup of high frequency noise. Figure 21 shows the general layout of the chamber and the relationship of its parts.

The 10 mm thick Nema G-10 frames were first sawed and then milled to shape. Reliefs were milled into these frames to accept the coupling strip PC boards which were epoxied into place. Additional reliefs were milled between the PC board reliefs and the chamber cutout to accept a bead of epoxy used to fasten the wires in place temporarily while they were being soldered to the PC boards. After similar preparation of the 3 mm thick frames, a 1 mm wide by 1 mm deep slot was milled into the perimeter of the chamber cutout of each frame. These slots are intended not only to decrease surface leakage currents by extending the leakage path, but also to minimize the perturbing effect of the edge with respect to edge-sparking.[53] After all machining was completed and the circuit boards had been epoxied in their reliefs, all machined edges which would be exposed to the gas volume were coated with epoxy and then sanded smooth.

The wire planes were wound on an automatic winding machine which accurately spaces and pretensions the wires. To cover a 10" wide active area, a wire array is wound with a width of at least 11". When the winding is complete, the frame is positioned beneath the wires and elevated until the frame and wires are just touching. Epoxy is then

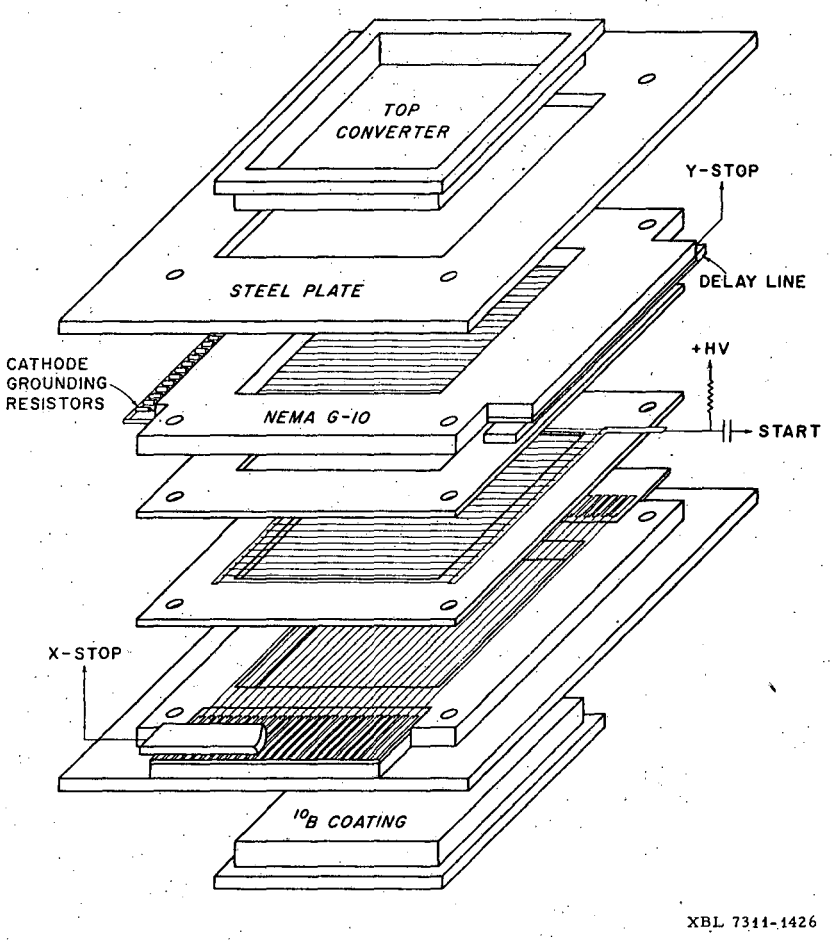

Fig. 21. Exploded diagram of the 10 × 10 inch neutron-sensitive MWPC. Part of the x-coordinate delay line has been omitted to show the signal coupling strips.

C. Neutron Converters

Aluminum holders were prepared to carry the neutron converting layers. Their purpose was not only to provide a flat base for the sensitive layer but also to provide a reference surface for accurate positioning of the layers in the chamber. The actual substrate was a 10 × 10 inch square of 0.063-inch-thick flat aluminum sheet-stock. A stiffening frame was machined from solid aluminum stock and the two pieces were joined together either with epoxy or by electron-beam welding. Heliarc welding was also tried but the larger amount of heat warped the final assembly. A flat gasket surface was machined onto the frame so the holder could be sealed to the chamber with a square, neoprene gasket. The distance between the converting layer and the cathode was adjusted by adding PVC shims to the gasket.

Boron converter coatings were deposited in a vacuum using an electron beam source heater. One natural boron coating and two 92% enriched ^{10}B coatings were deposited in this manner, and in each case an attempt was made to overcoat the boron with a thin layer of aluminum (1000-2000 Å). However, within several days following completion of the deposition, the overcoat peeled from both enriched converters carrying away a significant fraction of the boron coating. The reason for the peeling is not clearly understood but is possibly due to the adsorption of water vapor on the partial coating which occurred when the vacuum system was let up to atmosphere for recharging the source crucible.[54] The final coating thicknesses obtained for the enriched converters were therefore less than the desired value of 1 mg/cm^2 (about 4 μm at theoretical density).

poured into the relief grooves provided for it, and its high viscosity allows it to crown above the surface of the frame and embrace the wires. After the epoxy sets, the wires are soldered to the PC boards at both ends. Although there is a strong tendency for the wires to be deflected to one side or the other during soldering, the epoxy maintains the wire spacing over the active area. Of the extra wires extending past the active area, about five are retained on each side and the rest are cut out. These wires provide an effective solution to the fringe field problem by maintaining the electric field (and hence the proportional multiplication) reasonably constant right up to the edge of the active area. Both cathode planes were wound with 37 μm gold-coated molybdenum wire tensioned at 100 grams with a spacing of 1 mm. The cathodes were terminated in pairs through a 200 kΩ resistor to a common bus. Originally the anode plane was also wound at a spacing of 1 mm using 12.5 μm gold-coated tungsten wire tensioned at 25 grams. However, the proportional gain which was obtained at the onset of spark breakdown was less than desired, so the anode plane was rewound at a spacing of 1.5 mm. After reassembly the breakdown voltage was found to be almost the same as before, but as indicated by Eq. (9) in Sec. III the increased electric field strength around the wires provided the additional necessary gain.

The delay lines were mounted on the coupling strips with 12.5 μm mylar in between for insulation. Foam rubber strips were compressed into the space between the delay line and the steel plate to hold the delay line firmly against the coupling strips for good capacitive coupling of the cathode signals. Under good coupling conditions, signal attenuation in the delay lines is about 3 dB/ft. All gas and electrical connections from the chamber were terminated at couplers fastened to the sideplates.

The purpose of the aluminum overcoat was to provide an electrically conducting coating over the relatively insulating boron layer; early work with the prototype chamber had indicated that there might be problems associated with surface charge buildup on uncoated converters. However, in the large chamber, the converting surface does not function as a cathode and no problems were encountered with the uncoated converters.

In a double converter system, the tolerances can be relaxed in fabricating the downstream converter. While the thickness of the upstream layer should be uniform and no thicker than an α-particle range (so the neutron flux reaching the second converter is not unnecessarily attenuated), neither total attenuation nor uniformity are considerations for the downstream layer. At a considerable savings in expense, a simple and equally satisfactory converting layer was made by covering an entire aluminum substrate with double-sided, pressure-sensitive tape and then dusting 92% enriched ^{10}B powder onto the resulting adhesive surface. The thickness of the boron layer obtained in this manner varied between 3 and 4 mg/cm^2.

A sheet of 0.063-inch-thick, 0.92 g/cm^3 polyethylene was used as the fast neutron converter. It was attached to the aluminum holder with double-sided, pressure-sensitive tape.

D. Description of Electronic Equipment

1. Delay Lines

The rectangular cross section delay lines used for coordinate readout function identically to the more common cylindrical delay lines encountered in delayed sweep oscilloscopes or linear pulse amplifiers.

Figure 22a shows the basic construction of the line. It consists of a single layer helical coil wound over a plastic core to which conducting strips have been attached. The line is characterized by an inductance per unit length, L_o, due to the coil and a capacitance per unit length, C_o, due to capacitive coupling between the coil and the grounded conducting strips.

Consideration of Fig. 22b shows that

$$i_c = I(z) - I(z + dz) = I - (I + \frac{\partial I}{\partial z} dz) = - \frac{\partial I}{\partial z} dz = C_o dz \frac{\partial V}{\partial t} \qquad (19a)$$

and

$$v_L = V(z) - V(z + dz) = V - (V + \frac{\partial V}{\partial z} dz) = - \frac{\partial V}{\partial z} dz = L_o dz \frac{\partial I}{\partial t} \quad . \qquad (19b)$$

Cancelling the differential length, dz, from both sides of Eqs. (19a) and (19b) yields the ideal transmission line equations,

$$\frac{\partial I}{\partial z} = -C_o \frac{\partial V}{\partial t} \qquad (20a)$$

and

$$\frac{\partial V}{\partial z} = -L_o \frac{\partial I}{\partial t} \quad . \qquad (20b)$$

If Eq. (20a) is differentiated with respect to time and Eq. (20b) with respect to distance, the second order partial, $\frac{\partial^2 I}{\partial z \partial t}$, can be eliminated and the result is

$$\frac{\partial^2 V}{\partial z^2} = L_o C_o \frac{\partial^2 V}{\partial t^2} \quad . \qquad (21)$$

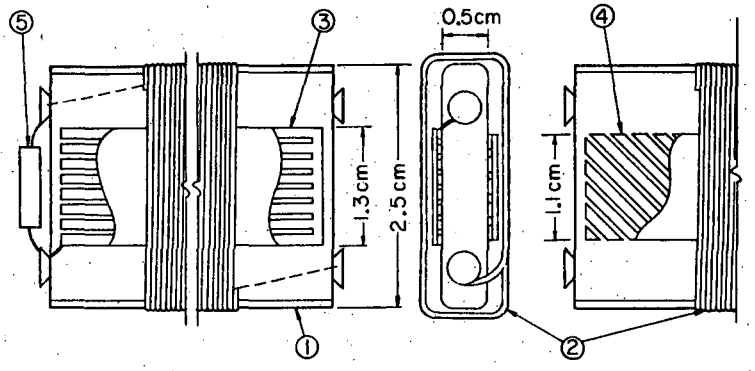

1 Plastic Core
2 Winding (#38 wire, 8 turns/mm)
3 Ground Strips (6.3 strips/cm of 12 μm Al on 25 μm Mylar. Strip width = 1.2 mm, gap width = 0.4 mm)
4 Compensating Strips (Same material as ground strips)
5 Terminating Resistor

(a)

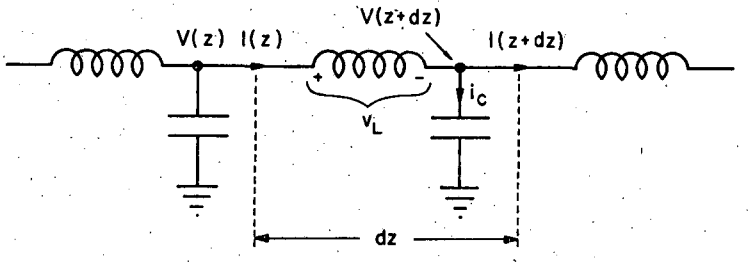

(b)

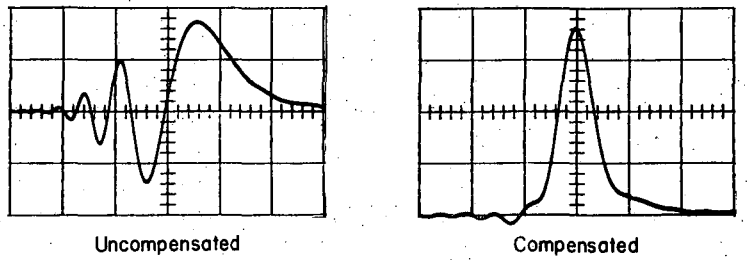

(c)

XBL 747-296

Fig. 22. Delay line characteristics. (a) MWPC delay line construction, (b) circuit model of ideal transmission line, (c) output waveforms for uncompensated and compensated delay lines.

By direct substitution it can be shown that any function of the form, $V(z,t) = V(t \pm \frac{z}{v_o})$, is a solution of Eq. (21) where $v_o = 1/\sqrt{L_o C_o}$. Thus the ideal transmission line can propagate a waveform of any shape in either direction with no distortion, for if an observer were to travel down the line starting at $(t,z) = (t_o, z_o)$ with the phase velocity, v_o, such that $z = z_o \pm v_o(t - t_o)$, he would see no change in the voltage. An equation similar to Eq. (21) can be derived for the current so the solutions for the current are also of the form $I(z,t) = I(t \pm \frac{z}{v_o})$. Letting $x = t \pm \frac{z}{v_o}$ and substituting the solutions for V and I into Eq. (20b) yields

$$-\frac{1}{v_o}\frac{dV}{dx} = -L_o \frac{dI}{dx} \rightarrow \frac{\frac{dV}{dx}}{\frac{dI}{dx}} = v_o L_o = \sqrt{\frac{L_o}{C_o}} \quad .$$

Integration with respect to x yields $\frac{V}{I} = \sqrt{\frac{L_o}{C_o}} = Z_o$, where constants of integration have been ignored since it is the AC characteristic impedance which is desired.

As might be expected, the performance of physical delay lines departs from that of the ideal transmission line. To some degree, all conductors (excepting superconductors) are resistive and dielectrics tend to be lossy. Both of these power loss mechanisms are frequency dependent (resistive skin effect) so that greater losses are incurred by the higher frequency components of a waveform resulting in amplitude distortion of the wave. While these losses cannot be eliminated, they can be minimized by proper choice of construction materials. Perez-Mendez reports values for attenuation on the order of 1 dB/μsec at 3 MHz[51,55] with the attenuation increasing rapidly beyond 5 MHz.

In addition to amplitude distortion, another distortion mechanism shows up when the wavelength of the excitation in the line becomes comparable to the cross sectional dimensions of the line. This phenomenon is known as phase distortion and is due to unequal phase velocities for different frequency components. The principal cause of phase distortion is the diminishing value of distributed inductance at higher frequencies (shorter wavelengths). This effect arises in extended inductors because as the wavelength shortens, individual turns of the coil are flux-linked to other turns in which the current can be as much as 180° out of phase. Reinforcement of the flux through mutual inductive coupling of consecutive turns is therefore diminished and the distributed inductance drops. A derivation due to Blewett and Rubel[56] shows that

$$L(\lambda) = 2L_o I_1(2\pi a/\lambda) K_1(2\pi a/\lambda) \tag{22}$$

where λ is the wavelength, a is the radius of a circular coil, I_1 and K_1 are modified Bessel functions of the first and second kinds respectively, and L_o is the low frequency value of the distributed inductance which was used in the derivation of the ideal case. For a rectangular line with a thickness, T, and a width, W, it is probably best to use a mean value for a obtained by equating cross sectional areas, i.e., $\pi a^2 = TW$.

Another cause of phase distortion is due to the capacitive coupling between turns of a close-wound coil. Although the magnitude of this capacity is constant, no coupling occurs at long wavelengths because adjacent turns experience approximately the same $\frac{dV}{dt}$. However when the wavelength becomes sufficiently short that $\frac{dV}{dt}$ varies significantly from

one turn to the next, capacitively coupled currents begin to flow between the turns. Lewis[57] has shown that the effect can be modeled as an increase in the distributed capacitance,

$$C(\nu) = \frac{C_o}{1 - \nu^2/\nu_o^2} \tag{23}$$

where ν is the frequency of the excitation and C_o is the low frequency value of the distributed capacitance. ν_o is the resonant frequency of a circuit consisting of the effective inductance of one turn in parallel with the capacitance between two adjacent turns.

In terms of the inductance and capacitance given by Eqs. (22) and (23), the phase velocity becomes

$$v = v_o \sqrt{\frac{1 - \nu^2/\nu_o^2}{2I_1(2\pi a/\lambda)K_1(2\pi a/\lambda)}} \tag{24}$$

Since λ is a function of v ($\lambda\nu = v$), Eq. (24) is not an explicit expression for v, but it can be stated that both the numerator and the denominator of the radical decrease with increasing frequency so that to a degree, the effects of decreasing inductance and increasing capacitance are self-compensating. In general, the inductance decreases faster than the capacitance increases resulting in higher phase velocities for higher frequencies.

Several methods are available for improving the phase compensation of the line.[50,58] The method employed for the lines used in this research was the floating patch technique which effectively provides an additional,

frequency dependent, shunt capacity to ground. The floating patches are the diagonal conducting strips shown in Fig. 22a. The term, floating, refers to the fact that the strips are not electrically connected to any other part of the delay line. Qualitatively, their function can be interpreted in the following manner.

For long wavelength excitations, the patches are capacitively coupled to turns all of which experience the same V(t). However, when the wavelength becomes short compared to the longitudinal extent of a strip, it is coupled to turns of all phases and it then acts as though it were grounded.* From the functional dependence of phase velocity on frequency and wavelength (Eq. (24)), it is clear that no simple technique can achieve perfect phase compensation so the strips are tailored to provide optimum compensation over a bandwidth which is wide enough to adequately reproduce the desired waveform. Compensation of a line beyond the frequency at which amplitude distortion becomes significant is a wasted effort anyway. Figure 22c shows the output response of a rectangular cross section delay line (with and without floating patch compensation) for a 50 nsec risetime step function input which was capacitively coupled to the line. This particular line had a characteristic impedance of 620 Ω and a compensated phase velocity of 20 cm/μsec.

All of the active signal processing electronics were specially designed for an MWPC imaging system. This includes the amplifiers, the timing SCA and timing discriminators, the pileup rejector and area selector, and the TAC's. In the following, a brief account of each

*For a complete discussion of floating patch phase compensation, see Ref. 59.

component will be given along with the performance characteristics of the system as a whole (see Appendix B for circuit schematics and logic diagrams).

2. Amplifiers

The amplifiers were built around the Fairchild μA733 IC voltage amplifier. The differential inputs of the μA733 provide for simple inversion of the negative anode signal and the output is fed to a discrete, two-transistor line-driver with 50 Ω capability. The feedback loop of the IC was adjusted to provide a voltage gain of about 100. The overall risetime of the amplifier is about 80 nsec and 20 mV input pulses could be linearly amplified with no noticeable distortion. RMS noise at the output with grounded input is about 2 to 3 mV and the total input capacity, including MWPC connections, is about 20 to 35 pF.

3. Timing SCA

The timing SCA and timing discriminators (identical to former except for SCA capability) are the most critical components in the system since the resolution ultimately depends on their ability to assign a definite time of occurrence to the output pulses from the MWPC. For the work described here, zero-cross (peak detecting) discriminators were used which are based on the principle that the occurrence-time of the peak is common to a family of pulses, regardless of their amplitude. Zero-cross discriminators are commonly used and consist basically of a signal differentiator, an amplifier, and a germanium tunnel diode detector. After differentiation and amplification of a positive input pulse, the

positive portion of the resulting bipolar current pulse is used to set the diode which is then reset as the positive-to-negative transition crosses zero (set and reset refer to positions on the tunnel diode characteristic curve to either side of the negative resistance region). By proper diode biasing, the leading edge of the voltage pulse which occurs on resetting the tunnel diode can be made to coincide closely with the peak of the input pulse.

While the principle of zero-cross detection is a sound one, several factors tend to make practical performance less than ideal; finite differentiation time-constants, finite amplifier gain in conjunction with a finite current differential to initiate set and reset, and amplifier noise, to name a few. However, the units which were used performed adequately with a maximum timing error (slew) of about 5 nsec over a dynamic range of 20 (50 to 1000 mV). Timing inaccuracies associated with amplifier noise (jitter) were largest near the 50 mV detection threshold (±2.5 nsec) but dropped below ±1 nsec for pulse amplitudes above 250 mV. The output of the discriminators is a fast NIM-level pulse (-700 mV; 2 nsec risetime) created by MECL-II components.

4. Pileup Rejector and Area Selector

The primary function of the pileup rejector is to detect and reject events which occur in a time interval which is short enough that stop-pulses from both events could be in the delay line simultaneously. It also serves as a cycle clock by keeping track of the arrival times of the timing pulses and then supplying appropriate control pulses. However, neither of these functions affects the spatial accuracy with which an

event is localized, so cheaper, TTL logic (10 to 20 nsec risetime) was used to generate the time gates and controls. TTL logic was also used in the area selector.

5. TAC's

The heart of the time-to-amplitude converter is a switched current source which linearly charges a 3900 pF silver-mica capacitor. The switching is controlled by MECL-II logic. A high input impedance amplifier (> 1 MΩ) is used to sense the voltage on the capacitor so as not to materially change the voltage during the display time.

6. Performance Characteristics

The timing accuracy of the assembled system is shown in Fig. 23. In (a), constant amplitude, 500 mV pulses from the fiducial mark generator were coupled into the delay lines and the resulting x-TAC output was collected in a PHA. Two 20.4 nsec lengths of cable were then added between the x-STOP timing discriminator and the x-TAC to produce the second and third peaks. The FWHM of the peaks is seen to be less than 2 channels = 1.3 nsec. This corresponds to a position accuracy of 0.2 mm for the delay line position-to-time conversion ratio of 6.8 nsec/mm. In (b), a continuous spectrum of random anode pulses (0 to 700 mV from interaction of Pu-Be source neutrons in the chamber at a rate of 10^4/sec) was teed into the START timing SCA and x-STOP timing discriminator. An 80 nsec length of cable was used to delay the pulses into the x-STOP timing discriminator to bias the x-TAC, and the SCA was set to accept pulses with amplitudes between 70 and 250 mV (common settings for radiographic work).

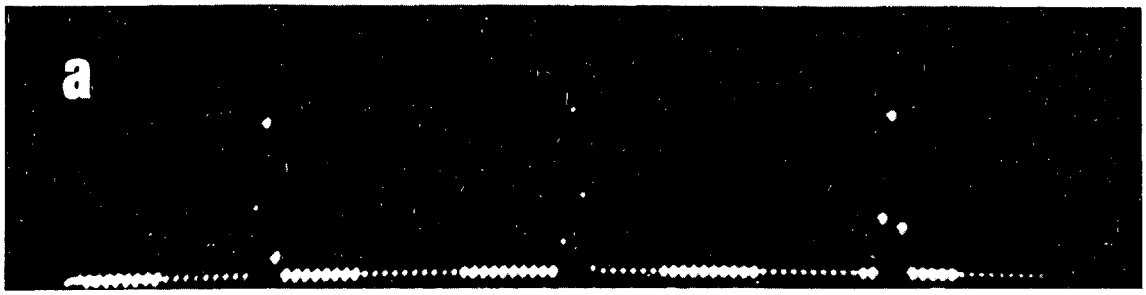

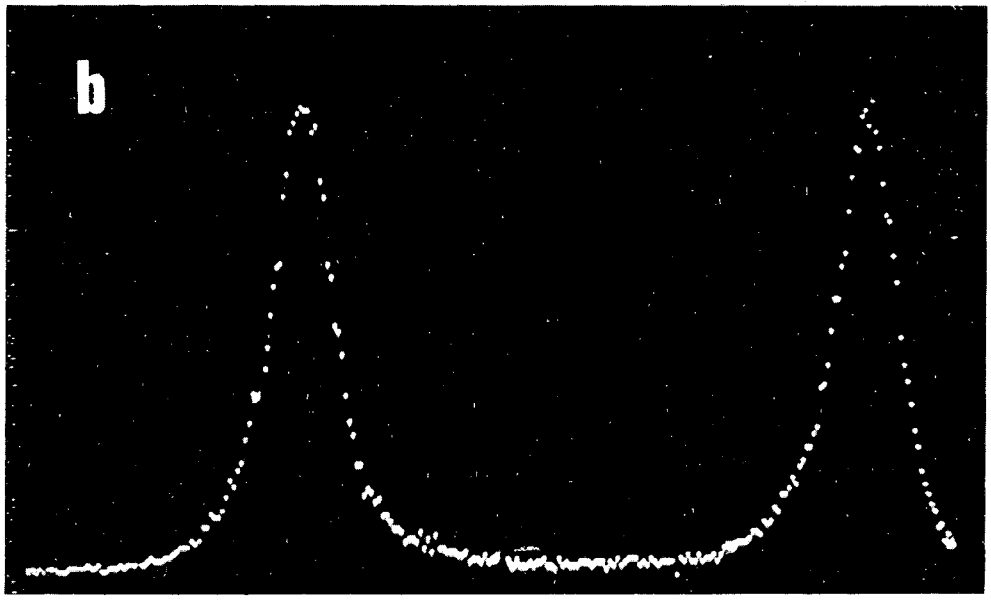

XBB-742-868

Fig. 23. Electronic timing accuracy. (a) Constant amplitude, 500 mV pulses. (b) Low energy portion of alpha-particle spectrum.

As in (a), the x-TAC output was collected in a PHA and a 20.4 nsec length of cable was added between the timing discriminator and TAC to produce the separate peaks. The FWHM of the peaks in this case is about 2.8 nsec or 0.4 mm. Inclusion of larger amplitude pulses in the SCA acceptance window does not change the shape of the peaks to any great extent because the increased slew is compensated by the decreased average jitter.

V. EXPERIMENTAL MEASUREMENTS

While visual inspection of test images provided much insight concerning the relative qualitative performance of the system, quantitative resolution and efficiency data was needed in order to make meaningful comparisons with other radiographic imaging systems and with results obtained from computer simulation programs.

A. Discussion of Measurements

The detection efficiency of an MWPC imaging system is of special interest. Since the amount of photographic effect which can be obtained from the interaction of a single neutron is essentially unlimited, there is no lower limit on the neutron fluences which are necessary to produce visual images. Thus it is possible to produce images of a highly statistical nature and the required fluence depends only on the detection efficiency and the desired image statistics. In the case of more conventional image recorders employing converting screens and film, the finite photographic speed generally requires so many neutron interactions to form a useful image that statistical considerations can be ignored.

A variety of methods has been used to specify the resolving power of imaging systems.[60] Many methods are based on measurements of the S-shaped response curve that is obtained when the system is used to image a knife edge. Two such methods are demonstrated in Fig. 24. In Morgan's method,[61] the unsharpness is taken to be the distance between the intersections of the projected maximum slope with minimum and maximum mean density lines. For Klasens' method,[62] a line is projected through the 0.16 and 0.84 density increase points and the unsharpness is taken as

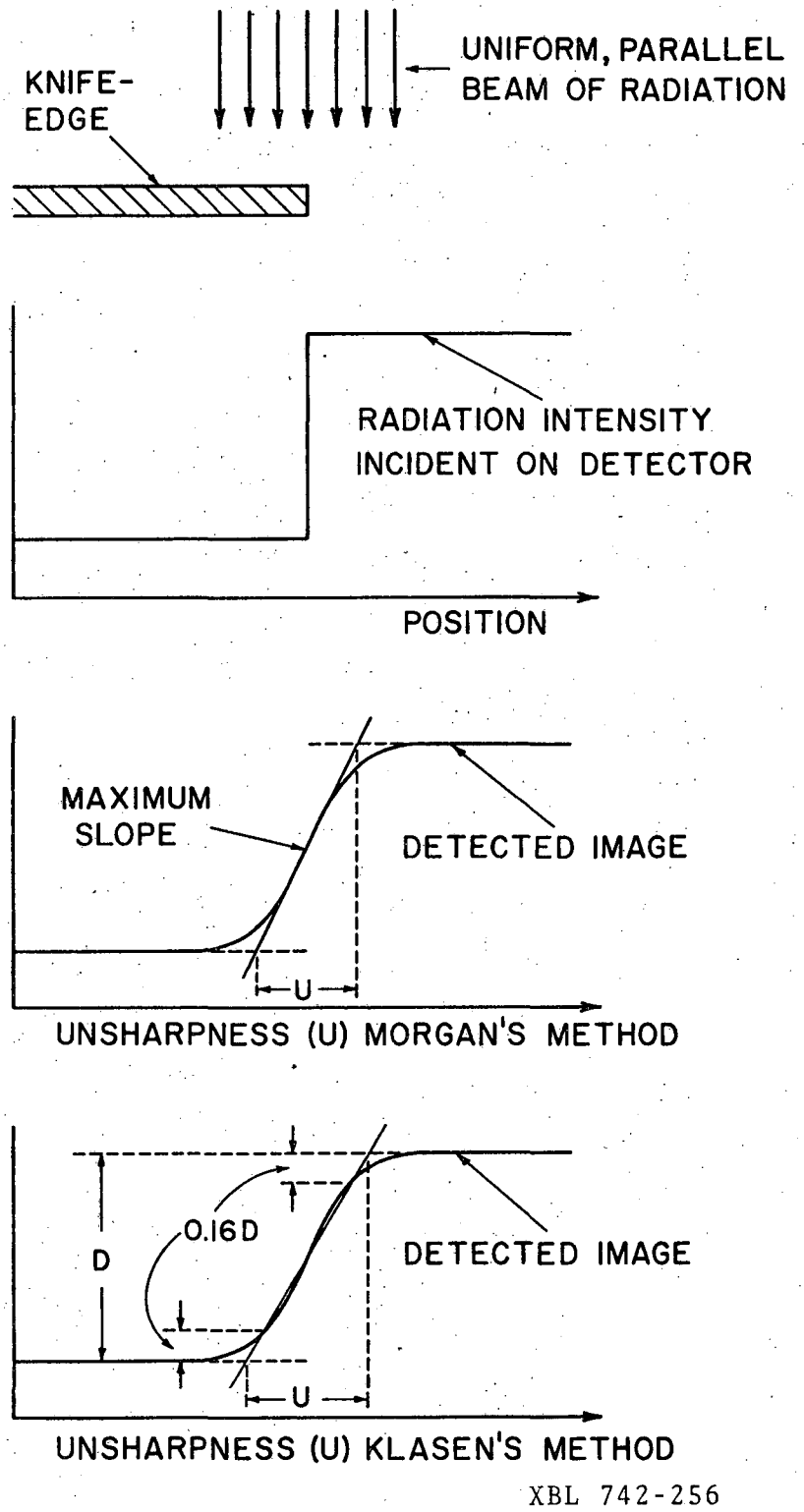

Fig. 24. Morgan's and Klasens' methods for specifying resolving power.

the distance between the intersections of this line with minimum and maximum mean density lines. Regardless of the exact details of the method used, the single unsharpness figure thus obtained can be used to successfully compare systems only when the knife-edge image response curves have similar shapes. For the comparison of systems with basically different response characteristics or for the description of a system whose response characteristics can be substantially altered through variable parameters, a more complete description of the resolving capability is necessary.

The modulation transfer function (MTF) offers such a complete description of resolution, and is an exact analog to the temporal frequency response of an electronic system. At a given spatial frequency the value of the MTF (contrast ratio) is the fraction of sinusoidal modulation which is transferred from the system's input to its output.[63] For imaging systems the input is generally referred to as the object function and the output as the image function. For optical imaging systems it is not too difficult to produce the spatial sinusoidal variations in light intensity for the object function. For instance, a focused beam of light transmitted through a photographic plate which contained the sinusoidally varying image would suffice. However, for more penetrating radiations such as high energy x-rays or neutrons, such controlled variations are more difficult to produce. For low energy x-rays or thermal neutrons, masks can be made which will modulate the radiation beam in a square wave fashion. The Fourier sine or cosine series of both the object function and the resulting image function can then be obtained and the contrast ratio can be calculated for the fundamental frequency or for any odd harmonic. For better accuracy, a separate mask can be prepared for each frequency to

be measured. Alternatively, an image of a knife-edge or a slit can be obtained in lieu of the sinusoidal image. Since both the step function and the idealized Dirac-delta function contain all frequencies, continuous Fourier analytical techniques can be used to deduce the MTF from their images (see Appendix C).

Aside from providing much more information than a single unsharpness figure, MTF's have the added advantage that they are commutative. That is, the MTF for an imaging system is just the product of the MTF's for each component of the system. Thus, for an imaging system consisting of N components and at any spatial frequency, ν,

$$MTF_{system}(\nu) = \prod_{k=1}^{N} MTF_k(\nu) \quad . \tag{25}$$

In practice, MTF's can be assigned to the image detector, electronic components (if any), the beam collimation, and even to characteristics of the radiographic subject. This property of MTF's is extremely useful since in some cases it allows component MTF's which are difficult to measure directly to be calculated from more easily obtained data.

While the present range of biological applications of neutron radiography is rather limited, this area is still of potential interest. The human body contains 10 percent by weight hydrogen, and the total neutron cross section due to hydrogen is several orders of magnitude larger than that of the next most abundant element.[64] Thus a neutron radiograph of a biological sample is essentially a map of the sample's hydrogen distribution. Although considerable research has been done over the past several years to investigate diagnostic applications for neutron radiography,[65]

I am not familiar with any *in vivo* clinical usage. However, successful employment of neutron radiography to determine the adequacy of bone margins in a surgically removed tumorous jaw bone has been reported.[66] The high sensitivity of the MWPC imaging system could permit quantitative *in vitro* diagnostics and increase the feasibility of *in vivo* experimentation. To this end, the total neutron cross section of an organic compound (Lucite $C_{18}H_{29}O_7$) was measured at thermal, epicadmium, and fast neutron energies. Lucite was chosen for the measurement because its hydrogen content (8 percent by weight) is similar to tissue and it can be easily machined to the desired shape.

Neutron attenuation through the boron converters for the 10 × 10 inch chamber was also measured. As mentioned in Sec. IV-B, attempts to overcoat the ^{10}B converters were unsuccessful and when the aluminum overcoat flaked off, an unknown amount of ^{10}B was carried away with it. For comparison with computer calculations, it was necessary to know how much boron remained. Since the microscopic neutron cross section of ^{10}B is well known, a measurement of the thermal neutron attenuation of the converter coating provided this information.

B. Prototype Chamber Measurements (Efficiency and Resolution)

Quantitative measurements taken with the prototype chamber were confined to preliminary efficiency and resolution measurements. Since the sensitive area of the chamber was not clearly defined because of the graduated edge wires, a 0.020-inch-thick sheet of cadmium with a 0.500-inch-diameter hole in it was placed over the chamber so that only a small central portion of the chamber was illuminated by the neutron flux. By measuring

counting rates with and without another sheet of 0.020-inch-thick cadmium placed over the hole, the thermal neutron detection efficiency was established.

For resolution measurements, four plates consisting of parallel arrays of cadmium strips were prepared to modulate the neutron beam in a square-wave fashion. These plates were fabricated by gluing 0.020-inch-thick cadmium to 0.125-inch-thick aluminum backings and then milling precision slots through the cadmium at equal intervals so the cadmium strips were the same width as the slots. The four spatial periods thus obtained were 10, 6, 4, and 2 mm. The system's response to each plate was collected in a PHA. Since the sensitivity of the chamber was not constant over its sensitive area, the system response to neutron beam only was also collected in the PHA so the plate data could be normalized by channel-by-channel division. The reduction of such data to yield resolution information is discussed in detail later.

The maximum detection efficiency which was obtained was 0.34% and the results of the resolution measurements are shown in Fig. 32 for comparison with the results obtained from the larger MWPC.

Several images of stencil letters cut in 0.020-inch-thick cadmium and 0.016-inch-thick lead are shown in Fig. 25. The images on the left were taken with a ^{55}Fe x-ray source and those on the right with the thermal neutron beam. In addition to demonstrating the transparency of lead to thermal neutrons, Fig. 25 also demonstrates the difference in event localization along the two coordinate directions. Due to the geometric fanout which was obtained between the chamber and the delay lines, individual anode wires are easily discernible in the images. The gap near the bottom

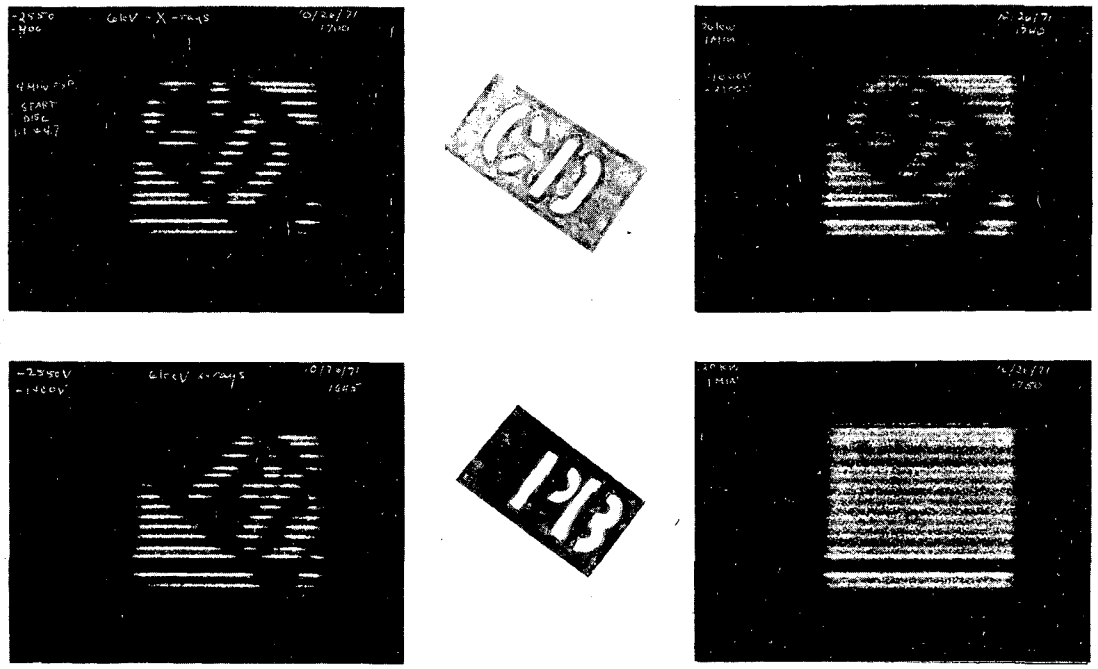

XBB-7110-5206

Fig. 25. ^{55}Fe x-ray (left) and thermal neutron (right) radiographs of 5/8-inch-high stencil letters.

of the images is due to a broken anode wire. The more diffuse nature of the line structure in the neutron images is due to the longer-range α-particles which can initiate avalanches on more than one anode. When this happens, the event can be localized at a position between wires.

C. 10 × 10 Inch Chamber Measurements

1. Boron Coating Areal Density Measurement

Since the thicknesses of the boron coatings on the converting surfaces were on the order of 4 μm (0.0002 inch), mechanical measurements were not attempted. However, this thickness of natural boron will attenuate a thermal neutron beam by about 5%, and 92% enriched ^{10}B provides about 20% attenuation. This effect is large enough to permit a simple measurement of the neutron attenuation. The coating thickness can then be related to the fractional attenuation through the macroscopic cross section for the (n,α) reaction.

The boron thickness of the powdered-boron converter was already determined by weighing samples during preparation so it was installed in the chamber as a back-converter and the chamber was used as the neutron detector. Each converter was then positioned in the thermal neutron beam so only about half of the active chamber area was shadowed by the boron coating. This procedure provided a sizable area of zero attenuation to which the attenuated area could be normalized. The area selector was used to limit chamber response to a six-inch-wide strip across its center to eliminate effects due to attenuation in the thick aluminum converter frame. The data were collected in a PHA. As with all quantitative measurements, data were also collected with no attenuator

in the beam for normalization purposes. After channel-by-channel normalization, data were added to increase statistics before the attenuation ratios were calculated. The results of these measurements are presented in Table V below.

Table V

Material	Fractional Transmission (FT)	Thickness (mg/cm^2) (T)
92% ^{10}B	0.834 ± 0.003	0.86 ± 0.02
92% ^{10}B	0.951 ± 0.004	0.24 ± 0.02
B^{nat}	0.966 ± 0.004	0.83 ± 0.09

Thickness values were obtained from the relation, $T = \frac{1}{\Sigma_c} \ln(\frac{1}{FT})$, using values for the macroscopic cross section (Σ_c) of 0.042 mg/cm^2 for natural boron and 0.211 mg/cm^2 for 92% enriched ^{10}B.

The natural boron converter was measured as a test of the method since its surface was still intact and test foil weight measurements made during deposition indicated that its thickness should be about 1.0 mg/cm^2. In spite of having the proper boron thickness, the detection efficiency of this converter was only a third to a half as large as efficiencies obtained from thinner natural boron layers. A loss factor this large is probably due to an error in the aluminum overcoat thickness resulting in significant α-particle absorption. Due to the poor performance of this converter, the data presented in the next section for natural boron is for the same converter used in the prototype chamber.

2. Neutron Detection Efficiency

The thermal neutron detection efficiency of the system was obtained by count rate measurement over a restricted area of the chamber where the thermal neutron flux was known to be fairly constant. Area delineation was achieved through the use of the area selector on the pileup rejector. Count rates were measured with and without 0.020-inch-thick cadmium in the beam and the thermal detection efficiency was based on the difference between these two count rates.

Since ^{10}B is very nearly a perfect 1/v absorber well into the epithermal neutron energy regime, epithermal detection efficiencies can be scaled approximately from the thermal efficiency using the relation

$$\eta(E_n) = \sqrt{0.025/E_n}\ \eta_{thermal} \qquad (26)$$

where E_n is the incident neutron energy in eV's. For our particular thermal reactor beam the cadmium ratio based on gold foil measurements was 6.3 whereas the cadmium ratio as determined by the chamber was about 20. This difference is probably due to the large absorption resonance of gold at 5 eV and the presence of a significant number of 5 eV neutrons in the beam.

Fast neutron detection efficiency measurements using a 1.5 mm-thick sheet of polyethylene as a converter were made using the 2×10^7 neutron/sec Pu-Be source. With the source located a known distance from the center of the 10 × 10 inch converter, the fraction of the total neutron yield which was intercepted by the chamber could be calculated. Count rate measurements were made first with the source in front of the chamber (so the recoil

protons are ejected into the active volume) and then with the source at a symmetrical position in back of the chamber. By taking the difference between the front and back counting rates, background and source-gamma effects were eliminated.

For the case of ideally flat converter coatings of very uniform thickness, the neutron-to-charged-particle conversion process can be modeled analytically. The resulting expressions yield the detection efficiencies that can be expected from such layered converters. In the following derivation it is assumed that the neutron beam is normally incident on the layer (see Fig. 26 for geometry).

The fraction of incident neutrons per unit area which undergo conversion reactions in material lying between x and x + dx is $\Sigma_c \exp[-\Sigma_t(T-x)]dx$ where Σ_c is the macroscopic cross section for the conversion reaction and Σ_t is the total macroscopic attenuation cross section. The charged particles will be emitted from dx with some angular distribution, $f(\theta)$, so the number of charged particles emitted from dx at x into $d\theta$ at θ per incident neutron is

$$d\eta = \Sigma_c \exp[-\Sigma_t(T-x)]f(\theta)dxd\theta \quad . \tag{27}$$

The charged particles represented by Eq. (27) must travel a distance, $x/\cos(\theta)$ to reach the converter-gas interface at which point their residual range is $R(E_i) - x/\cos(\theta)$, where $R(E)$ is the particle range as a function of energy and E_i is the initial energy of the charged particle. Since the particles must deposit a minimum threshold energy, E_t, in the gas in order to be detected, their effective range for detection is

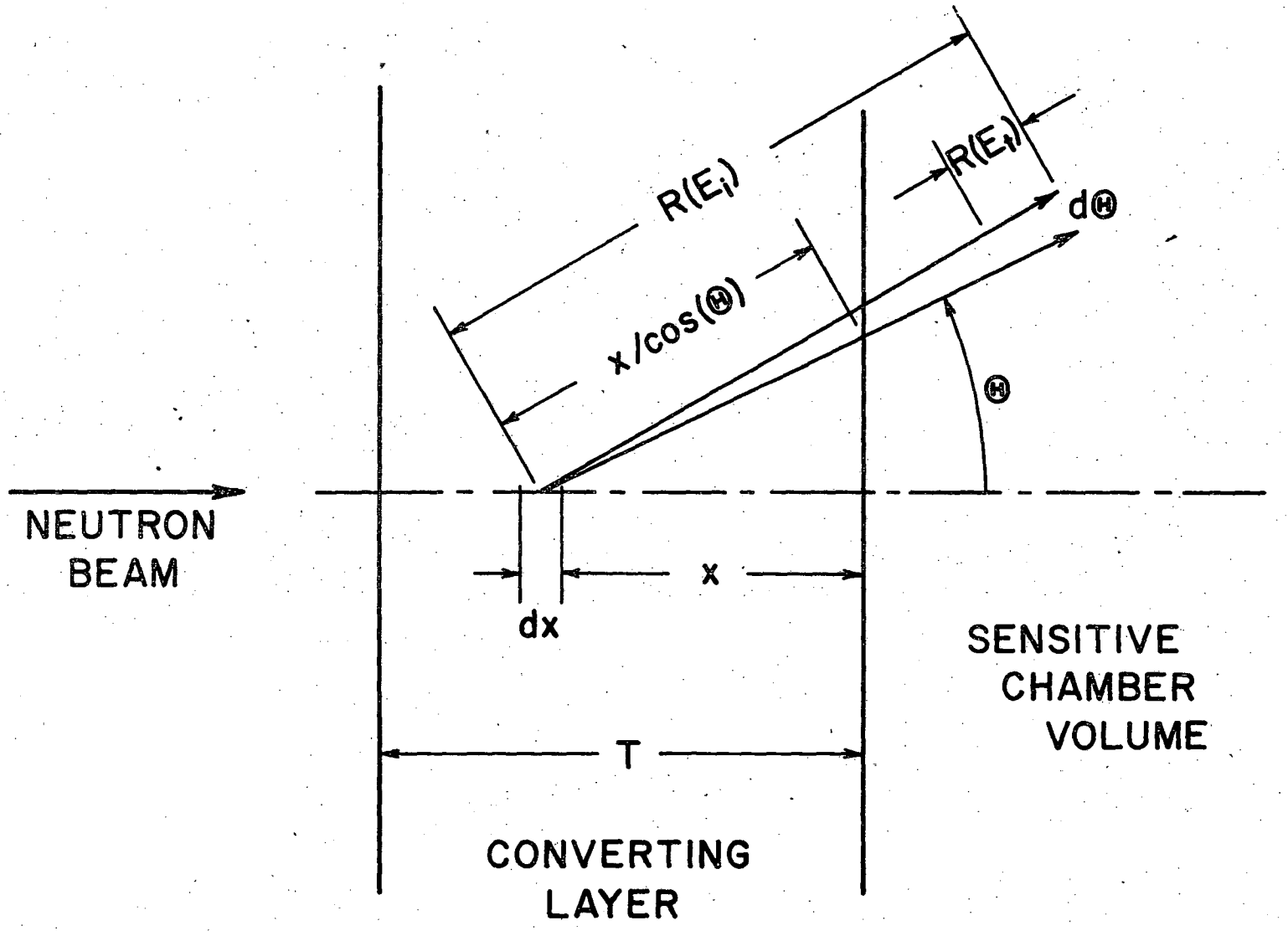

Fig. 26. Geometry for converter efficiency calculation.

$R_e = R(E_i) - R(E_t)$. The total number of charged particles emitted into the gas volume with an energy greater than E_t is obtained by integration over the variables, x and θ,

$$\eta = \int_0^{\pi/2} d\theta \int_0^{x^*} dx \Sigma_c \exp[-\Sigma_t (T-x)] f(\theta) \qquad (28)$$

where x^* is the lesser of $R_e\cos(\theta)$ and T. For exothermic conversion reactions involving thermal or epithermal neutrons, memory of the incident neutron energy is lost and the charged particles are emitted isotropically at a constant energy, E_i, with the corresponding constant range, $R(E_i)$. Substitution of $f(\theta) = \frac{1}{2}\sin(\theta)$ into Eq. (27) and integration yield

$$\eta = \frac{\Sigma_c \exp(-\Sigma_t T)}{2\Sigma_t} \{[\exp(\Sigma_t T^*)-1](1 + \frac{1}{\Sigma_t R_e}) - \frac{T^*}{R_e} \exp(\Sigma_t T^*)\} \quad . \qquad (29)$$

where T^* is the lesser of T and R_e. For enriched boron, Σ_t is very nearly equal to Σ_c so the efficiency becomes

$$\eta_f = \tfrac{1}{2}\exp(-\Sigma_c T)\{[\exp(\Sigma_c T^*)-1](1 + \frac{1}{\Sigma_c R_e}) - \frac{T^*}{R_e} \exp(\Sigma_c T^*)\} \qquad (30)$$

where the f subscript on η denotes the efficiency for a front-converter (one which is interposed between the beam and the gas volume). However, when charged particle emission is isotropic, a back converter (one placed on the downstream side of the gas volume) can also emit particles into the gas volume. Changing the exponential in Eq. (28) to $\exp(-\Sigma_c x)$ and integrating yields

$$\eta_b = \tfrac{1}{2}\{[1 - \exp(-\Sigma_c T^*)](1 - \frac{1}{\Sigma_c R_e} + \frac{T^*}{R_e}\exp(-\Sigma_c T^*)\} \quad . \tag{31}$$

Note that the back-converter efficiency given by Eq. (31) is the number of detectable charged particles per incident neutron on the back-converter. However, when a front-converter of thickness, T_f, is also used, the flux reaching the back-converter will be attenuated by the factor, $\exp(-\Sigma_c T_f)$. Thus, for a double converter system, the detection efficiency is

$$\eta_{fb} = \eta_f + \exp(-\Sigma_c T_f)\eta_b \quad . \tag{32}$$

The Q-value of the (n,α) reaction in ^{10}B is about 2.8 MeV. About 92% of the reactions are accompanied by a γ-ray with an energy of approximately 0.5 MeV. The remaining 2.3 MeV divides between the α-particle and the lithium recoil nucleus according to conservation of momentum with about 1.5 MeV going to the α-particle and 0.8 MeV to the Li-recoil. In the other 8% of the reactions, no γ-ray is emitted resulting in slightly longer range particles. For analytical purposes, the longer ranges of this group are ignored.

Since the α-particle and the Li-recoil are colinear, either one or the other is emitted toward the converter-gas interface and the total detection efficiency due to both kinds of particles is simply the sum of the detection efficiencies for each, or

$$\eta_f = \eta_f^{\alpha} + \eta_f^{Li} \tag{33a}$$

and

$$\eta_b = \eta_b^{\alpha} + \eta_b^{Li} \quad . \tag{33b}$$

In Table VI is a comparison of the detection efficiencies measured in the single back-converter mode for the various boron converters along with values calculated from Eq. (31) for different detection thresholds. The experimental detection threshold is estimated to be about 100 keV and alpha-range data was obtained from Ref. 67. Since the range indicated for a 1.5 MeV α-particle was rather high (1.03 mg/cm^2) compared to other values found in the literature, the calculations were repeated by linearly scaling Ref. 67 data to yield a value of 0.81 mg/cm^2 at 1.5 MeV.[68] In all cases, the Li-recoil ranges were obtained by scaling the α-particle ranges according to

$$R_{Li}(E/M) = \frac{M_{Li}}{M_{\alpha}} \frac{Z_{\alpha}^2}{Z_{Li}^2} R_{\alpha}(E/M) \quad . \tag{34}$$

Values used for Σ_c in natural boron and 92% enriched ^{10}B were 0.042 cm^2/mg and 0.211 cm^2/mg respectively (at 0.025 eV).

Comparison of experimental anode pulse height spectra with spectra predicted on the basis of data obtained from Ref. 67 indicated that the α-particle ranges in argon were too long. Considering this in addition to the lower range values quoted in the literature, it is likely that the values calculated for $R_{\alpha}(1.5) = 0.81$ mg/cm^2 are the more realistic. Even so, the experimental detection efficiencies are low by about a factor of two. While some of the loss can be attributed to errors in the experimental

Table VI

E_t \ T		^{10}B powder 1.03 mg/cm^2	^{10}B 0.86	^{10}B 0.24	B^{nat} 0.70	
0.0	α	5.06	4.94	2.18	0.96	
	Li	1.68	1.68	1.57	0.34	
	α + Li	6.74	6.62	3.75	1.30	
0.05	α	4.45	4.44	2.14	0.89	
	Li	1.29	1.29	1.28	0.26	
	α + Li	5.74	5.73	3.42	1.15	
0.10	α	4.19	4.19	2.12	0.85	Calculated
	Li	1.07	1.07	1.07	0.22	$R_\alpha(1.5)=1.03$ mg/cm^2
	α + Li	5.26	5.26	3.19	1.07	
0.20	α	3.82	3.82	2.08	0.79	
	Li	0.87	0.87	0.87	0.17	
	α + Li	4.69	4.69	2.95	0.96	
0.50	α	2.98	2.98	1.97	0.61	
	Li	0.39	0.39	0.39	0.08	
	α + Li	3.37	3.37	2.36	0.69	
0.0	α	4.04	4.04	2.11	0.83	
	Li	1.32	1.32	1.32	0.27	
	α + Li	5.36	5.36	3.43	1.10	
0.05	α	3.55	3.55	2.05	0.73	
	Li	1.01	1.01	1.01	0.20	
	α + Li	4.56	4.56	3.06	0.93	
0.10	α	3.33	3.33	2.03	0.69	Calculated
	Li	0.84	0.84	0.84	0.17	$R_\alpha(1.5)=0.81$ mg/cm^2
	α + Li	4.17	4.17	2.87	0.86	
0.20	α	3.04	3.04	1.98	0.62	
	Li	0.68	0.68	0.68	0.14	
	α + Li	3.72	3.72	2.66	0.76	
0.50	α	2.36	2.36	1.83	0.47	
	Li	0.31	0.31	0.31	0.06	
	α + Li	2.67	2.67	2.14	0.53	
0.10	α + Li	2.27	2.07	1.12	0.38	Experimental

threshold, imperfect energy resolution, and errors in the determination of the coating thickness, consideration of the data in Table VI shows that these errors would have to be unreasonably large to account for the entire loss. It is more likely that the major part of the loss is due to irregularities in the coating thickness to be discussed in part D. However, the double converter efficiencies calculated from Eq. (32) using experimental values for η_f and η_b were in good agreement with the experimental double converter efficiency. The maximum efficiency obtained using a powdered ^{10}B back converter and a 0.86 mg/cm^2 front converter was 3.76%.

The qualitative behavior of the detection efficiency as the incident neutron energy is varied is shown in Fig. 27. The curves were obtained from Eqs. (30), (31), and (32) using $\Sigma_c(E) = \sqrt{\frac{0.025}{E}}\,\Sigma_c(0.025)$ where E is the neutron energy in eV. An optimum thickness for thermal energy was assumed for the front-converter and the back-converter was assumed to be of at least optimum thickness. Note that for cold neutrons with energies below 10^{-3} eV, the single back-converter is most efficient. This is due to self-shielding in the front-converter and shielding of the back converter in a double converter system which increases at lower energies. For energies greater than 0.05 eV, the efficiency scales as $1/v$ and $\eta_f \approx \eta_b \approx \frac{1}{2}\eta_{fb}$.

Fast neutron detection efficiencies for hydrogenous recoil proton converters can also be obtained from Eq. (28). In this case, the CM angular distribution of scattered protons is $\frac{1}{2}\sin(\theta_{CM})$. Transforming to laboratory coordinates yields $f(\theta) = \sin(2\theta)$. In addition, the initial proton energy is a function of the scattering angle, $E_i = E_n\cos^2(\theta)$ where

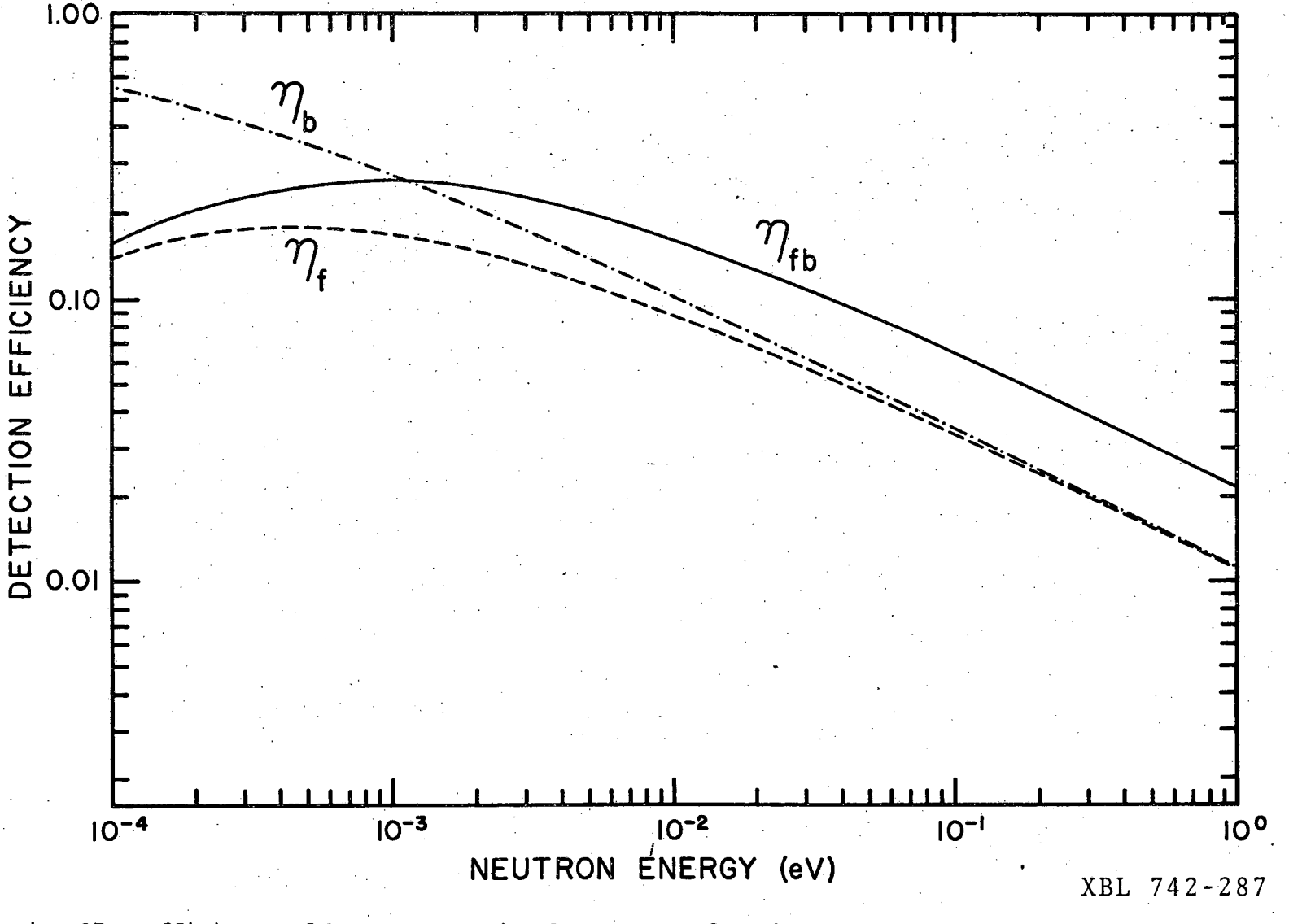

Fig. 27. Efficiency of boron converting layers as a function of incident neutron energy.

E_n is the incident neutron energy. With $f(\theta) = \sin(2\theta)$ and $R_e = R(E_n\cos^2(\theta)) - R(E_t)$, Eq. (28) becomes

$$\eta = \int_0^{\pi} d\theta \int_0^{x^*} dx\Sigma_c \exp[-\Sigma_t(T-x)]\sin(2\theta) = 2\Sigma_c \exp(-\Sigma_t T) \int_0^1 \mu d\mu \int_0^{x^*} \exp(\Sigma_t x)dx \quad (35)$$

where the transformation $\mu = \cos(\theta)$ has been applied and x^* is the lesser of $R_e(\mu)\mu$ and T. Equation (35) can be integrated analytically with respect to x resulting in

$$\eta = \frac{2\Sigma_c \exp(-\Sigma_t T)}{\Sigma_t} \int_0^1 \mu d\mu [\exp(\Sigma_t x^*)-1] \quad . \quad (36)$$

In general, the integration with respect to μ is not analytic unless an analytic model is assumed for R(E).

The efficiency given by Eq. (36) is the number of protons per incident neutron which are ejected from the converter with an energy greater than E_t by first collisions. While protons can be ejected from the converter as a result of second, third, and higher order collisions, the correction to Eq. (36) is small. An expression similar to Eq. (36) was derived for the second collision efficiency and evaluated numerically for several values of E_n in the 1 to 20 MeV range with $T = R(E_n)$ for polyethylene. As might be expected, the results indicated that $\eta_2 \lesssim [1-\exp(-\Sigma_t T)]\eta$ where η and η_2 are the first and second collision efficiencies respectively and $1-\exp(-\Sigma_t T)$ is the probability that the first collision occurs. For polyethylene, this probability is less than 5%.*

*Data for Σ_c and Σ_t taken from Ref. 13 and proton range data taken from Ref. 69.

Figure 28 shows the detection efficiency that can be expected from a 1.5 mm thick polyethylene converting layer as a function of neutron energy. The curves labeled LLD = 0 and LLD = 1 MeV were obtained by numerical integration of Eq. (36) and the remaining curves were obtained from a more detailed simulation program which treats the proton energy deposition in the gas. The term LLD refers to a lower level discriminator setting and is to be identified with E_t in the foregoing. An infinitely thick chamber is one in which the gas volume is thick enough to stop the most energetic proton. In practice it could be realized with a highly pressurized filling of a dense gas such as xenon or isobutane. The initial rise of the curves is due to increasing proton range and the fall is due to decreasing scattering cross section.

If the incident neutrons are not monoenergetic, the efficiency can still be obtained from Eq. (36). Denoting the neutron energy spectrum with the normalized flux distribution, $\phi(E_n)$, the efficiency becomes

$$\eta_{spectrum} = \int_0^\infty \eta(E_n)\phi(E_n)dE_n \quad . \tag{37}$$

Equation (37) was numerically evaluated for a Pu-Be source spectrum[70] resulting in a value of 0.10%. The experimentally obtained value was also 0.10%. The good agreement between these two numbers supports the non-uniform layer argument to account for low thermal efficiency since the polyethylene surface was visibly smoother than the boron surfaces.

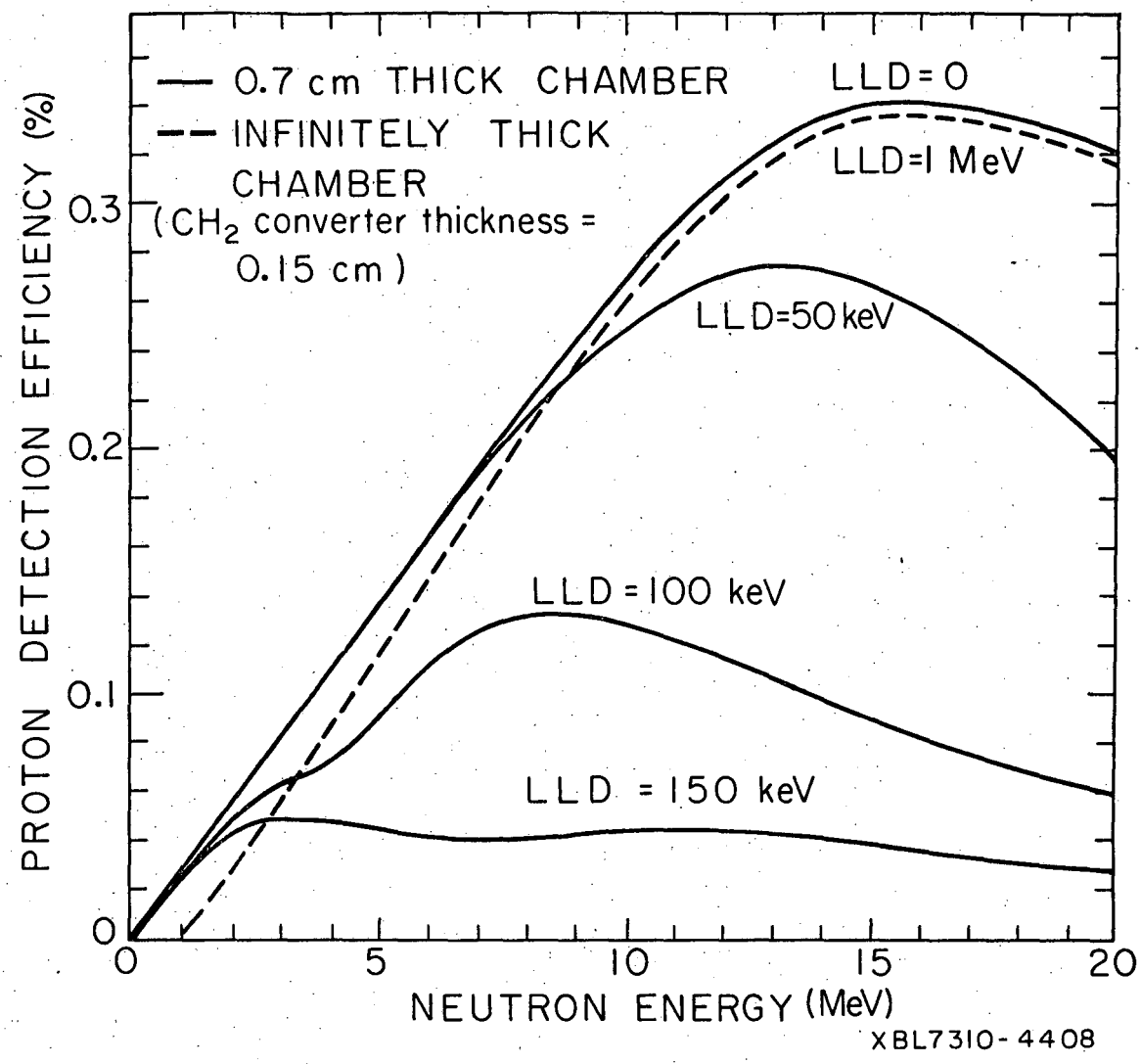

Fig. 28. Detection efficiency of recoil proton converter as a function of incident neutron energy.

3. Resolution

The first resolution measurements of this system were made using a ^{55}Fe x-ray source which emits a 5.9 keV x-ray. Electrons released by photoelectric conversion of the x-rays in the chamber filling gas have very short ranges in the gas (< 1 mm) and will localize very near the conversion point. Therefore the system resolution, as measured with ^{55}Fe x-rays, is not degraded by the effect of longer range particles which tend to localize at some distance from their point of origin. Denoting the ^{55}Fe MTF by MTF_{55} and assigning $MTF_{(n,\alpha)}$ to the (n,α) conversion and localization process, the total neutron MTF is given by

$$MTF_{total}(\nu) = MTF_{55}(\nu) \times MTF_{(n,\alpha)}(\nu) \quad \text{or} \quad MTF_{(n,\alpha)}(\nu) = \frac{MTF_{total}(\nu)}{MTF_{55}(\nu)} \qquad (38)$$

where advantage has been taken of the commutative property of MTF's. It is necessary to isolate the function $MTF_{(n,\alpha)}(\nu)$ since it is this function which is calculated by the computer simulation program.

For the first attempt at measuring the ^{55}Fe MTF, masks were made which modulated the x-ray intensity in a square wave fashion. Full size (10 × 10 inch) photographic bar patterns were first prepared with the width of the spaces between the parallel bars exactly equal to the width of the bars. Four patterns were made with spatial periods (width of bar plus space) of 20 mm, 10 mm, 4 mm, and 2 mm which provide the fundamental spatial frequencies of 0.05, 0.10, 0.25, and 0.50 cycles/mm respectively. These bar patterns were then transferred to 3.3 mil thick capton with a 1-oz copper cladding using the same process employed in the etching of PC boards. After the bar patterns were etched into the

cladding to form the masks, more copper was electroplated onto the bars so the masks could also be used with the more energetic 22 keV x-ray of ^{109}Cd. A total copper thickness of 5 mils was desired but uniformity of thickness and edge straightness were difficult to maintain during the electroplating and consequently the finished copper thickness varied from 2.4 mils for the thinnest mask to 4.5 mils for the thickest. Also, the width of the bars tended to increase slightly during the electroplating. The corrections for asymmetrical masks and effects due to transmission through the copper or absorption in the capton are developed in Appendix C.

In use, the masks were attached to an aluminum frame which was mounted on the chamber in such a way that the bars of the mask could be accurately aligned perpendicularly to the anode wires by means of a screw adjustment. This orientation was chosen so the mask images could be obtained by PHA readout of the cathodes which run perpendicularly to the anodes, thus avoiding the effects associated with anode spacing as discussed in Sec. III. The aluminum frame positioned the mask 2.0 cm away from the plane of the anode wires and the source was positioned 20.0 cm upstream of the mask. This geometry reduced the effects of finite source size and geometric magnification. The front of the chamber was fitted with a 0.001-inch-thick aluminum-flashed mylar window to allow access of the 5.9 keV x-rays into the active chamber volume.

Initial measurements using these masks were made with a chamber filling of 7% methane in argon but the maximum obtainable gain of the chamber (corresponding to the highest anode voltage that did not initiate spark breakdown; about 2300 V) barely raised the ^{55}Fe photopeak above the detection threshold. Nanoamplifiers with a gain of 5 were inserted between

the amplifiers and the timing discriminators but this solution did not effect the signal-to-noise ratio in any beneficial way. Anode pulse height discrimination was used to include only pulses of the photopeak and data was collected for each of the four spatial frequencies. Data was also collected with no attenuator in front of the chamber so local chamber gain and efficiency variations could be normalized out through channel-by-channel division of the bar pattern data. Identical measurements were made using the ^{109}Cd source in order to observe the effect of the longer range ^{109}Cd photoelectrons.

Analysis of the resolution data described above was disappointing. Better performance was expected from the system and the poor resolution was attributed to the low signal-to-noise ratio. In order to increase the gain of the chamber, a mixture of 23.52% isobutane, 4% methylal and 0.48% freon 13-B1 (CF_3Br) by weight in argon was substituted for the argon-methane mixture. This gas has extremely good spark suppression properties and allows much higher voltages to be applied to the anodes. It also increases the space charge limit on electron gain through partial space charge cancellation by low mobility, negative freon ions.[71] However, increased gain is obtained at the expense of decreased proportionality due to electron capture on the electronegative freon. Using this gas mixture, the chamber gain was easily increased by a factor of four by raising the anode voltage to 3000 V with no indication of spark breakdown.

In addition to changing the filling gas to increase the gain of the chamber, it was decided to try a different technique for performing the resolution measurements. The bar pattern masks were extremely useful

in that the image modulation at each frequency was directly observable. Also, the measurements were integral in the sense that the response from the entire chamber was recorded. However, use of the bar pattern masks required a separate measurement for each mask, and data analysis yielded not the MTF curve, but only discrete points lying on the curve. On the other hand, all frequencies are present with equal amplitude in the Dirac delta function so a single measurement of the system's response to a delta-function radiation source contains all the information necessary to compute the entire MTF curve. In practice it is impossible to construct a true delta function source but it is simple to correct for a finite width line source (see Appendix C). The response of a system to a line source excitation is appropriately called the line spread function (LSF)[72] and the MTF is simply the Fourier transform of the LSF with corrections for finite line width.

A ^{55}Fe x-ray line source was fabricated by milling a 3/16-inch-wide slot in a piece of 1.05-inch-thick Lucite and fixing four 0.005-inch-thick brass plates with cleanly sheared edges to both sides of the slot so as to form two parallel 0.010-inch-wide slits separated by the thickness of the Lucite. With the ^{55}Fe x-ray source located over one of the slits, a line of 5.9 keV x-rays is projected from the other slit. Geometric effects tend to increase the width of the beam as the distance from the source is increased and the actual intersection of the beam with a finite thickness detector is slightly trapezoidal in nature.

An identical construction was used to fabricate a ^{109}Cd line source except that 0.020-inch-thick lead was substituted for the brass and the sides of the Lucite block were also covered with lead.

To maximize the data collection rates and minimize spreading of the beam, the line sources were located as close as possible to the chamber (touching the mylar window). They were then accurately aligned perpendicularly to the anodes and the line source images were collected in a PHA. Also, at this time, LSF's were obtained under the same conditions as the bar mask data.

Comparison of the x-ray line source data with the bar mask data obtained under the same conditions showed good agreement. Since slits are easier to make than periodic bar patterns and slit measurements yield more information than bar pattern measurements, the line source method was chosen for measuring the neutron resolution. Two pieces of cleanly sheared 0.020-inch-thick cadmium were clamped to a 1/16-inch-thick aluminum plate and the gap was accurately set with a feeler gauge. The aluminum plate was then fastened to the chamber in such a way that the angular alignment could be set with a screw adjustment. Resolution measurements were made in the beam port exposure facility with the cadmium slit aligned perpendicularly to the anodes.

Fast neutron resolution measurements using the polyethylene converter consisted of obtaining the image of the edge of a 2-inch-thick block of Lucite using an unmoderated Pu-Be source. As with all other resolution measurements, the edge of the Lucite was aligned perpendicularly to the anodes and the cylindrically shaped source was placed with its axis normal to the plane of the chamber and its front face about 140 cm from the anode plane.

The LSF's obtained for the ^{55}Fe and ^{109}Cd line sources using the isobutane mixture are shown in Fig. 29. Background has been subtracted

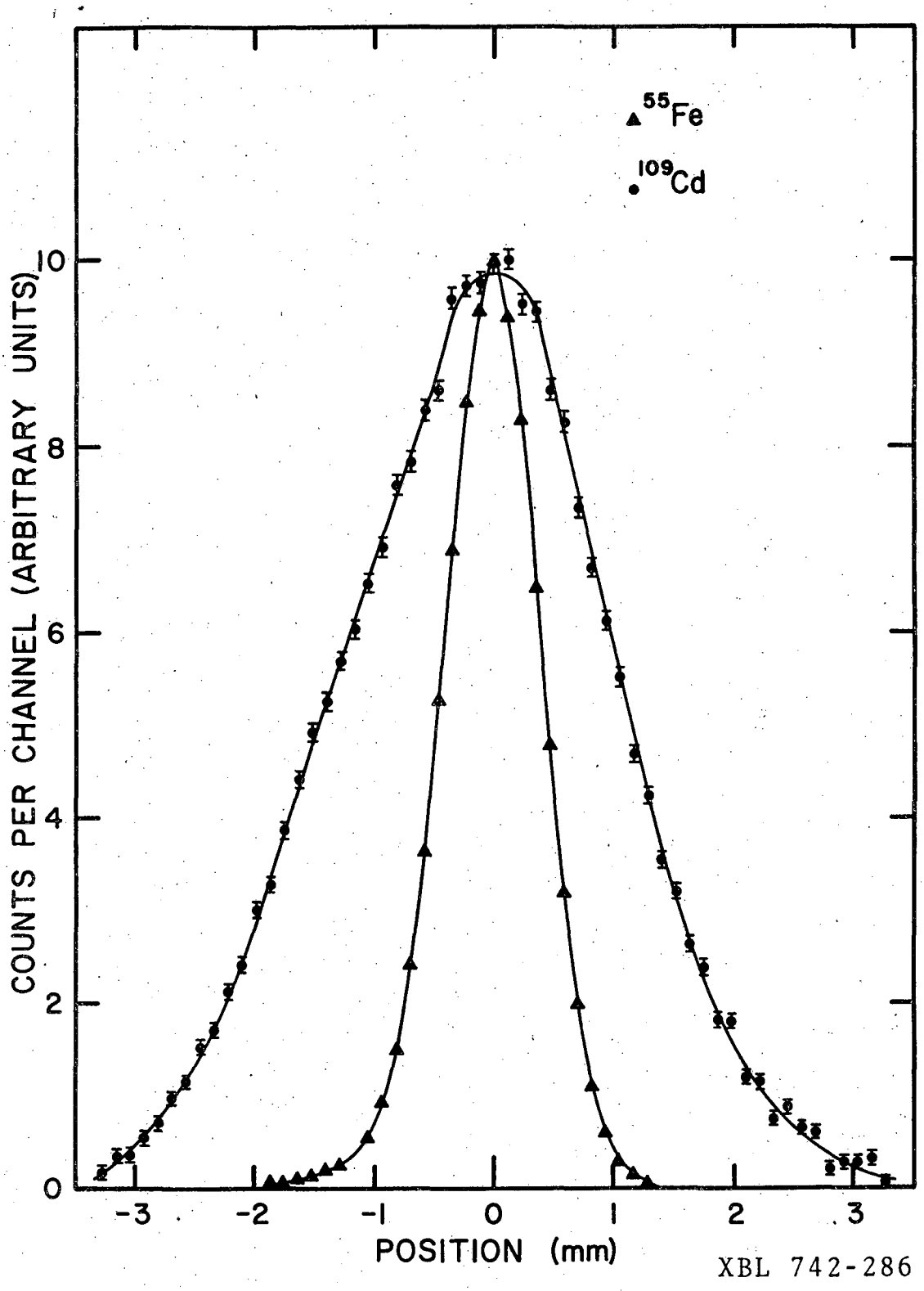

Fig. 29. Experimental LSF's obtained using ^{55}Fe and ^{109}Cd line sources.

and both peaks have been normalized to a maximum height of 10. The longer range of the ^{109}Cd photoelectron is seen to increase the half-width of the LSF by approximately 2 mm near the base. The extrapolated range of a 22 keV electron is about 0.9 mg/cm^2 which is 5 mm in argon at STP.* Considering the probabilistic manner in which electrons lose energy and the fact that the chamber localizes the event at its center of ionization, the observed effect is about right.

The data presented in Fig. 29 were used as input for a Fourier transforming program to calculate the MTF's shown in Fig. 30. The MTF's obtained with the argon-methane mixture at lower gain are also shown. Higher contrast ratios were obtained for both sources using the argon-isobutane mixture. The contrast ratio values obtained from the bar masks data using finite Fourier transforms are seen to be in good agreement with the LSF transforms obtained under the same experimental conditions.

Figure 31 shows a thermal neutron LSF obtained with a 1.00 mm wide Cd slit in the reactor beam. The energy discriminator levels of the SCA were adjusted to include only those α-particles which deposited between 0.27 MeV (LLD) and 0.61 MeV (ULD) in the sensitive volume of the chamber. The solid curve of Fig. 32 is the MTF corresponding to Fig. 31 and represents about the best resolution which was obtained with this imaging system. MTF's for other SCA settings are also presented. For the dot-dashed curve, LLD was lowered to the detection threshold (about 120 keV for the chamber gain which was employed during data taking). In principle,

---

*The electron range in argon was obtained from aluminum range data using the approximation that the range in g/cm^2 is independent of the atomic number of the absorber (Ref. 38, p. 18).

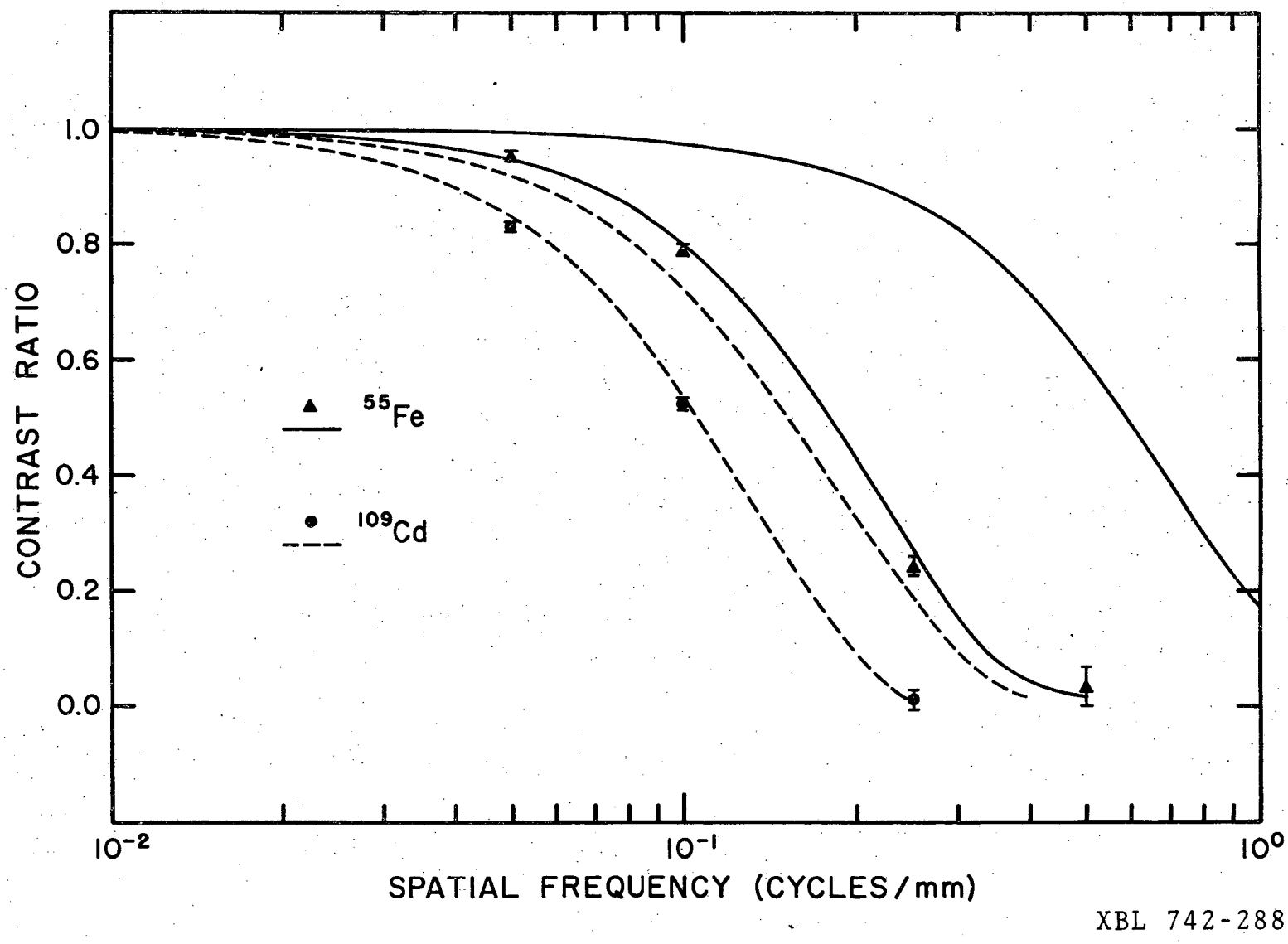

Fig. 30. MWPC experimental x-ray resolution. The MTF curves were obtained from transformation of line source data and the points were obtained from bar mask measurements.

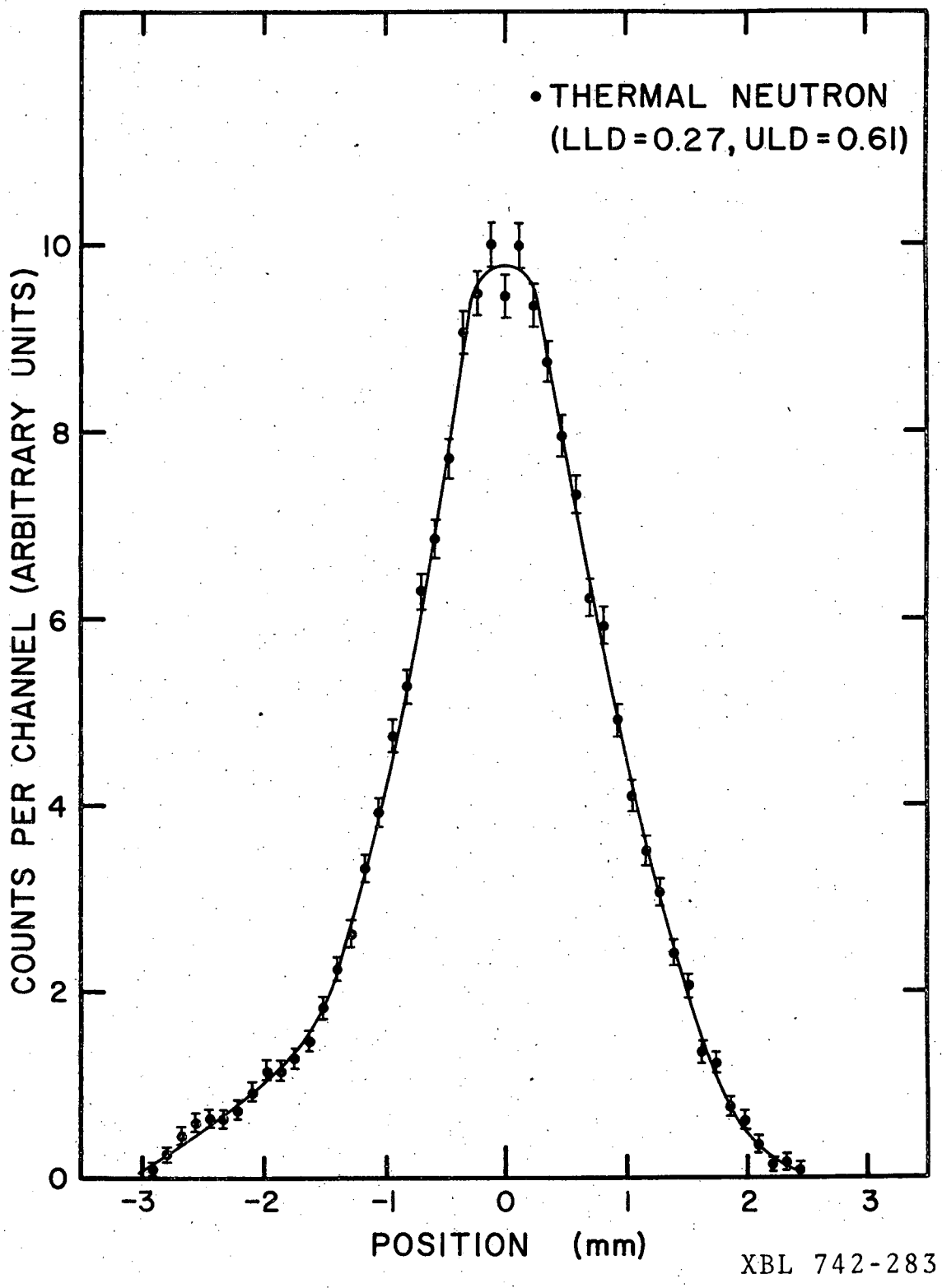

Fig. 31. Experimental LSF using thermal neutrons and a ^{10}B back converter.

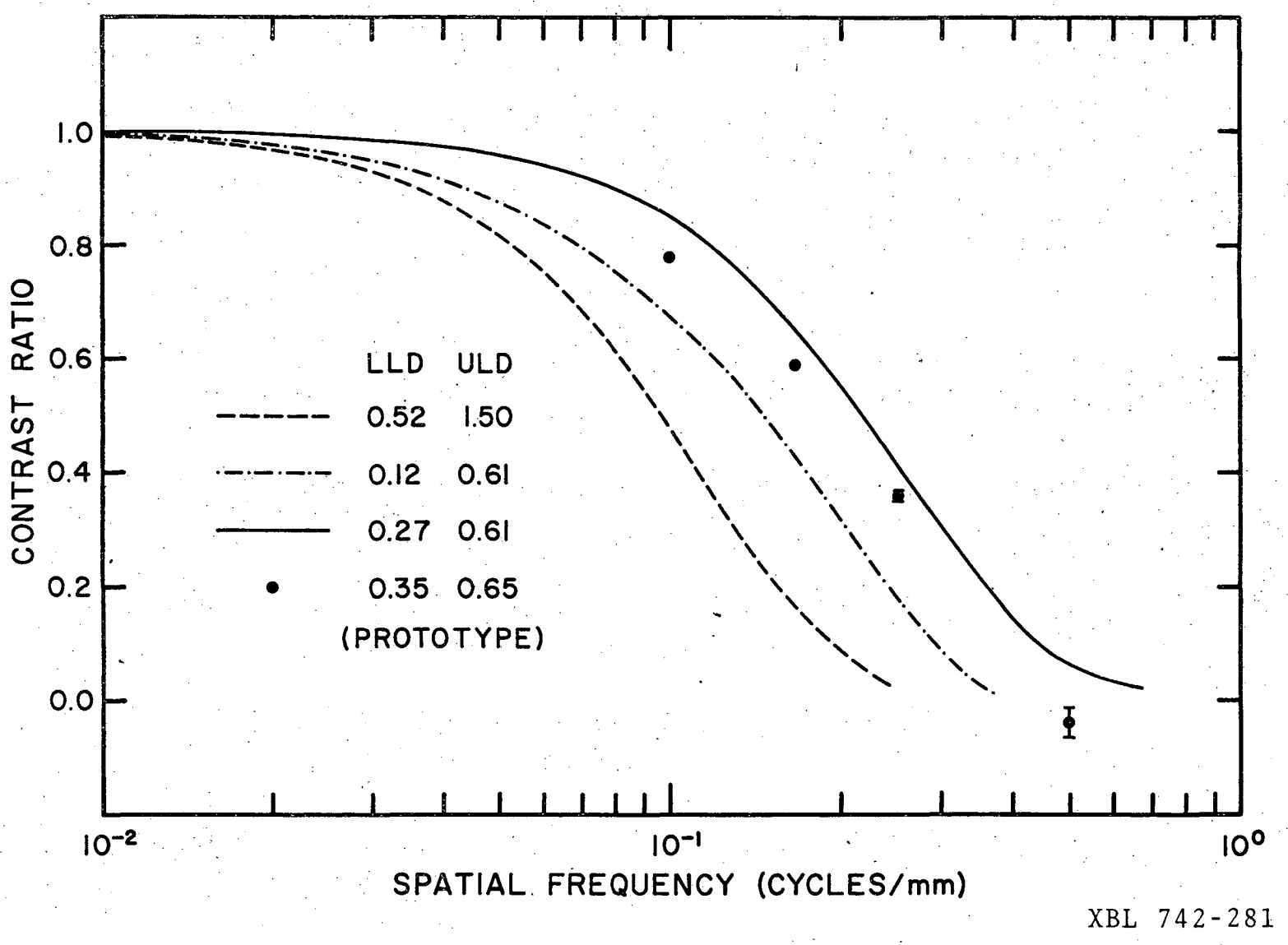

Fig. 32. MWPC experimental resolution with thermal neutrons and a ^{10}B back converter. The data points are for measurements made with the prototype chamber using Cd bar masks.

the inclusion of low energy, short range α-particles should improve the resolution of the system but the effect is seen to be just the opposite due to the decreased accuracy with which low amplitude pulses are processed. The dashed curve is the system's response when the SCA is set to include only the α-particles which deposit more than 0.61 MeV in the chamber. The degradation of resolution due to the longer ranges is evident.

The PHA conversion ratio was chosen small enough (about 0.11 mm/channel) that the statistical nature of the experimental LSF's had very little effect on the MTF calculations. Several experimental LSF's were artificially smoothed (e.g., by reading points from a fitted curve as in Fig. 31) and the resulting MTF's differed insignificantly from those calculated from the data in the region of interest. This is to be expected since for spatial periods that are large compared to the conversion ratio, the MTF calculation itself is a data averaging routine.

The choice of slit width, 2a, depends on the maximum spatial frequency to which the MTF calculation is to be extended. The correction factor for slit width has its first singularity at $\nu = 1/2a$ and in general, contrast ratio values calculated from statistical LSF's are unreliable near the singularity. On the other hand, unnecessarily thin slits are not desirable because they lead to low data collection rates and low signal-to-noise ratios. The transformation of several thermal neutron LSF's collected with a slit width of 0.35 mm showed that the MTF either tailed off to zero in the vicinity of 1 cycle/mm or was very slightly oscillatory about zero with amplitudes of 0.03 or less. Thus a 1.00 mm wide slit was chosen to improve the statistics in the frequency range of interest.

After correcting the fast neutron resolution measurement for source size, the 10-90% knife-edge resolution (distance between 10% and 90% of the density change across the image of the edge) was found to be about 4 mm. Due to the relatively long ranges of the more energetic recoil protons (0 to 10 MeV for a Pu-Be source) the resolution was expected to be on the order of half the active chamber thickness, so this value seems reasonable.

4. Lucite Attenuation Measurements

For the thermal neutron Lucite attenuation measurements, a test plate was prepared which consisted of parallel, ½-inch-wide bars of various Lucite thicknesses. The Lucite strips were separated by ½-inch-wide gaps in which were inserted ½-inch-wide strips of 0.020-inch-thick cadmium to reduce the number of neutrons reaching the chamber which carried no attenuation information. With an antiscatter grid* mounted between the chamber and the test plate, thermal neutron images of the test plates were collected in the PHA. After normalization, the attenuation ratios were calculated and the data least-square fitted to a simple exponential function of the form $\hat{y} = C\exp(-x/\lambda)+(1-C)$ which allows for a constant background. As can be seen in Fig. 33, the antiscatter grid is very effective in eliminating the scattered thermal neutrons. Image reversal, as from Fig. 33a to 33b, was obtained by rotating the test plate 180° with respect to the chamber to insure that the measured responses were symmetrical.

*The antiscatter grid consisted of a 12-inch-diameter piece of 1-inch-thick 3 mm hexagonal celled honeycomb which had been dipped in a gadolinia-loaded paint.

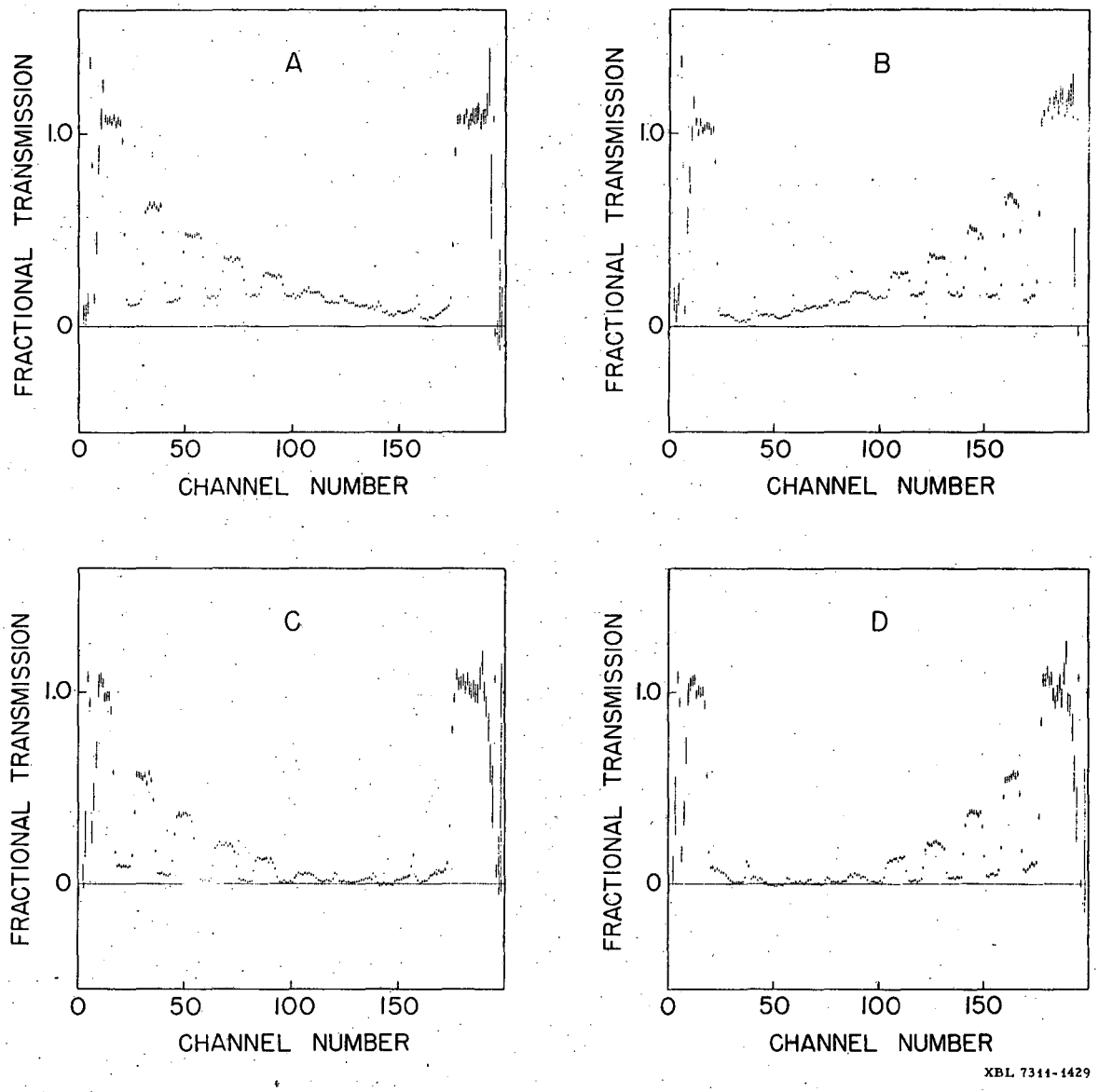

Fig. 33. PHA readouts of images of Lucite strip test plate; (a) and (b) were obtained without the antiscatter grid and (c) and (d) were obtained with the grid.

At epicadmium energies the absorption cross section of gadolinium falls off rapidly and the antiscatter grid becomes ineffective. For this reason, epicadmium attenuation measurements were done using only one Lucite thickness at a time to simplify the process of separating the response due to the directly transmitted beam from the total response. For epicadmium imaging using a 1/v type detector, neutrons scattered off hydrogenous material can be especially troublesome since they are detected more efficiently than the directly transmitted beam which contains the image information.

Fast neutron attenuation measurements with a polyethylene converter were also done one strip at a time using the Pu-Be fast neutron source.

The experimental data points, the curves obtained from least square fits of the function, $y = C\exp(-x/\lambda)+(1-C)$, and the fitting parameter, λ, are displayed in Fig. 34. For the cases of thermal and fast neutron attenuation, the λ-values are in good agreement with expected collision-mean-free path values for the average-energy neutron in each spectrum. By using the stoichiometric formula, $C_{0.62}H_{1.0}O_{0.24}$ ($C_{18}H_{29}O_7$), for Lucite and subtracting the weighted microscopic cross sections of carbon and oxygen, the effective hydrogen scattering cross section was found to be 53 barns for the thermal spectrum and 1.6 barns for the Pu-Be spectrum. When account is taken of the fact that the hydrogen is partially bound at thermal energies, the energy corresponding to the 53 barn cross section is 0.025 eV.* The energy corresponding to the fast 1.6 barn cross section is about 5 MeV.[13]

*Hydrogen binding was accounted for by using the effective hydrogen scattering cross sections in organic compounds (Ref. 14, p. 567).

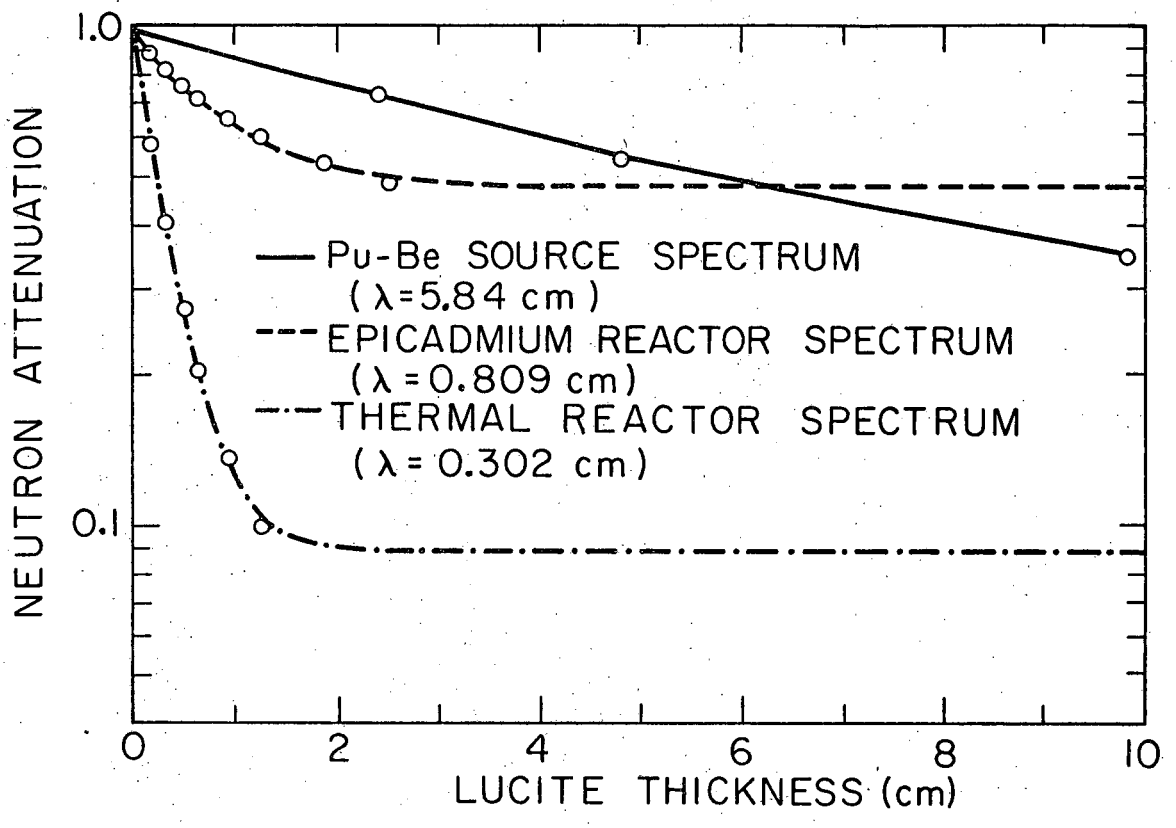

Fig. 34. Lucite attenuation data for thermal, epicadmium, and fast neutron energy spectra. The curves are least-square fits of the function $y = C\exp(-x/\lambda)+(1-C)$.

For the epicadmium reactor spectrum, the effective hydrogen scattering cross section indicated by the single exponential fit was found to be 17.5 barns. This is an unlikely value since the corresponding neutron energy is about 25 keV. To take better account of the γ-background (over 50% in this case) the epicadmium data was refitted using the function, $y = C\exp(-x/\lambda_n)+(1-C)\exp(-x/\lambda_\gamma)$, where λ_n and λ_γ are the attenuation mean-free-paths in Lucite for neutrons and γ-rays respectively. The resulting value of λ_n = 0.654 cm yields an effective hydrogen scattering cross section of 22.6 barns and a corresponding neutron energy in the neighborhood of 1 eV. The value obtained for λ_γ was 13.3 cm which corresponds to a γ-energy of about 1.1 MeV. The λ-values obtained from application of the double exponential fitting function to thermal and fast data were within 1% of those quoted in Fig. 34.

D. Performance Analysis Methods for Resolution and Comparison With Experimental Results

The Fortran computer program which was written to simulate the (n,α) conversion and localization process is basically an extension of Eq. (27) which was $d\eta = \Sigma_c \exp[-\Sigma_t(T-x)]f(\theta)dxd\theta$ where $d\eta$ is the number of charged particles per incident neutron which is emitted from dx at x into dθ at θ. For digital computation, Eq. (27) becomes

$$\Delta\eta_{ij} = \Sigma_c \exp[-\Sigma_t(T-x_i)]f(\theta_j)\Delta x_i \Delta\theta_j \quad . \tag{39}$$

However, instead of simply summing over i and j for the total detection efficiency, the history of each $\Delta\eta_{ij}$ is considered from its origin at some depth in the converting layer, x_i, to the point at which it stops in or leaves the active volume of the chamber.

The program treats energy deposition in the converting material, in a layer of nonconverting material (if one is present; e.g., an aluminum overcoat), and finally in the filling gas. Range-energy data is supplied in tables for the materials and particles involved. Finite differencing of x and θ is done in a linear fashion ($\Delta x_i = \Delta x_k$ for any i,k; $\Delta\theta_j = \Delta\theta_k$ for any j,k) with x_1 defining the layer of converter nearest the active volume and θ_1 defining the angular zone closest to the converter normal. The calculation begins at (i,j) = (1,1) and proceeds as outlined below.

1. $\Delta\eta_{ij}$ is computed according to Eq. (39) above.
2. The energy loss suffered by the charged particles as they pass through the converting layer and the nonconverting layer (if present) is computed and subtracted from the initial particle energy. For boron converters, both the α-particle and the Li-recoil are detectable and each is treated separately.
3. The particle range in the gas corresponding to the remaining kinetic energy at the gas interface is computed and the center of ionization of the track in the active volume is found.
4. If the energy deposition in the gas lies between LLD and ULD (set at the beginning of the problem), $\Delta\eta_{ij}$ is binned according to energy to form the energy spectrum. The distance between the point of origin in the converter and the center of ionization in the gas is then projected onto the anode plane and $\Delta\eta_{ij}$ is binned according to this length to form a radial profile of particle localization points.

When i and j have both run their full range, the first part of the calculation is complete, resulting in the energy spectrum, $n_e(E)$, of

detected particles and the radial density profile of localization points, $n_r(r)$. The detection efficiency, η, can be computed from either distribution as $\eta = \sum_i n_e(E_i)\Delta E_i = \sum_j n_r(r_j)2\pi r_j \Delta r_j$. In principle, the distribution, $n_r(r)$, is a complete indication of system resolution but is extremely difficult to measure experimentally, so $n_r(r)$ is used to compute simulated responses to experimental situations such as a knife edge or slit. These computed responses can then be compared directly with experimental results.

The only fast neutron experimental results were obtained with a Pu-Be source having a neutron energy spectrum extending from 0 to about 10 MeV. In this case, the flux was divided into weighted groups represented by an energy, E_i, and a weighting factor, ϕ_i, such that $\sum_i \phi_i = 1$. The calculation as outlined above in steps (1) through (4) was then repeated for each group, and contributions from each group to $n_e(E)$ and $n_r(r)$ were accumulated until the last group was processed.

In general, results of the program were in good qualitative agreement with experimental results. In many cases, reasonable quantitative agreement was also obtained. The major factor which is not treated in the program is the imperfect energy resolution of the physical system. Such factors as local variations in anode-wire-diameter and spacing or small variations in the plane spacing cause the electron gain to vary over the active chamber area. The FWHM of the photopeak of ^{55}Fe was measured to be approximately 20% and the energy resolution for charged particles should be approximately the same (assuming the electron gain is not saturated). Thus, the simulated energy acceptance window (LLD,ULD) is sharply defined whereas the experimental window includes some particles with energy less than LLD (and shorter ranges) and some particles with

energy greater than ULD (and longer ranges). In addition, the program does not suffer from detection threshold effects so that computed optimum performance characteristics are on the optimistic side.

Figure 35a shows computed energy spectra for a 0.24 and a 0.86 mg/cm^2 ^{10}B converting layer assuming the maximum α-particle range in boron to be 1.03 mg/cm^2. The curves were obtained by spreading each element of the program spectrum, $n_e(E_i)$, into a 20% FWHM Gaussian and rebinning. The knee in the curve labeled Li-recoils corresponds to the maximum Li-recoil energy and the peak labeled α-particles is due to the more energetic α-particles which traverse the entire active volume and stop in the opposing converter. Both curves have been normalized to the same area to clearly demonstrate the softer spectrum which is obtained from the thicker converting layer.

The calculation was repeated assuming the maximum α-particle range in boron to be 0.81 mg/cm^2. These results are shown in Fig. 35b. The experimental spectrum of the 0.24 mg/cm^2 ^{10}B converter obtained from pulse height analysis (approximately 0.01 MeV/channel) is also shown here since the agreement with calculation seemed to be better. The more rapid rise of the experimental spectrum at low energy is probably due mostly to core-gamma contamination in the reactor beam. It is interesting that the experimental spectrum follows the spectrum for a thick converter more closely than the thin converter spectrum. It is possible that the thickness of the coating could fluctuate over a wide range but still average to 0.24 mg/cm^2. In this case, the spectral contribution from thin areas would be characteristic of thin layers and similarly for the thick areas. The detected energy spectrum for such a converter would then be an

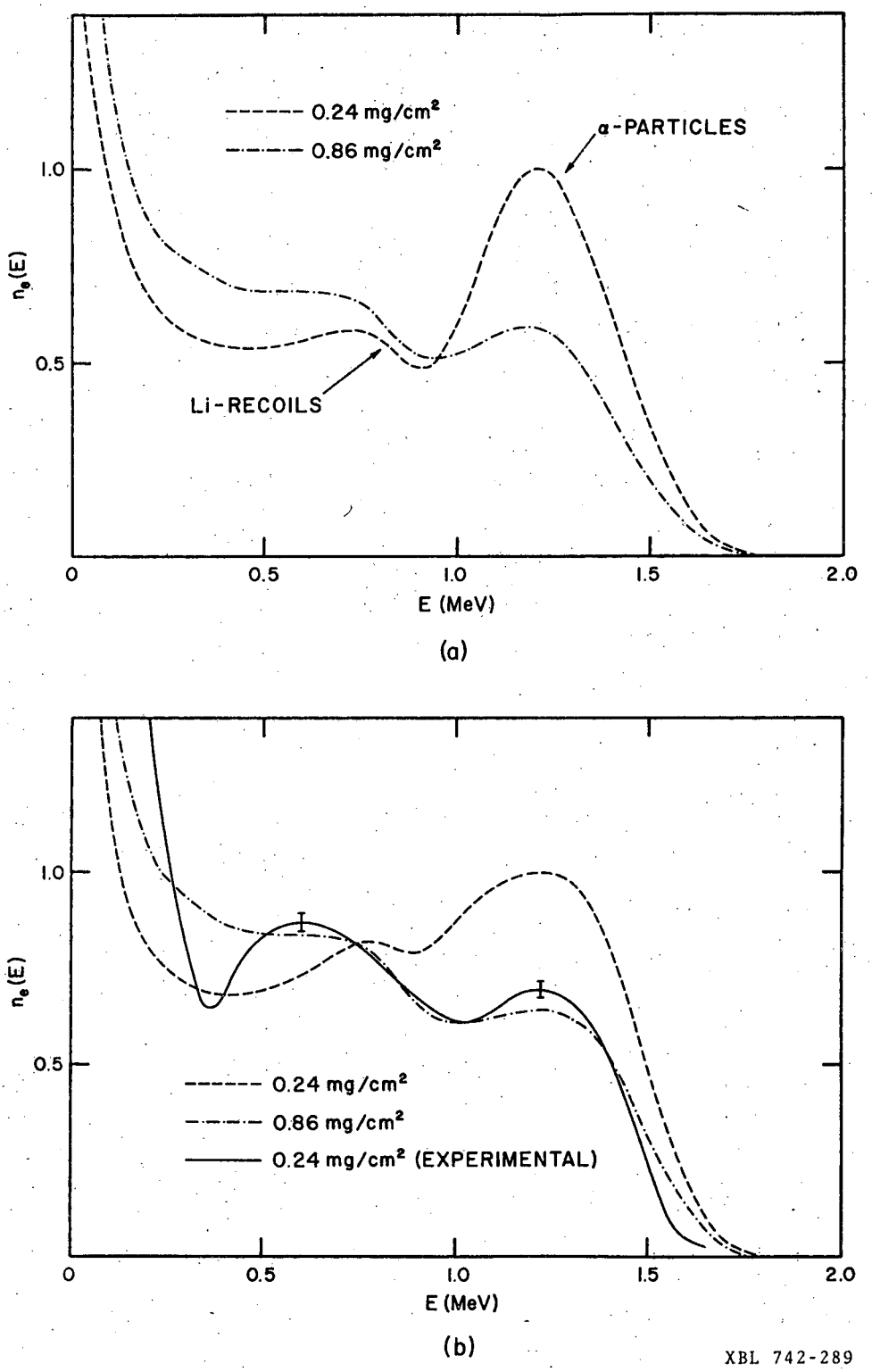

Fig. 35. Energy spectra of α-particles and Li-recoils from a boron converting layer. In (a) the range of a 1.5 MeV α-particle was taken as 1.03 mg/cm^2 of boron and in (b) the range was taken as 0.81 mg/cm^2.

average spectrum, the precise nature of which would depend on the details of the fluctuations. Thickness fluctuations also lower the detection efficiency since converting material which is "buried" below the average depth is necessarily less efficient in yielding charged particles to the active volume. This effect has been noted by other investigators and efficiency loss factors on the order of 30% have been reported.[68]

The SCA discriminator settings were calibrated in MeV according to Fig. 35b and then used as input parameters in the simulation program. In Fig. 36, the MTF for (LLD,ULD) = (0.27,0.61) has been repeated from Fig. 32 after adjustment according to Eq. (38). The program's response is shown as the dotted curve. The program predicted the occurrence of negative contrast ratios for energy discriminator settings which rejected a significant fraction of the shorter range particles. As a test of the theory, the system's response was measured at (LLD,ULD) = (1.35,1.50) and is also shown in Fig. 36 (after adjustment) along with the computed response. Phase inversions of this sort were also observed directly using the test plates of parallel cadmium strips with the prototype chamber.

A negative contrast ratio at a spatial frequency, ν, means that the system's image of a periodic test pattern of frequency, ν, will show the greatest response in areas of least excitation. In terms of images of real objects which cover the entire spatial frequency spectrum, it means that fine details will not be resolved at all, and gross details will have very indistinct edges. Needless to say, this type of response is to be avoided for imaging applications.

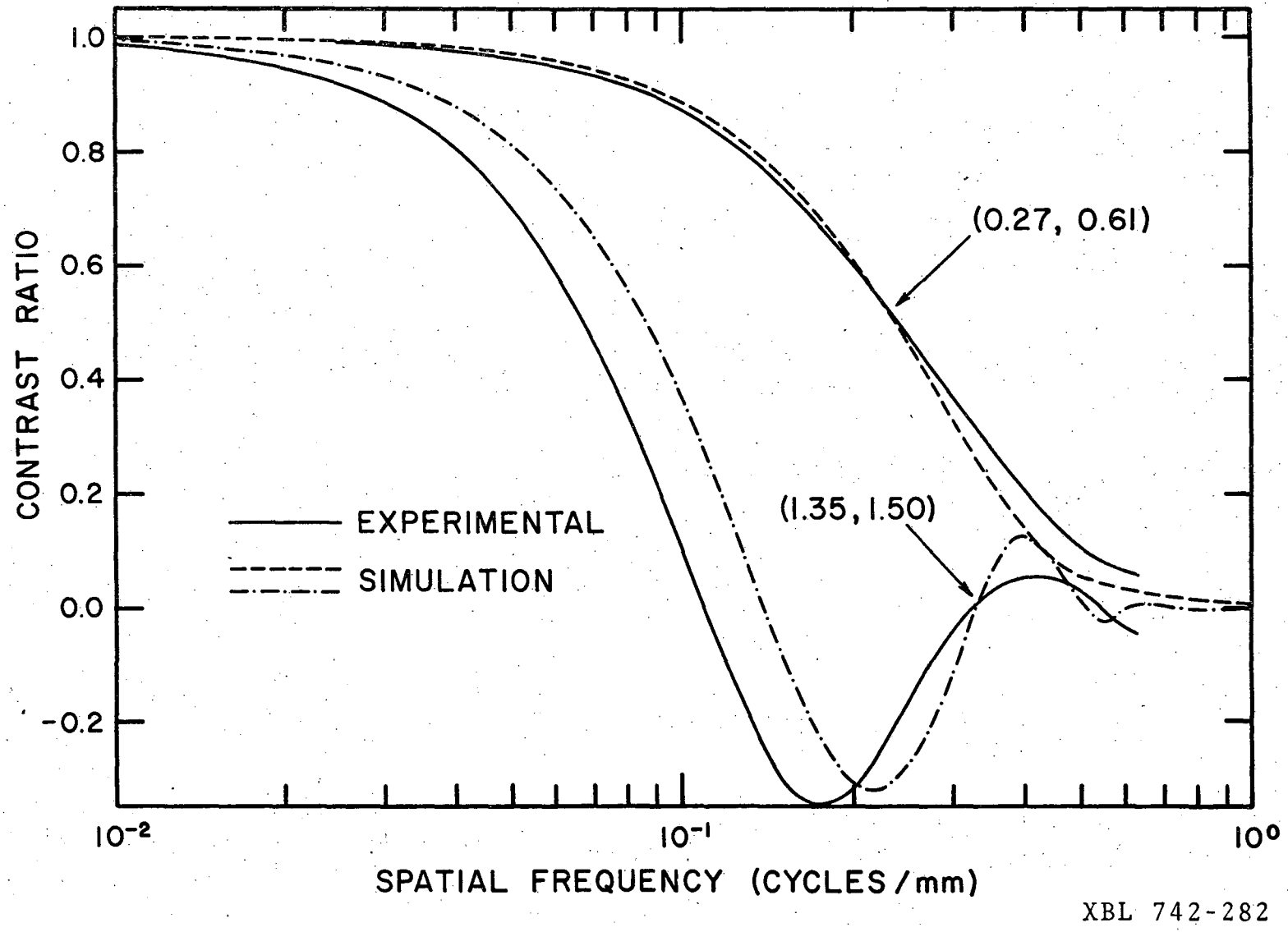

Fig. 36. Comparison of MTF's obtained from the simulation program with experimental MTF's.

Finally, the program was used to predict the approximate resolution that could be expected from the system in the absence of a lower level detection threshold (as mentioned previously, the low energy portion of the experimental pulse height spectrum was immersed in the core-gamma spectrum and the low amplitude pulses were not processed as accurately by the electronics). Figure 37 shows the results obtained for a 0.86 mg/cm^2 ^{10}B converter by including all particles in the acceptance window (ULD = 1.50), and then only the low energy half of the spectrum (ULD = 0.60). Comparison of Figs. 36 and 37 demonstrates the importance of including the lowest energy particles in the acceptance window.

If a high density filling gas and/or pressurization is employed to shorten the particle ranges, the ULD = 0.60 curve of Fig. 37 can still be used to estimate spatial resolution by scaling the abscissa. For instance, if the ranges are halved, then abscissa values should be multiplied by two. The same is not true of the ULD = 1.50 curve because this curve includes the effects of particles stopping in the opposing converter. Although the spatial resolution obtainable from the conversion process in ^{10}B can be increased by the use of pressurized, high density gases, the system resolution is still limited in one dimension by the anode wire spacing.

Also included in Fig. 37 are the computed MTF's for a 1.5 mm-thick polyethylene proton recoil converter used with a Pu-Be source. Again, the calculation was done for the total energy spectrum and the low energy half of the spectrum. Note that while many of the recoils possess energies in the MeV range, over 99% of them deposit less than 500 keV in the chamber due to their relatively long ranges. Further reductions in the ULD setting

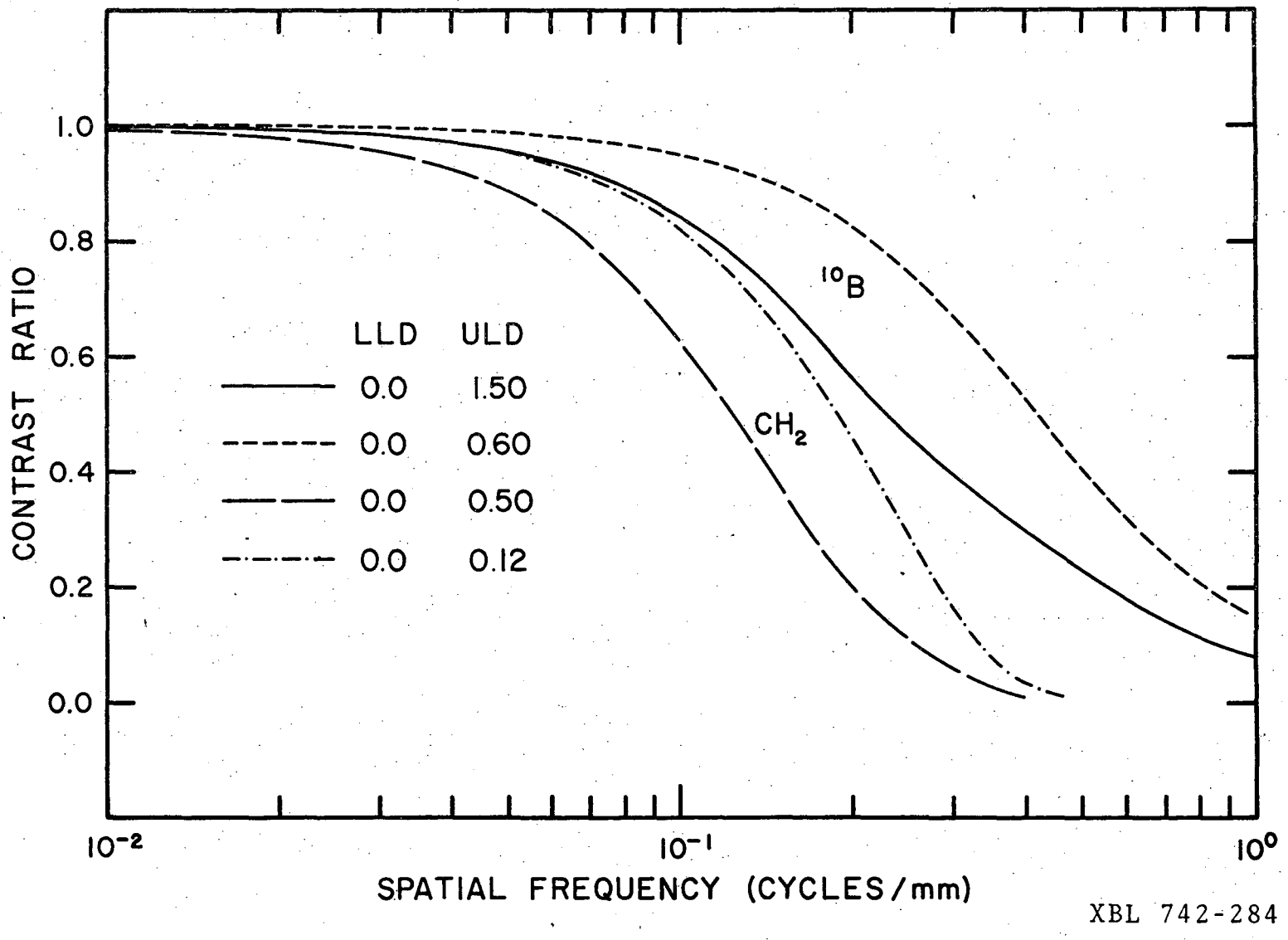

XBL 742-284

Fig. 37. MTF's obtained from the simulation program for a boron thermal neutron converter and a polyethylene (CH_2) fast neutron converter assuming no lower level detection threshold.

do not effect improvements as great as in the case of the ^{10}B converter due to the reduced correlation between track length and energy deposition.

VI. IMAGING WITH NEUTRON SENSITIVE MWPC

A. Direct CRT Imaging

The first radiographic images taken with the 10 × 10 inch chamber were obtained using direct CRT display during the exposure. The scope camera was loaded with 3000 speed Polaroid film and set on time exposure so the dots of light corresponding to individual interactions in the chamber were accumulated as they occurred in the latent film image. This is an extremely versatile detection technique since the photographic speed of the system can be varied over a virtually unlimited range. Through adjustment of the camera aperature and the CRT beam intensity, the speed can be increased to the point that single interactions produce large, completely exposed areas, or decreased to the point that repeated interactions are required to cause visible film darkening thus producing continuous tone radiographs.

Three examples of this method are shown in Fig. 38 which also demonstrates the correspondence between visual image quality and the MTF's presented in Sec. V. Figure 38a is a ^{55}Fe x-radiograph of two leaves (the range of suitable subjects for 5.9 keV x-rays is somewhat limited) taken under the same experimental conditions as the ^{55}Fe LSF shown in Fig. 29. The edge definition is good and the veins are clearly imaged. The lighter, circular areas in the lower leaf were dry spots. Figures 38b and 38c are thermal neutron radiographs of the same electric hand drill shown in Fig. 8b which were taken at different SCA energy discriminator settings. Figure 38b was taken under the same conditions as the thermal neutron LSF of Fig. 31 with (LLD,ULD) = (0.27,0.61). Figure 38c was

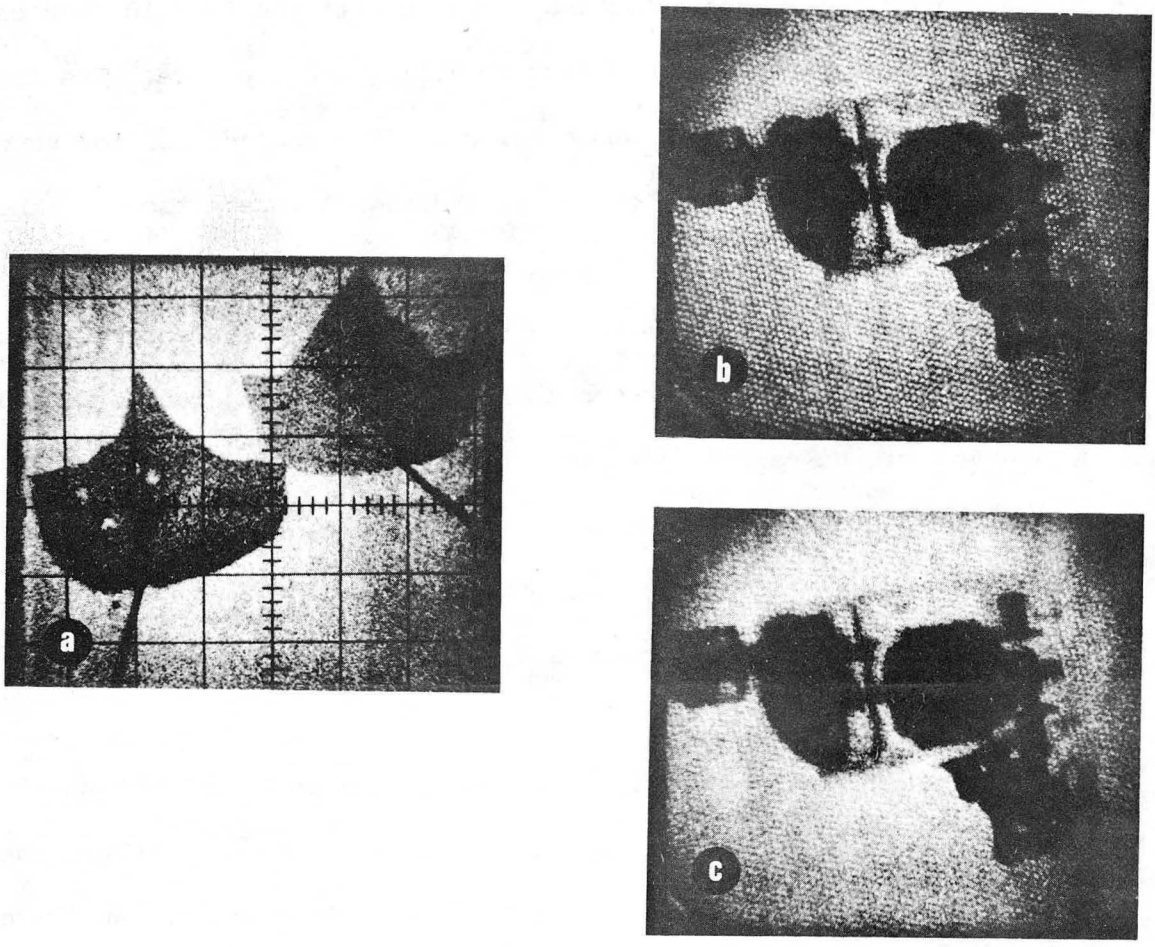

XBB-742-869

Fig. 38. (a) ^{55}Fe x-radiograph of leaves, (b) thermal neutron radiograph of drill using low energy portion of alpha-particle spectrum, (c) thermal neutron radiograph of drill using higher energy portion of alpha-particle spectrum.

taken with (LLD,ULD) = (0.61,1.20) and shows the degradation in spatial resolution due to inclusion of longer range particles. The mottled pattern superposed on the neutron radiographs is the image of the 3-mm-cell honeycomb antiscatter grid.

The images shown in Fig. 39 were also obtained by direct CRT display. Radiographs (a), (b), and (c) were taken prior to acquisition of the antiscatter grid but they still serve to demonstrate the effect of counting statistics on image quality. Radiograph (d) is repeated from the previous figure (38b) to show the improved sharpness provided by the antiscatter grid. The experimental conditions were constant for this set of radiographs (excepting the antiscatter grid and the camera f-stop) with neutron interaction densities of 5, 10, 60, and 40 mm^{-2} for (a) through (d) respectively. Image graniness is seen to increase for lower interaction densities, but even at the lowest density of 5 mm^{-2}, the essential features are still present.

B. Image Storage in 4096 Channel Analyzer

1. On-Line Readout

With the 4096 channel memory arranged into a 64 × 64 square matrix corresponding to the 25 cm square imaging area of the chamber, each element of the matrix corresponds to a 4 mm square area of the image. As mentioned earlier, the knife-edge resolution obtained with the polyethylene proton recoil converter was about 4 mm, so that little spatial resolution was lost by storing fast neutron radiographs as 64 × 64 image matrices. Figure 40 shows an example of such a radiograph.

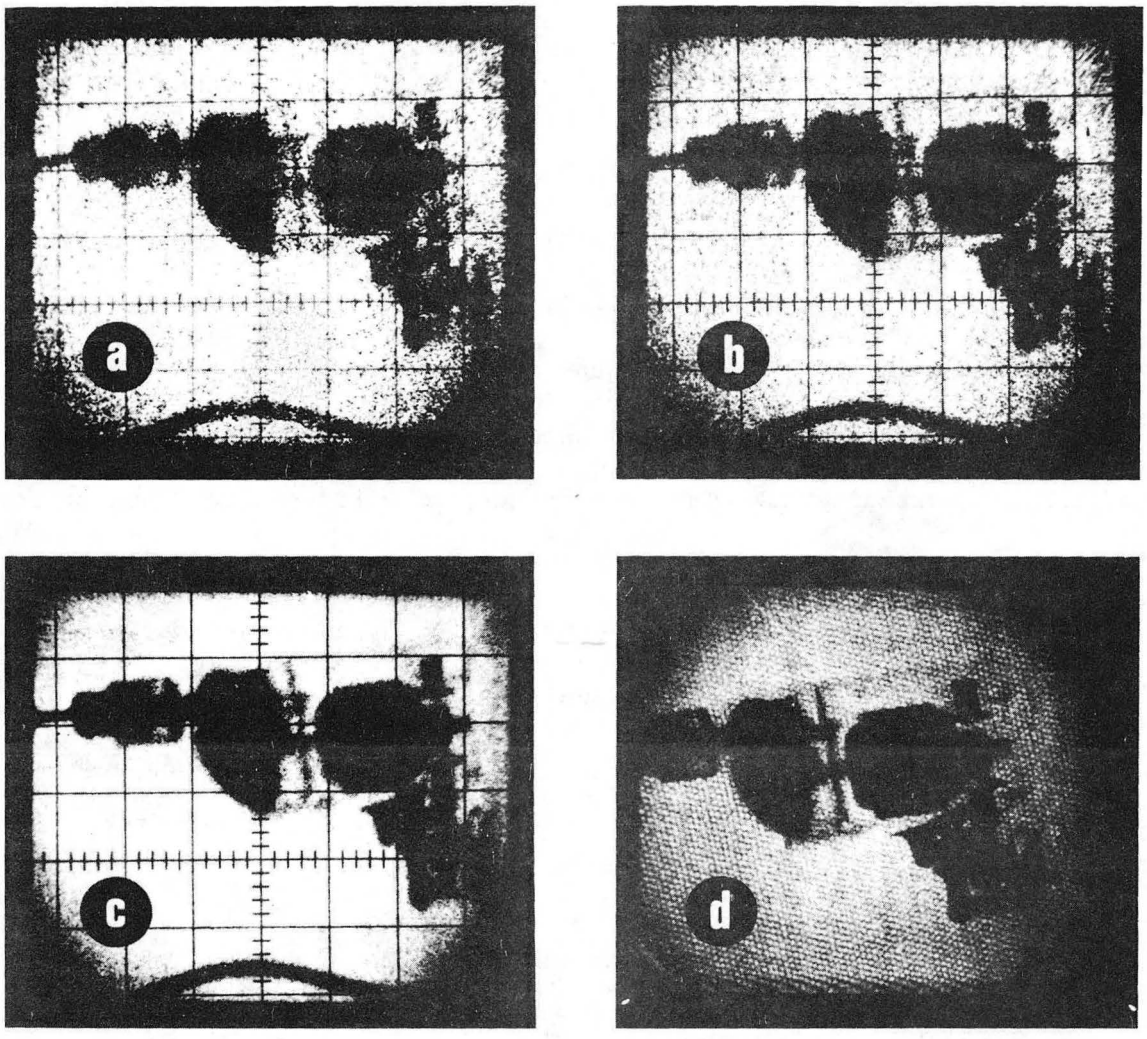

XBB-7311-6611

Fig. 39. Radiographs of drill taken at different interaction densities. (a) 5 mm^{-2}, (b) 10 mm^{-2}, (c) 60 mm^{-2}, (d) 40 mm^{-2}.

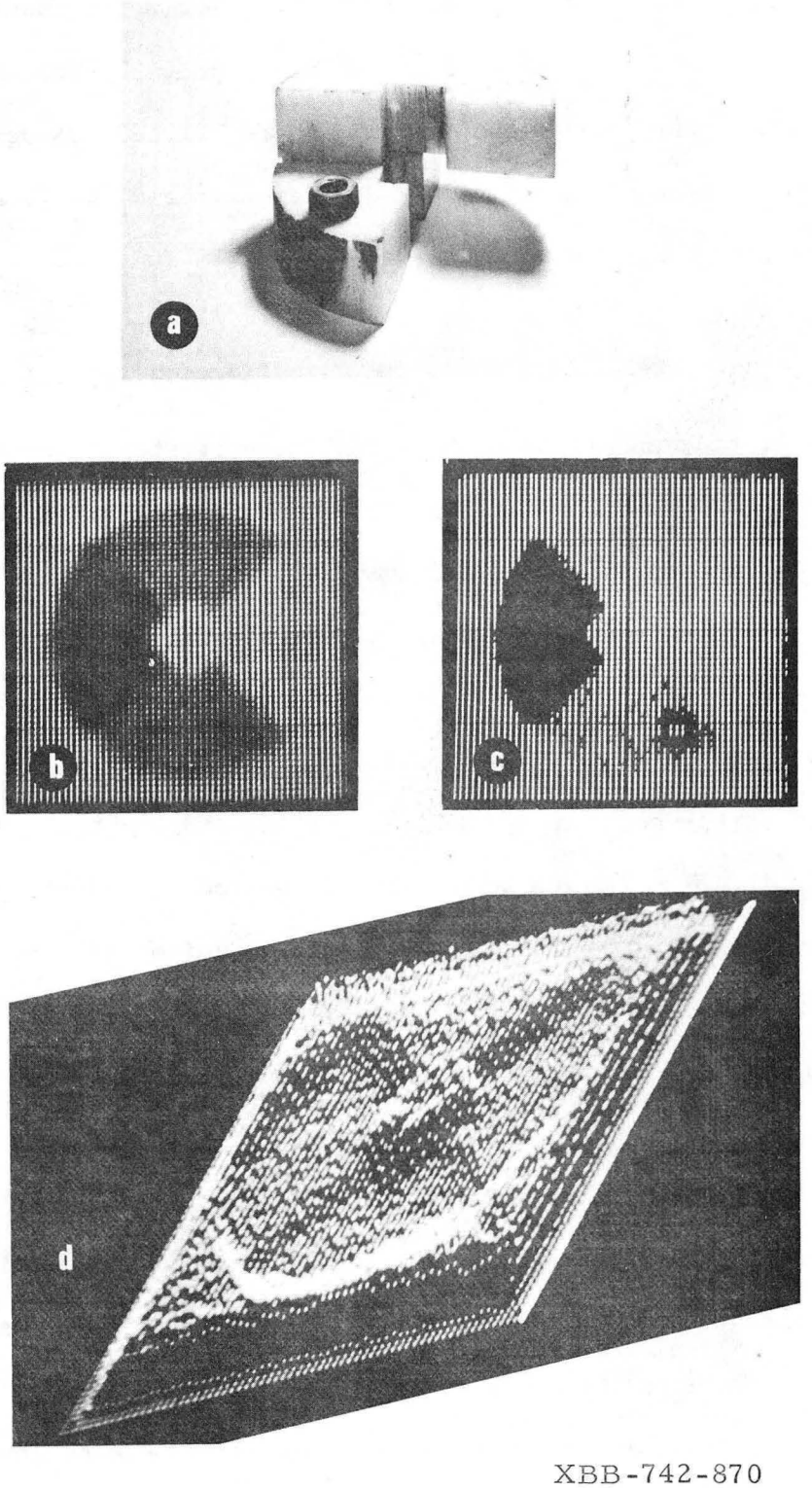

XBB-742-870

Fig. 40. (a) Test object used for fast neutron imaging, (b) and (c) fast neutron digital radiographs of test object, (d) isometric display of memory contents.

Figure 40a is a photograph of the test object which consisted of two semicircular shaped pieces of 2-inch-thick polyethylene and a steel nut, 1-1/8 inches across the flats. Images (b) and (c) were obtained using the digital photographic display unit and (d) is an isometric display of the memory contents (a built-in function of the memory unit). Figure 40d is rotated 90° CCW with respect to (b) and (c) and the polyethylene attenuator is represented by the depressed area which is made up of channels with smaller numbers of stored events. Image (b) is a photographic version of the same information displayed in (d); that is, the 64 contours were evenly distributed between zero and the level defining unattenuated areas. It therefore shows essentially the same information that would be contained in a direct CRT image. In (c), the bias and gain controls were adjusted to restrict the contours to attenuation levels containing the image of the steel nut which is barely visible in (b). The extension of this method to radiographs of more complicated structures is straightforward. Subject only to the image statistics, radiographic details lying at any attenuation level can be picked out and imaged with up to 100% contrast.

2. Off-Line (7600) Image Processing

For thermal neutron imaging, a problem was encountered with the use of the antiscatter grid. The parallel channels of the grid attenuated the divergent reactor beam more heavily as the distance from the beam axis increased so that levels of constant attenuation were no longer represented by contours of the stored image matrix. While the problem is

easily corrected through channel-by-channel normalization of the image matrix, the correction cannot be performed by a simple PHA. This task was accomplished by transferring the data to a large computer (CDC 7600) for arithmetic manipulation.

Two examples of digital thermal neutron radiographs are shown in Fig. 41. In order to take advantage of the better resolution obtained from the (n,α) conversion process, the image data was collected as four separate 64 × 64 matrices (and four more normalizing matrices). Each element of the resulting 128 × 128 matrix therefore corresponds to an image area approximately 2 mm square. After normalization, the contents of each matrix element is a number between 0 and 1.0 which represents the fractional transmission at the corresponding area in the image. Figure 41a was produced by distributing 32 gray shades evenly between 0 and 1.0 and (b) was produced by distributing the 32 shades evenly between 0.1 and 0.9. The choice of limits in the latter case results in background subtraction and contrast enhancement for small attenuations which makes the outline of the aluminum case much more evident.

After the image data is reduced to a normalized matrix, the visual display can be tailored to suit the situation. As in Fig. 40c, small differences in attenuation can be expanded over the entire range of contrast. In addition, the arithmetic capability of the computer allows for adjustment of the functional relationship between attenuation and image contrast. For example, individual elements of the matrix can be squared, exponentiated, or logged to accent particular features of the image.

The exposure or interaction densities which are necessary to produce digital images such as Fig. 41a are subject to a fairly clearcut criterion.

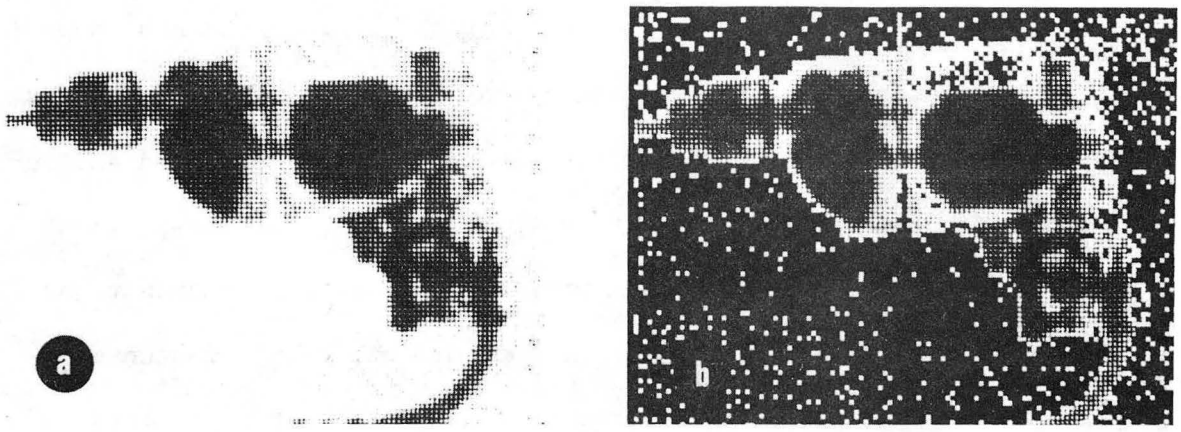

XBB-7311-6612

Fig. 41. Digital, computer processed thermal neutron radiographs of drill.

Under ideal circumstances, the human eye is capable of recognizing a minimum luminance contrast of about 1%.[73] However, many factors can reduce the eye's ability to perceive contrast differences and 30 to 50 gray shades are generally sufficient to produce adequate, continuous tone radiographs. Since each resolution element of a digital radiograph is imaged with a single shade, it is only necessary that enough counts be collected from each element to define the proper shade within a reasonable error. Thus, if N shades are used to image the data and the standard error is chosen, then a minimum of N^2 counts should be collected in the most exposed resolution element. This results in minimum probabilities of 38% that a resolution element will be imaged with the proper shade and 87% that it will be imaged within one shade of the proper shade. The statistics of Fig. 41a conform approximately to this criterion. Since the finite resolution of a detector effectively divides the image into resolution elements whether or not the image is digitized, the above considerations also apply to undigitized images for informational purposes.

A common application of radiography is the location of small cavities or foreign inclusions in otherwise homogeneous material. The measure of a system's ability to image such details is known as contrast sensitivity. For conventional photographic radiography, the contrast sensitivity depends on the smallest change in specimen thickness that will produce a detectable density change on the film which can be shown to be equal to

$$\Delta D_{min} = \frac{G\Sigma\Delta x_{min}}{\ln(10)} \quad \text{or} \quad \Delta x_{min} = \frac{\Delta D_{min}}{0.43G\Sigma} \tag{40}$$

where Σ is the attenuation coefficient of the material and G is the slope of the characteristic curve of the film.[74]

For a digital radiographic system, the contrast sensitivity is mainly a function of the counting statistics. The analog of Eq. (40) for a single channel of a digital system is $\Delta N_{min} = N\Sigma\Delta x_{min}$ or $x_{min} = \frac{\Delta N_{min}}{N\Sigma}$ where N is the average number of counts/channel around the inclusion. When the statistical uncertainty in ΔN_{min} is included explicitly, the expression for Δx_{min} becomes

$$\Delta x_{min} = \frac{\Delta N_{min} \pm \sqrt{N}}{N\Sigma} = \frac{\Delta N_{min}}{N\Sigma} \pm \frac{1}{\sqrt{N}\Sigma} \quad . \tag{41}$$

Generally it is desirable that the magnitude of the statistical error in the quantity, Δx_{min}, be no larger than the quantity itself. Thus, a practical criterion for choosing N is $\Delta x_{min} \geqslant \frac{1}{\sqrt{N}\,\Sigma}$ which alternately serves to establish the minimum thickness change which can be determined for a given N. According to Eq. (41), Δx_{min} can be made as small as desired with any desired accuracy by proper choice of N. In practice, Δx_{min} would be subject to limits set by background (such as the scattered component of the incident beam).

Figure 42a is a photograph of a test object used with the MWPC to make a contrast sensitivity measurement. It consists of 50-μm-thick mylar letters on a 0.016-inch-thick aluminum backing. In our reactor beam the attenuation coefficient of mylar was measured to be 2.8 + 0.3 cm^{-1}. Substitution of this value for Σ along with typical values for ΔD_{min} and G of 0.015 and 4 respectively[74] into Eq. (40) yields Δx_{min} = 31 μm for the photographic method. Thus the letters would be slightly better than barely detectable in a film radiograph.

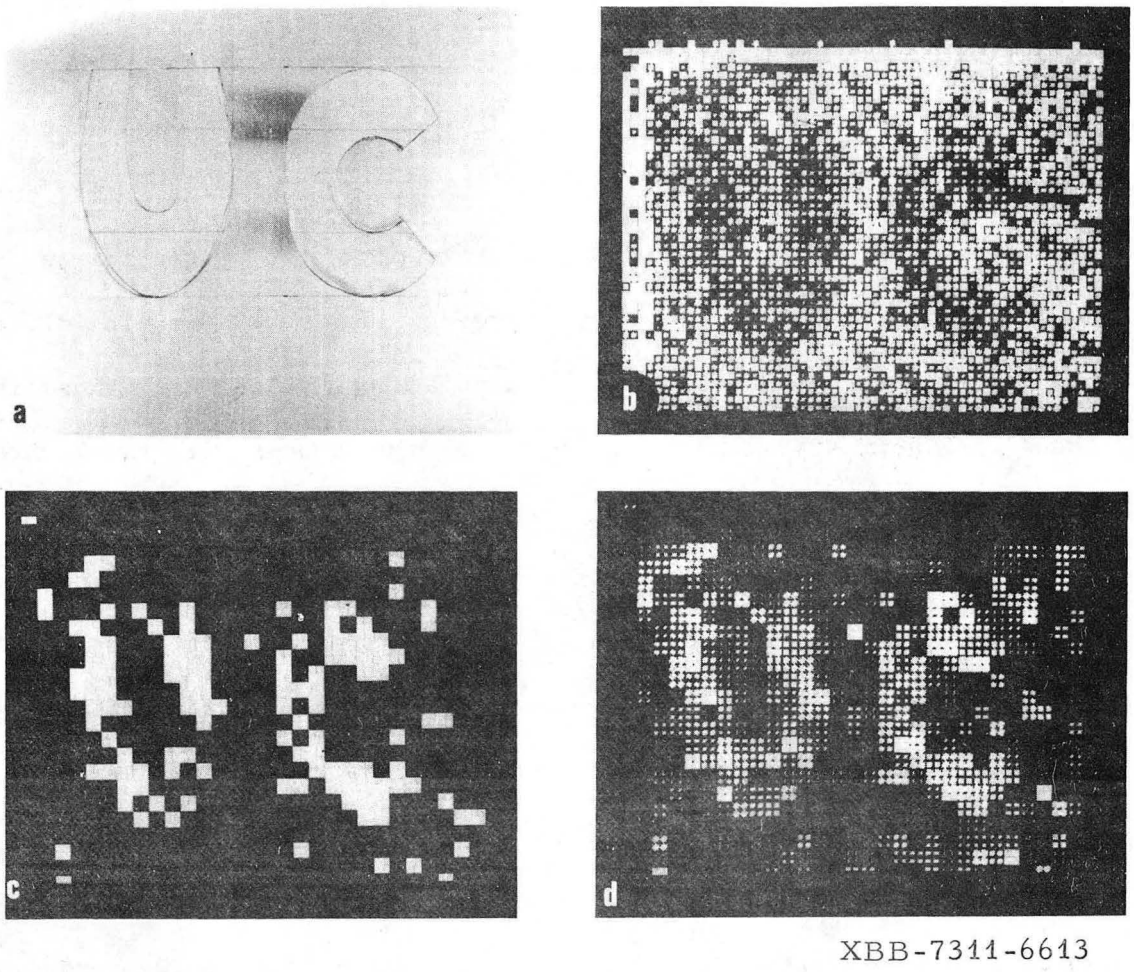

XBB-7311-6613

Fig. 42. (a) Test object used for contrast sensitivity measurement. (b), (c), and (d) Digital, computer processed thermal neutron radiographs of test object.

The three digital radiographs shown in Figs. 42b through 42d were obtained from a 64 × 64 normalized image matrix. The standard error for an individual element was about 3% (approximately the same as the percent attenuation provided by the mylar). In (b), the matrix was imaged by distributing 32 gray shades between 0.945 and 1.030. For image (c), the elements were averaged in groups of four to improve the statistics and then elements lying below 0.980 were imaged at 100% contrast. In (d), a normal distribution (centered at 0.970 with a σ of 0.015) was divided into 32 equal area segments which are shown in 32 gray shades with the lightest shade corresponding to the center of the distribution. Figure 42c is probably the best demonstration of digital contrast sensitivity since by simply improving the counting statistics, the missing resolution elements can be filled in. Further improvements of the statistics would allow the size of the resolution element to be decreased and would allow thinner specimens to be imaged with comparable contrast.

Since the method used to produce the foregoing digital images involved a time consuming data transfer (from paper tape to IBM cards), it is not practical for routine radiography, but it still serves to demonstrate the capability of the MWPC as a digital imaging device. This difficulty could be eliminated by the addition of a small on-line computer to the system in which case the visual images would be available for inspection almost immediately following the exposure.

For biological applications, or for radiation safety, the radiation dose to the subject due to the neutron exposure is an important consideration. At the present thermal neutron detection efficiencies that have been achieved, the dose at the detector is already quite small. For

the radiographs of the electric drill shown in Fig. 39, the doses ranged from 20 to 240 μrem. For the fast neutron radiographs shown in Fig. 40, the dose was about 230 mrem corresponding to an interaction density of about 17 mm^{-2} at a detection efficiency of 0.03% (the high energy threshold was reduced to improve resolution). However, because of the relatively large size of the resolution element and the extreme simplicity of the subject, approximately the same information could have been obtained from an exposure of 100 mrem.

As the thickness of the subject increases and the incident beam is more heavily attenuated, the dose to the subject must be increased to maintain the directly transmitted fluence at the detector. Table VII shows the dose to various thicknesses of Lucite which result in a directly transmitted fluence of 1000 neutrons/mm^2 for the thermal reactor spectrum, the epithermal reactor spectrum, and the Pu-Be source spectrum.

The futility of attempting to image thick organic specimens with thermal neutrons is evident from Table VII. Even if the indicated dose for a 5 cm thickness were acceptable, the high background due to the scattered component would make imaging of the directly transmitted beam almost impossible. Since the ratio of the scattered intensity to the directly transmitted intensity increases approximately logarithmically[74] with subject thickness, the problem is compounded for larger thicknesses. The greater penetration provided by epithermal and fast neutrons results in much lower doses for thicker subjects at the expense of reduced material contrast.

For purposes of computing the dose received by the subject in acquiring an image with a given interaction density, the efficiency of the

Table VII*

Lucite Thickness (cm)	Dose to subject for directly transmitted fluence of 1000 neutrons/mm^2 (mrem)		
	Thermal (λ = 0.30 cm^{-1})	Epithermal (λ = 0.65 cm^{-1})	Pu-Be (λ = 5.8 cm^{-1})
0.0	0.104	0.104	4.08
0.1	0.145	1.121	4.15
1	2.86	0.480	4.84
2	78.8	2.22	5.75
5	1.64×10^6	218	9.61
10	2.59×10^{13}	4.59×10^5	22.6
25	1.02×10^{35}	4.25×10^{15}	295

*Neutron dose data taken from Ref. 75.

image detector must also be considered. For instance, the detection efficiencies achieved with the MWPC for thermal, epithermal, and fast neutron energy spectra were approximately 0.035, 0.0055 (scaled from 0.025 eV to 1 eV as 1/v), and 0.001 respectively. For a given interaction density, these efficiencies result in approximately equal thermal and epithermal doses to a Lucite thickness of 1.0 cm and equal epithermal and fast doses to a Lucite thickness of 3.9 cm.

VII. CONCLUSIONS

The neutron sensitive MWPC provides radiographic capability that is not otherwise available in the family of more conventional neutron radiographic image detectors. Its major attributes include extreme sensitivity and its ability to provide coordinate information that is easily digitized for computer storage and manipulation. For the radiographic inspection of large objects where spatial resolution requirements can often be relaxed, the reciprocal relationship between the size of the resolution element and the necessary interaction density allows the exposures and source strengths to be reduced accordingly.

The resolving capabilities of the MWPC and two conventional image detectors are compared in Fig. 43. NE 421 is a mixture of ^{6}LiF, ZnS, and a plastic binder (1:2:1 by weight) and is representative of the class of neutron-sensitive scintillators. The MTF for the MWPC is repeated from Fig. 32. The superior resolution of gadolinium makes it irreplaceable for extremely high resolution applications. However, the resolving power of the scintillator is seen to exceed that obtained from the MWPC by less than a factor of four. The use of pressurized, higher density filling gases to shorten the charged particle track lengths will improve the resolution in one dimension, but for two-dimensional imaging there is not much point in exceeding the resolution set by the anode wire spacing. While present construction techniques make 1 mm anode spacings practical, it becomes increasingly difficult to maintain the necessary tolerances for finer spacings. Thus the MWPC resolution indicated in Fig. 43 can probably be increased by a factor of two without too much difficulty.

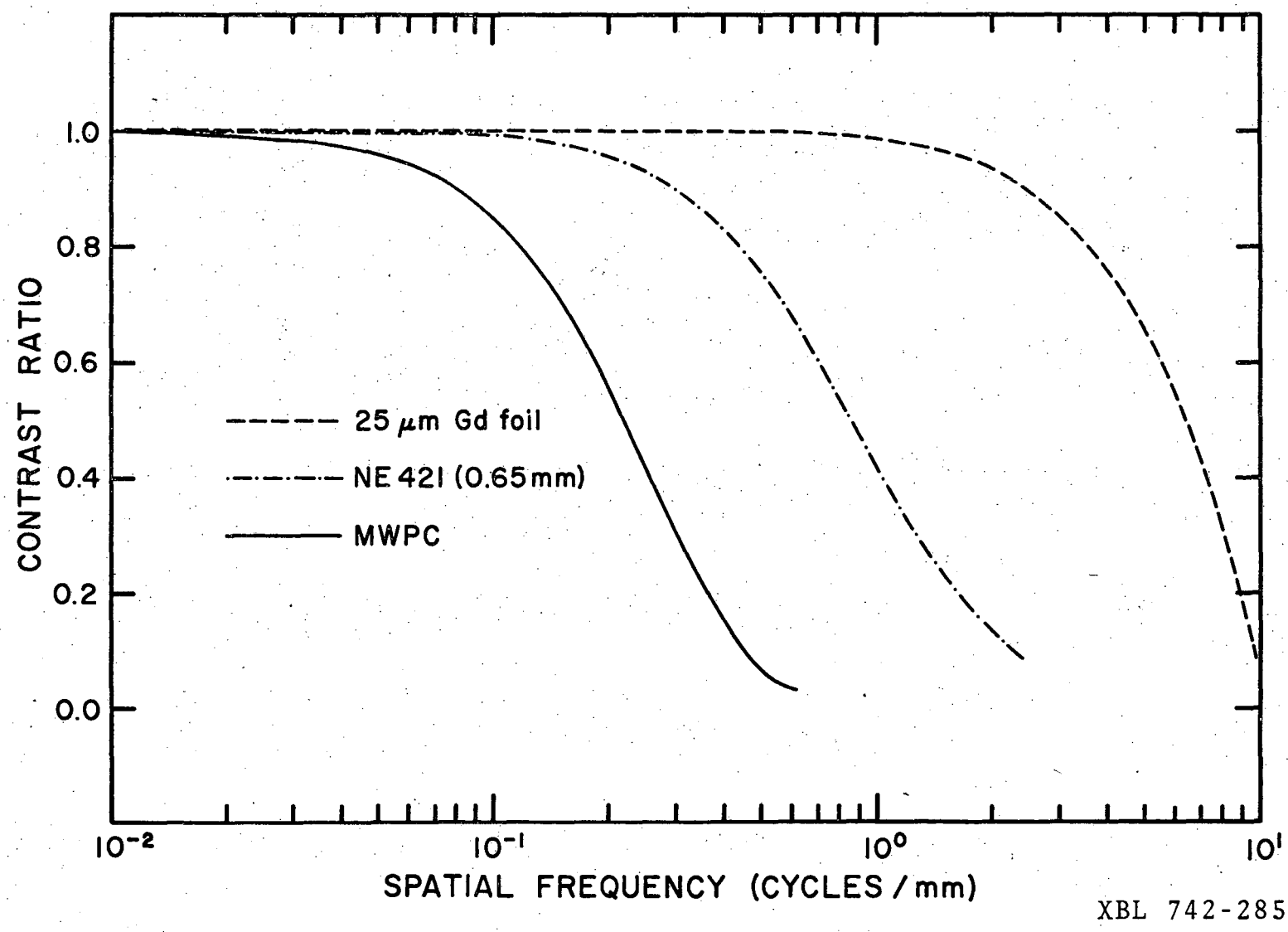

XBL 742-285

Fig. 43. Comparison of the resolving powers of the neutron sensitive MWPC, NE 421, and Gd metal.

The speed of an image detector is generally inversely related to its resolving power so that high resolution images are obtained at the expense of higher neutron fluences. The exposures which are necessary to produce a density change of 1.5 on photographic film are listed in Table VIII. The exposure listed for the MWPC will image ten shades in a 2mm square according to the criterion set forth in Sec. VI-B.

Table VIII*

Image Detector	Exposure (thermal neutrons/cm^2)	film
Gd (25 μm)	2×10^8	Kodak Type AA (x-ray film)
NE 421 (0.65 mm)	2×10^6	Kodak Tri-X (light sensitive film)
MWPC	2×10^5	----

*Exposure data for NE 421 and Gd metal from Ref. 4, p. 62.

As in the case of the spatial resolution, the speed or detection efficiency of the MWPC is also subject to improvement. Increases of 20 to 30% should be realizable with more uniform converter coatings. Also, the use of more sensitive electronics capable of accurately timing low amplitude pulses would increase both the detection efficiency and the spatial resolution.

Much larger increases in the detection efficiency might be realized with the application of layered, honeycomb converters similar to those recently developed for increasing γ-detection efficiency in the MWPC.[76]

In place of the lead γ-to-electron converter coating, the honeycomb would be coated with ^{10}B for slow neutron detection or a hydrogenous material for fast neutron detection. The surface area for the conversion reaction can be increased manyfold in this manner. Conducting strips are incorporated in the design of the honeycomb so axial electric fields can be established to drift electrons from the cells into the sensitive volume of the chamber. It is difficult to predict to what extent the thermal neutron detection efficiency can be increased in this manner but a value as high as 15 or 20% does not seem too unrealistic.

Appendix A. INDUCED CATHODE PULSES AND DELAY LINE INTERPOLATION

In the early stages of induced pulse formation the total charge in the ion sheath is confined to a small volume about the anode wire, and at a distant point on one of the cathode planes the sheath appears as a point charge. From electrostatics[77] the induced charge density on an infinite plane due to a point charge, Q', situated a distance, L, from the plane is

$$\rho = \frac{Q'L}{2\pi r^3} = \frac{Q'}{2\pi(L^2 + x^2 + z^2)^{3/2}} \text{ coulomb/cm}^2 \qquad (42)$$

where r is the distance from the point in the plane to the charge (see Fig. 44). The induced charge density on long strips can be obtained by integrating with respect to z.

$$\int_{-\infty}^{\infty} \frac{Q'Ldz}{2\pi(L^2 + x^2 + z^2)^{3/2}} = \frac{Q'}{\pi L(1 + x^2/L^2)} = \frac{Q'}{\pi L} f(x/L) \text{ coulomb/cm} \quad . \qquad (43)$$

The function f(x/L) is shown in Fig. 45. Note that for distances as large as 3L away from the avalanche, the charge density has only dropped to 10% of its peak value. The charge induced on a long finite width strip with edges at x_1 and x_2 is obtained by integrating the charge density across the strip, or

$$Q'(x_1,x_2) = \int_{x_1}^{x_2} \frac{Q'dx}{\pi L(1 + x^2/L^2)} = \frac{Q'}{\pi} [\tan^{-1}(x_2/L) - \tan^{-1}(x_1/L)] \quad . \qquad (44)$$

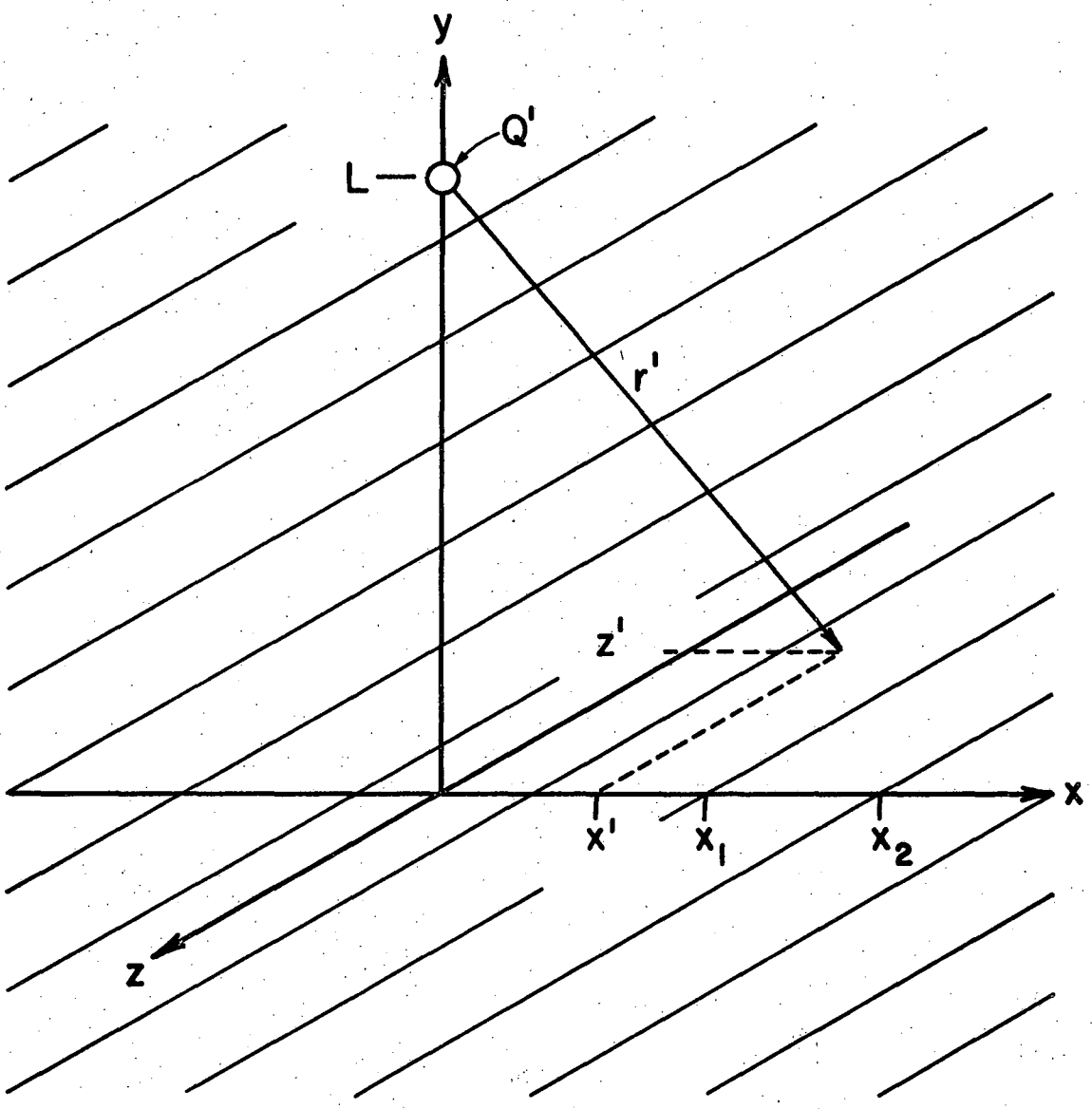

Fig. 44. Geometry for calculating the induced cathode charge distribution.

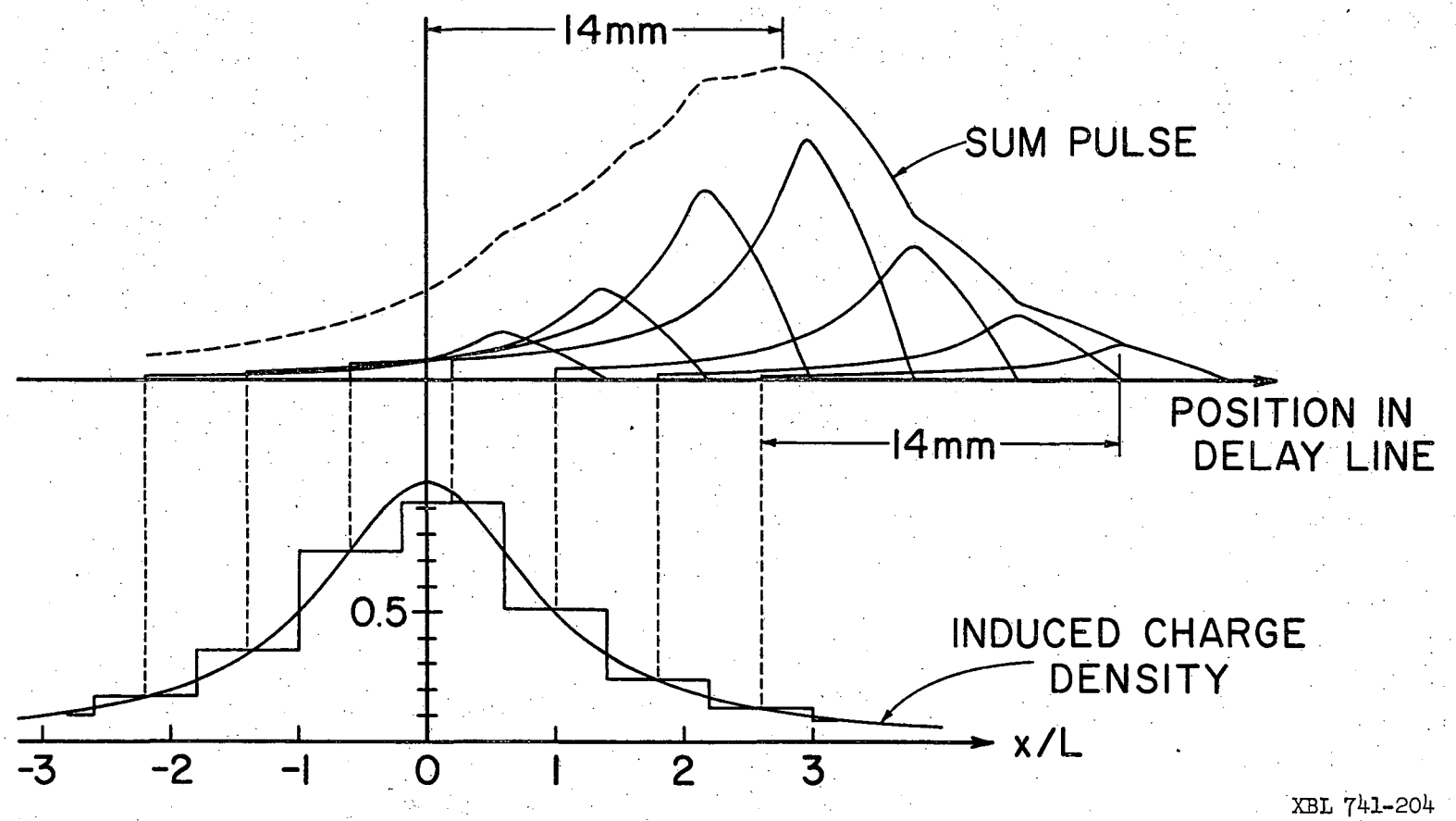

Fig. 45. Induced cathode charge distribution and addition of pulses in delay line.

The relative charges induced on strips of width 0.8L are shown as the histogram superposed on f(x/L) in Fig. 45. As long as the radius of the ion sheath is small, the point charge assumption will be valid. Thus, the relative shape of the charge distribution, f(x/L), should remain constant during fast pulse formation. The time development of induced cathode pulses must therefore follow that derived for the induced anode pulse (Eq. (17)).

Figure 45 also shows the cathode pulses being coupled into a delay line. Here it is assumed that the pulses are coupled into discrete points in the line corresponding to the centers of the cathode strips. It has further been assumed that L = 5 mm and the delay line position-to-time conversion ratio was taken as 12.5 nsec/mm. The situation is depicted 225 nsec after the avalanche and the peaks of the pulses have already traveled 14 mm down the line. Note that a set of mirror image pulses would be propagating to the left and eventually will be dissipated in the termination resistor. The actual shape of the pulse in the line is just the algebraic sum of the pulses coupled from each cathode strip. The peak of the sum-pulse is seen to be 14 mm down line from the actual position of the avalanche, so by using zero-cross timing it is possible to interpolate between cathode strips for the real event position.

The ripple of the sum-pulse would not be present on an actual delay line pulse primarily because the pulses are coupled into a finite width of the delay line rather than at a point. In addition, amplitude distortion would heavily attenuate the high frequencies which constitute the ripple.

Appendix B. SCHEMATIC DIAGRAMS OF FIDUCIAL MARK GENERATOR AND DIGITAL PHOTOGRAPHIC DISPLAY UNIT

This appendix contains the schematics for the two units which were developed specifically as part of this project. The timing SCA and timing discriminators are documented in LBL drawings 22X2153-S1A, 22X2223 L-1, and 22X2153 L-1A and the amplifiers are documented in LBL drawing 22X2161-P1.

In the following diagrams, component numbers beginning with 74 refer to members of the 7400 series of TTL medium speed logic.

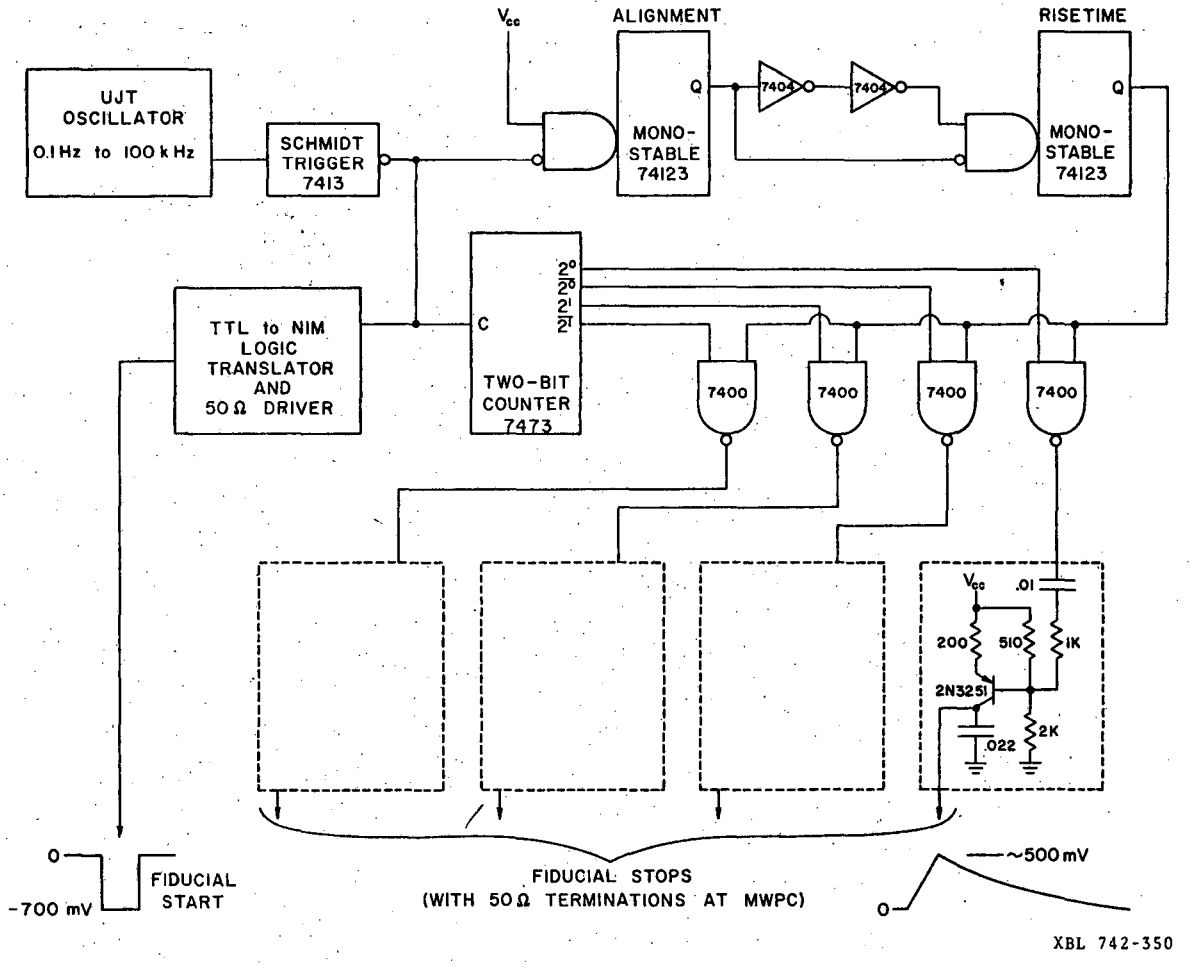

Fig. 46. Schematic diagram of fiducial mark generator.

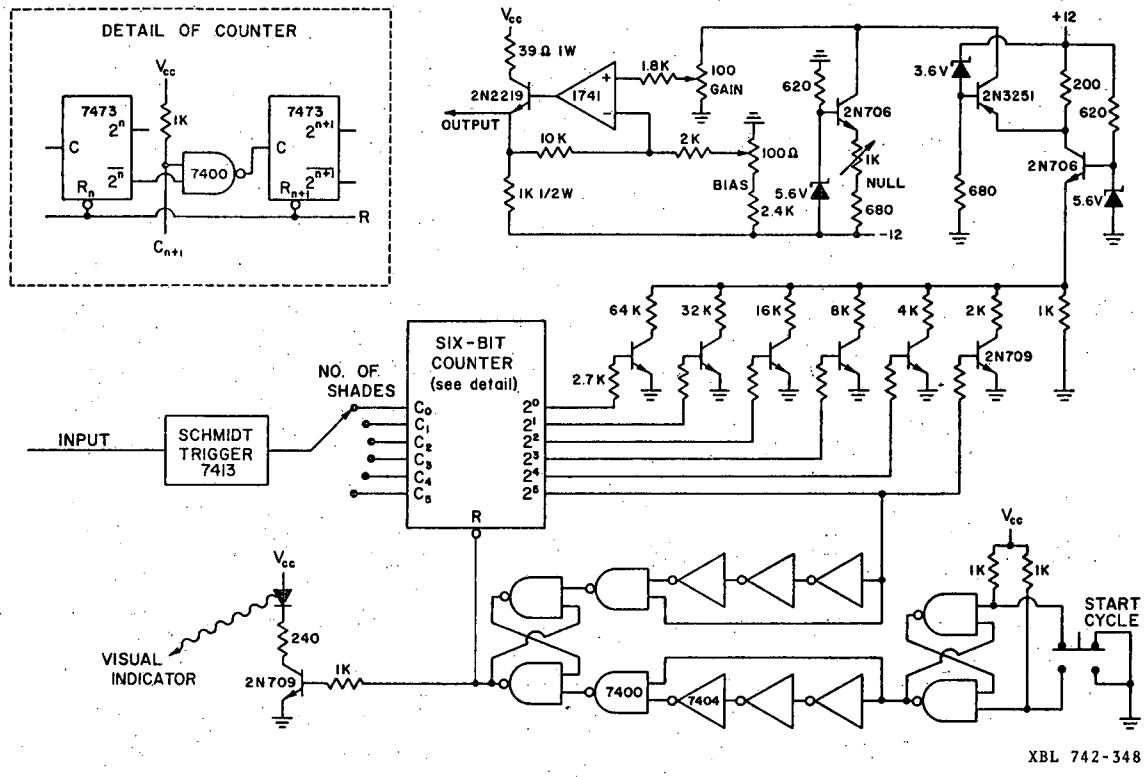

Fig. 47. Schematic diagram of digital photographic display unit.

Appendix C. DETAILS OF MTF CALCULATIONS

Any function, f(x), which is piecewise differentiable in the interval, $-\frac{1}{2}L \leq x \leq \frac{1}{2}L$, can be expressed as an infinite sum of sinusoids known as an exponential Fourier series,[78] i.e.,

$$f(x) = \tfrac{1}{2} \sum_{n=-\infty}^{\infty} f_n \exp(2\pi i \nu_n x) \tag{45}$$

where

$$f_n = \frac{2}{L} \int_{-\frac{1}{2}L}^{\frac{1}{2}L} f(x) \exp(-2\pi i \nu_n x) dx \tag{46}$$

and $\nu_n = n\nu = \frac{n}{L}$; f_n is the amplitude of the n^{th} harmonic. If the function is symmetric about x = 0, then Eq. (45) and Eq. (46) respectively become

$$f(x) = \sum_{n=0}^{\infty} f_n \cos(2\pi \nu_n x) \tag{47}$$

and

$$f_n = \frac{2}{L} \int_{-\frac{1}{2}L}^{\frac{1}{2}L} f(x) \cos(2\pi \nu_n x) dx \quad . \tag{48}$$

For the asymmetric square wave object function shown in Fig. 48a, Eq. (48) becomes

$$O_n = \frac{2}{L} \int_{-\frac{1}{2}}^{\frac{1}{2}L} O(x) \cos(2\pi \nu_n x) dx = \frac{4}{L} \left(\int_{0}^{\frac{1}{2}c} T_2 \cos(2\pi \nu_n x) dx + \int_{\frac{1}{2}c}^{\frac{1}{2}L} T_1 \cos(2\pi \nu_n x) dx \right)$$

$$\rightarrow O_n = \frac{2}{n\pi}(T_2 - T_1) \sin(\pi \nu_n c) \tag{49}$$

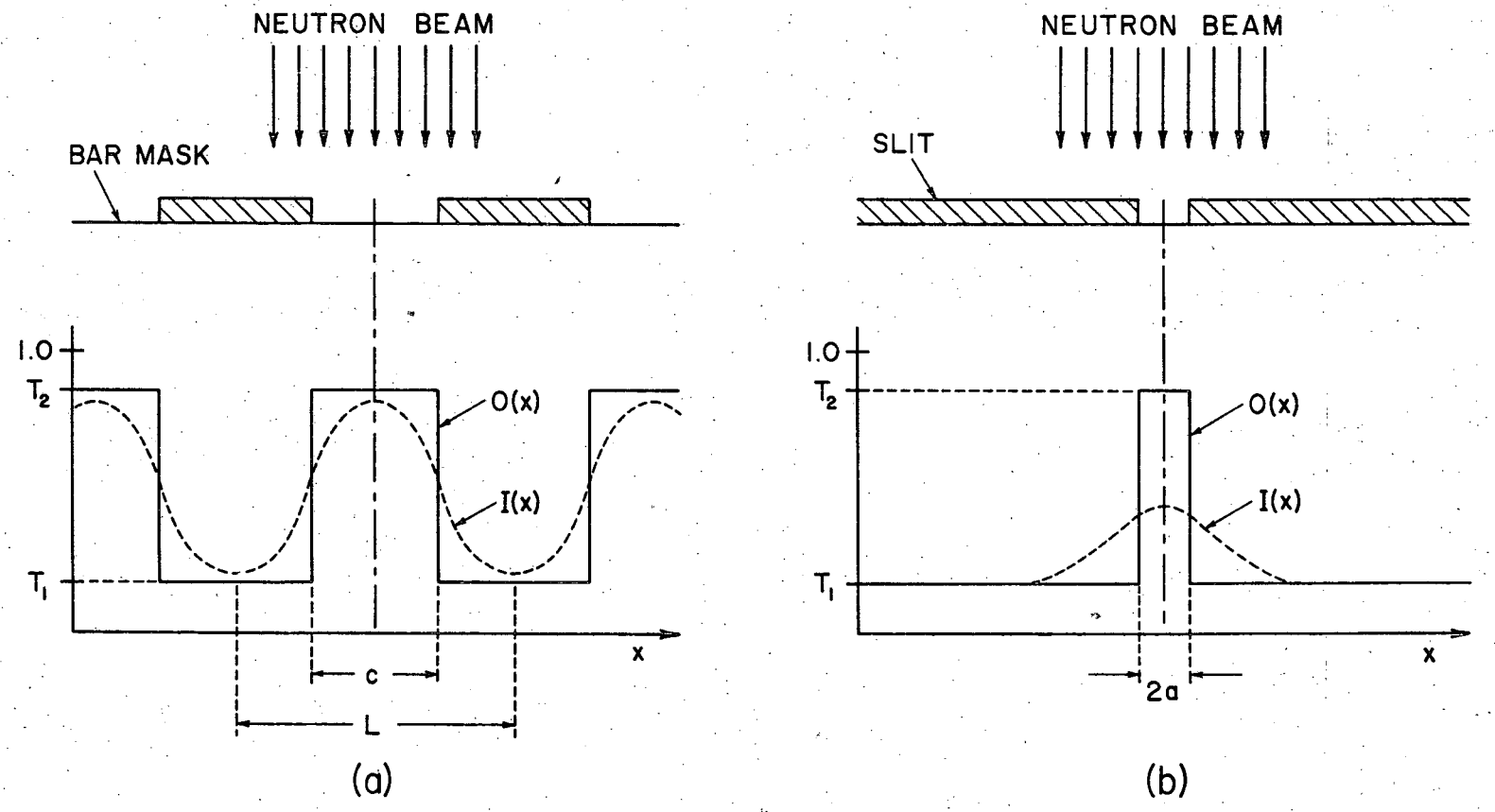

XBL 742-257

Fig. 48. Calculation of MTF's from experimental data using (a) periodic bar masks and (b) a slit line source.

where T_1 and T_2 are the fractional transmission of the spaces and bars of the mask. Defining the degree of asymmetry as $\delta = \frac{1}{2} - c/L$ so that $c = L(\frac{1}{2} - \delta)$, Eq. (49) becomes

$$O_n = \frac{2}{n\pi}(T_2 - T_1)\sin\left(\frac{n\pi}{2} - n\pi\delta\right) = \begin{cases} \frac{2}{n\pi}(T_2 - T_1)(-1)^{\frac{1}{2}(n-1)}\cos(n\pi\delta) & \text{for odd } n \\ \frac{2}{n\pi}(T_2 - T_1)(-1)^{\frac{1}{2}(n-2)}\sin(n\pi\delta) & \text{for even } n>0 \end{cases} \tag{50}$$

where use has been made of the trigonometric relation for the sum of two angles. The masks are designed to be symmetrical and δ can usually be kept below 0.1 so that even harmonic amplitudes are much lower than odd harmonic amplitudes. In the remainder of this derivation, n denotes an odd integer. The image function, I(x), which is the system's response to the input, O(x), can be expressed as a similar series. Applying Eq. (48) to I(x) yields

$$I_n = \frac{2}{L}\int_{-\frac{1}{2}L}^{\frac{1}{2}L} I(x)\cos(2\pi\nu_n x)dx \quad . \tag{51}$$

Since the function, I(x), is obtained from channel-by-channel normalization of PHA data resulting in the ordered set $\{I_k\}$, Eq. (51) is recast in the form of a finite sum,

$$I_n = \frac{2}{L}\sum_{k=1}^{L/\Delta x} I_k\cos(2\pi\nu_n k\Delta x)\Delta x \tag{52}$$

where Δx is the spatial width corresponding to one channel of the PHA and $k = 1$ corresponds to a channel containing either a minimum or a maximum of the image function.

By definition, the value of the MTF at a spatial frequency, ν_n, is the ratio of sinusoidal modulation of frequency, ν_n, which is transferred from the system's input to its output, or

$$MTF(\nu_n) = \frac{I_n(\nu)}{O_n(\nu)} = n\pi\nu\Delta x \frac{\sum_{k=1}^{1/\nu\Delta x} I_k \cos(2\pi\nu_n k\Delta x)}{(T_2 - T_1)(-1)^{\frac{1}{2}(n-1)}\cos(n\pi\delta)} \quad . \tag{53}$$

Generally a separate test plate is prepared for each frequency at which a measurement is desired so only the first harmonics are involved in the MTF calculation and Eq. (53) becomes

$$MTF(\nu) = \frac{I_1}{O_1} = \pi\nu\Delta x \frac{\sum_{k=1}^{1/\nu\Delta x} I_k \cos(2\pi\nu k\Delta x)}{(T_2 - T_1)\cos(\pi\delta)} \quad . \tag{54}$$

In principle, the symmetry of I(x) allows the range of integration in Eq. (51) to be halved. However, the statistical nature of the experimentally obtained I(x) makes it advantageous to retain the full range, or even to extend the range to include several complete cycles. In this case, Eq. (54) becomes

$$MTF(\nu) = \frac{\pi\nu\Delta x}{N} \frac{\sum_{k=1}^{N/\nu\Delta x} I_k \cos(2\pi\nu k\Delta x)}{(T_2 - T_1)\cos(\pi\delta)} \tag{55}$$

where N is the number of complete cycles included in the summation.

The continuous Fourier transform can also be applied to the calculation of the MTF. Any function, $f(x)$, which is piecewise differentiable in the interval, $-\infty < x < \infty$, and for which the integral,

$$\int_{-\infty}^{\infty} |f(x)|dx \quad ,$$

exists, is represented by[79]

$$f(x) = \int_{-\infty}^{\infty} \bar{f}(\nu)\exp(2\pi i\nu x)d\nu \tag{56}$$

where

$$\bar{f}(\nu) = \int_{-\infty}^{\infty} f(x)\exp(-2\pi i\nu x)dx \quad . \tag{57}$$

As in the case for the finite transform, the expressions simplify for functions which are symmetric about $x = 0$ to

$$f(x) = \int_{-\infty}^{\infty} \bar{f}(\nu)\cos(2\pi\nu x)d\nu \tag{58}$$

and

$$\bar{f}(\nu) = \int_{-\infty}^{\infty} f(x)\cos(2\pi\nu x)dx \quad . \tag{59}$$

Equation (59) is the continuous analog of Eq. (47) with $\bar{f}(\nu)$ being the spatial frequency spectrum of $f(x)$. Note that $\bar{f}(\nu)$ is defined for all

values of ν rather than just at the discrete values, ν_n. Applying Eq. (59) to the object and image functions yields

$$\bar{O}(\nu) = \int_{-\infty}^{\infty} O(x)\cos(2\pi\nu x)\,dx \tag{60}$$

and

$$\bar{I}(\nu) = \int_{-\infty}^{\infty} I(x)\cos(2\pi\nu x)\,dx \quad . \tag{61}$$

The MTF follows directly from its definition,

$$MTF(\nu) = \frac{\bar{I}(\nu)}{\bar{O}(\nu)} = \frac{\int_{-\infty}^{\infty} I(x)\cos(2\pi\nu x)\,dx}{\int_{-\infty}^{\infty} O(x)\cos(2\pi\nu x)\,dx} \quad . \tag{62}$$

Since the applicability of Eq. (62) is not restricted to cyclic functions with a finite period, patterns used to modulate the beam do not have to be repeated. A particularly simple case results when a single narrow slit is used (see Fig. 48b). For a slit of width 2a, such that $O(x) = \begin{cases} T_2 \text{ for } -a \leq x \leq a \\ T_1 \text{ otherwise} \end{cases}$, it follows that

$$\bar{O}(\nu) = 2\left(\int_0^a T_2\cos(2\pi\nu x)\,dx + \int_a^{\infty} T_1\cos(2\pi\nu x)\,dx\right) = \frac{(T_2 - T_1)\sin(2\pi\nu a)}{\pi\nu} \quad . \tag{63}$$

Note that $\lim_{a\to 0}[\bar{O}(\nu)] = 2a(T_2 - T_1)$ so that for an infinitely narrow slit (delta-source), all frequencies are present in the object function with

the same amplitude, $2a(T_2 - T_1)$. For the special case of the narrow slit, the resulting image function is called the Line Spread Function (LSF) so

$$MTF(\nu) = \frac{\pi\nu}{(T_2 - T_1)\sin(2\pi\nu a)} \int_{-\infty}^{\infty} LSF(x)\cos(2\pi\nu x)\,dx \qquad (64)$$

and

$$\lim_{a\to 0}[MTF(\nu)] = [2a(T_2 - T_1)]^{-1} \int_{-\infty}^{\infty} LSF(x)\cos(2\pi\nu x)\,dx \quad . \qquad (65)$$

For slits that are narrow compared to the FWHM of the LSF, the difference between Eq. (64) and Eq. (65) is small over the frequency range of interest.

Since the LSF is also obtained from normalized PHA data, the appropriate form for Eq. (64) is

$$MTF(\nu) = \frac{\pi\nu\Delta x}{(T_2 - T_1)\sin(2\pi\nu a)} \sum_{k=-k}^{K} LSF_k \cos(2\pi\nu k\Delta x) \qquad (66)$$

where k = 0 corresponds to the symmetry axis of the LSF and K is large enough to include the tails of the LSF.

ACKNOWLEDGMENTS

Financial support for this work was derived from the U. S. Atomic Energy Commission through the Lawrence Berkeley Laboratory and through a three year fellowship administered by Oak Ridge Associated Universities as part of the "Special Fellowships in Nuclear Science and Engineering" program.

Many people contributed to the work represented by this thesis and I wish to express my appreciation to them all. Special thanks are extended to Prof. Selig Kaplan for his guidance and assistance in all phases of the degree program.

The cooperation of the UCB reactor staff, particularly Mr. Harry Braun and Mr. Tek Lim, is greatly appreciated as is the quick and accurate fabrication of experimental assemblies by Mr. Dan Winterbauer and Mr. John Souza. The assistance of Mr. Jerry Stoker with the chamber fabrication and assembly is also greatly appreciated. For completion of the final draft, credits go to Mr. Tim Daly for inking the illustrations and Mrs. Kathy McCracken for typing the text.

Finally, I wish to express my sincere gratitude to my wife, Diane, for continued moral support and for her assistance in literature searching.

REFERENCES

1. A. P. French, Principles of Modern Physics (John Wiley and Sons, Inc., New York, 1958).

2. H. Kallmann, Research 1, 254 (1948).

3. O. Peter, Z. Naturforsch. 1, 557 (1946).

4. H. Berger, Neutron Radiography (Elsevier Publishing Co., Amsterdam, 1965), p. 4.

5. J. Thewlis, Brit. J. App. Phys. 7, 345 (1956).

6. J. Thewlis and R. T. P. Derbyshire, Report AERE M/TN 37, U. K. Atomic Energy Research Establishment, Harwell, England, 1956.

7. H. V. Watts, ARF 1164-27, Category No. UC-23, Isotopes-Industrial Technology, TID-4500 (17^{th} Ed.).

8. H. Berger, Symposium on Physics and Nondestructive Testing, ANL-6346, 12, (October, 1960).

9. E. L. Criscuolo and D. Polansky, Missle and Rockets Symposium, U. S. Naval Ammunition Depot, Concord, California (April 18, 1961).

10. A. W. Schultz and W. Z. Leavitt, The Feasibility of Using Neutron Radiography as a Nondestructive Testing Technique, WAL TR 142/67 (December, 1961).

11. R. L. Tomlinson and P. E. Underhill, AGN TP-229, Nuclear Division, Aerojet General Corporation.

12. W. L. Whittemore, G. T. Schnurer, and A. T. McMain, Proceedings of the 17^{th} Conference on Remote Systems Technology (1969), p. 49.

13. D. J. Hughes and Robert B. Schwartz, Neutron Cross Sections, BNL 325, 2^{nd} Ed., 1958.

14. E. Segrè, Nuclei and Particles (W. A. Benjamin, Inc., New York, 1964), p. 244.

15. W. H. McMaster, N. Kerr Del Grande, J. H. Mallett, and J. H. Hubbell, UCRL-50174 Sec. II Rev. 1 (June 1969).

16. S. Kawasaki, Nucl. Instr. Methods 62, 311 (1968).

17. E. A. Warman, Iron Age 190, 72 (1962).

18. J. P. Barton and M. F. Klozar, Trans. Am. Nucl. Soc. 12, 465 (1969).

19. D. Polansky and E. Criscuolo, Fast Neutron Radiography, Neutron Radiography Session by the ASNT, Evanston, Illinois (1965).

20. E. Tochilin, Phys. Med. Biol. 10, 477 (1965).

21. J. P. Barton, Materials Evaluation 25, 45 (1967).

22. D. Strominger, et al., Rev. Mod. Phys. 30, No. 2 - Part II (April 1958).

23. O. Sala, et al., Phys. Rev. 74, 1249 (1948).

24. H. Berger, Neutron Radiography (Elsevier Publishing Co., Amsterdam, 1965), p. 60.

25. K. H. Sun, P. R. Malmberg, and F. A. Pacjak, Nucleonics 14, 46 (1956).

26. R. Stedman, Rev. Sci. Instr. 31, 1156 (1960).

27. J. Kastner, H. Berger, and I. Kraska, Nuclear Applications 2, 252 (1966).

28. A. R. Spowart, Non-Destructive Testing, 151 (February, 1968).

29. L. Reiffel, Rev. Sci. Instr. 29, 1151 (1958).

30. K. Cotterell, Applied Materials Res. 3, 103 (1964).

31. H. V. Watts, Report ANL-6515, Argonne National Laboratory, Argonne, Illinois 53-80 (1961).

32. S. Kaplan, L. Kaufman, V. Perez-Mendez, and K. Valentine, Nucl. Instr. Methods 106, 397 (1973).

33. L. Kaufman, V. Perez-Mendez, J. Sperinde, and G. Stoker, Am. J. Roentgenol., Radium Therapy Nucl. Med. 113, 378 (1970).

34. M. R. Hawkesworth, J. Phys. E: J. Sci. Instr. 2, 673 (1969).

35. G. A. Erskine, Electrostatic Problems in Multiwire Proportional Chambers, CERN report, Nucl. Instr. Methods 105, 565 (1972).

36. P. M. Morse and H. Feshbach, Methods of Theoretical Physics (McGraw-Hill, New York, 1953), p. 1236.

37. L. B. Loeb, The Kinetic Theory of Gases, 3rd Ed. (Dover Publications, Inc., 1927), p. 602-605.

38. W. J. Price, Nuclear Radiation Detection, 2nd Ed. (McGraw-Hill, Inc., New York, 1958).

39. T. E. Bortner, G. S. Hurst, and W. G. Stone, Rev. Sci. Instr. 28, 103 (1957).

40. L. B. Loeb, Basic Processes of Gaseous Electronics (University of California Press, Berkeley, 1955).

41. O. C. Allkofer, Spark Chambers (Verlag Karl Thiemig K. G., Munchen, 1969), p. 14.

42. M. E. Rose and S. A. Korff, Phys. Rev. 59, 850 (1941).

43. G. Charpak, Evaluation of the Automatic Spark Chambers, ed. by E. Segrè (George Banta Co., Inc., 1970), Ann. Rev. Nucl. Sci., Vol. 20, p. 195.

44. G. Charpak, D. Rahm, and H. Steiner, Nucl. Instr. Methods 80, 13 (1970).

45. G. Fischer and J. Plch, Nucl. Instr. Methods 100, 515 (1972).

46. D. Corson and P. Lorrain, Introduction to Electromagnetic Fields and Waves (W. H. Freeman and Co., San Francisco, 1962), p. 525.

47. H. Foeth, R. Hammerstrom, and C. Rubbia, Nucl. Instr. Methods 109, 521 (1973).

48. G. Charpak and F. Sauli, High Accuracy Two Dimensional Readout in Multiwire Proportional Chambers, CERN 73-4, Laboratory I, Nuclear Physics Division, February, 1973.

49. C. J. Borkowski and M. K. Kopp, Proceedings of the 13th Scintillation and Semiconductor Counter Symposium, Washington, D. C., March 1-3, 1972: IEEE Trans. Nucl. Sci., June, 1972.

50. R. Grove, K. Lee, V. Perez-Mendez, and J. Sperinde, Nucl. Instr. Methods 89, 257 (1970).

51. R. Grove, V. Perez-Mendez, J. Sperinde, and G. Stoker, LBL-1035, UC-37 Instruments, TID-4500 (59th Ed.).

52. M. R. Hawkesworth, J. Phys. E: J. Sci. Instr. 2, 235 (1969).

53. J. M. Breare, J. A. Lightfoot, and R. J. Stubbs, Nucl. Instr. Methods 100, 281 (1972).

54. G. Steers, private communication.

55. R. Grove, I. Ko, B. Leskovar, and V. Perez-Mendez, Nucl. Instr. Methods 99, 381 (1972).

56. J. P. Blewett and J. H. Rubel, Proceedings of the Institute of Radio Engineers 35, 1580 (1947).

57. I. A. D. Lewis, Institute of Electrical Engineers (Sec. III), 312 (1951).

58. F. D. Lewis and R. M. Frazier, Proc. I. R. E. 45, 196 (1957).

59. H. E. Kallman, Proc. I. R. E. 34, 646 (1946).

60. R. Halmshaw, Ed., Physics of Industrial Radiography (London: Heywood, 1966).

61. R. H. Morgan, Am. J. Roentg. 62, 870 (1949).

62. H. A. Klasens, Philips Res. Rep. 1, 241 (1946).

63. M. R. Hawkesworth and M. A. Raoof, J. Phys. E3, 851 (1970).

64. H. L. Atkins, Materials Evaluation 23, 453 (1965).

65. R. Buchet, Journal de Radioligie, d'Electrongie et de Medicien Nucleaire 51, 269 (1970). Reprinted in English translation in "Neutron Sources and Applications", Proceedings of the ANS National Topical Meeting, April 19-21, 1971, Augusta, Georgia, CONF-710402 II, II-37 (1971) and M. Brown, ibid. I, II-19.

66. W. L. Whittemore and P. J. Boyne, Research/Development, July 1971, p. 22; P. J. Boyne and W. L. Whittemore, Oral Surgery, Oral Medicine, Oral Pathology 31, 152 (1971).

67. P. Steward, UCRL-18127, Ph.D. Thesis (1968).

68. R. D. Lowde, Rev. Sci. Instr. 21, 835 (1950).

69. J. F. Fanni, Tech. Rept. #AFWL-TR-65-150 (September, 1966).

70. S. Block and K. F. Petrock, Hazards Control Quarterly Report No. 18, Lawrence Radiation Laboratory Report UCRL-12167 (July-September, 1964), p. 19.

71. R. Bouclier, G. Charpak, Z. Dimcovski, G. Fischer, and F. Sauli, Nucl. Instr. Methods 88, 149 (1970).

72. K. Rossman, Phys. Med. Biol. 9, 551 (1964).

73. H. S. DeBen, The Journal of Photographic Science, 1964, Vol. 12, p. 148.

74. J. P. Barton, Applied Materials Research (April, 1965), p. 90.

75. H. J. Moe, S. R. Lasuk, and M. C. Schumacher, ANL-7291 (September, 1966), p. 89.

76. C. B. Lim, D. Chu, L. Kaufman, V. Perez-Mendez, and J. Sperinde, Lawrence Berkeley Laboratory Report LBL-2041; IEEE Transactions on Nuclear Science, Volume NS-21, Number 1 (February, 1974), p. 85.

77. D. Corson and P. Lorrain, Introduction to Electromagnetic Fields and Waves (W. H. Freeman and Co., San Francisco, 1962), p. 136.

78. CRC Standard Mathematical Tables, 17th Ed. (The Chemical Rubber Co., 1969), p. 469.

79. Ibid., p. 500

TECHNICAL INFORMATION DIVISION
LAWRENCE BERKELEY LABORATORY
UNIVERSITY OF CALIFORNIA
BERKELEY, CALIFORNIA 94720